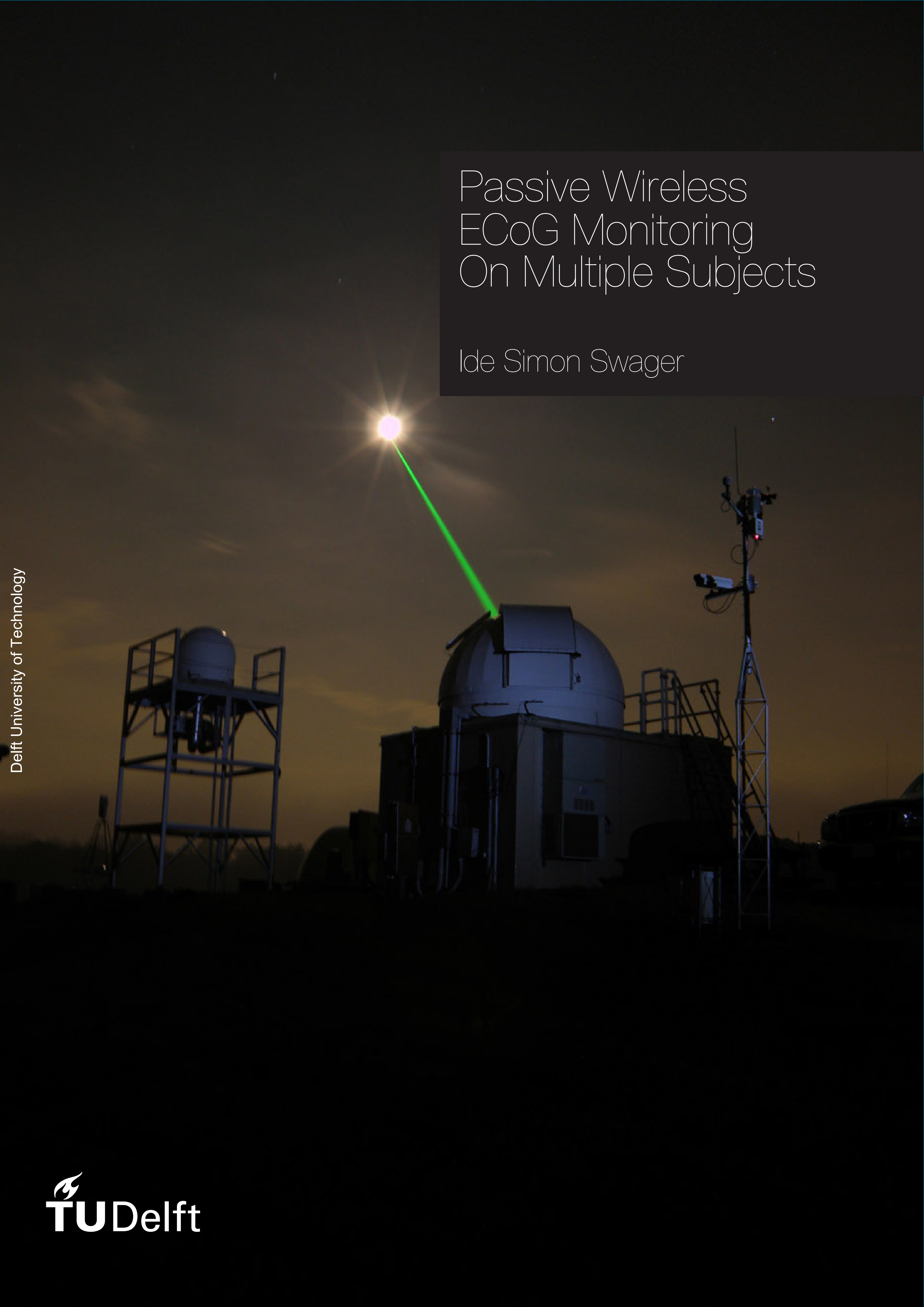

Passive Wireless ECoG Monitoring On Multiple Subjects

Ide Simon Swager

Delft University of Technology

Passive Wireless ECoG Monitoring On Multiple Subjects

by

Ide Simon Swager

to obtain the degree of Master of Science
at the Delft University of Technology,
to be defended publicly on Friday September 16, 2016 at 10:00 AM

Student number:	4042026	
Project duration:	September 1, 2015 – September 16, 2016	
Thesis committee:	Prof. dr. ir. W.A. Serdijn,	TU Delft, supervisor
	Dr. ir. G. Janssen,	TU Delft
	Dr. P. Pawelczak,	TU Delft
	Dr. F. Hoebeek,	Erasmus MC

Frontpage picture taken by Tom Zagwodzki, Goddard Space Flight Center. It shows the Lunar Laser Ranging experiment, which involves measuring a reflected laser beam off a mirror on the moon.

An electronic version of this thesis is available at `http://repository.tudelft.nl/`.

TU Delft

Abstract

In this work, a system level design for a wireless, multi-subject ElectroCorticoGram (ECoG) monitoring system for epilepsy research on mice is presented. It is a continuation of previous collaborations between the Erasmus Medical Centre (EMC) neuroscience department and the section Bioelectronics at Delft University of Technology. The system is realized by using discrete components and custom PCB development. The innovative focus has been put on the design of a flexible wireless link that uses backscattering, Frequency Division Multiple Access (FDMA) and an Software Defined Radio (SDR). The combination of a high bitrate (up to 320 kbit/s) backscattering link that uses digitally generated subcarriers and FDMA to support multiple concurrent measurements has not been presented in literature before.

Weight, size and power consumption have been identified as the most stringent limitations. The 915 MHz ISM band is used for communication, for which the potential GSM interference should be taken into account. The design of the system contains the RHD2132 IC by Intantech to function as Analog Front-End (AFE), a Cortex M0+ low-power microcontroller (MCU) and an RF switch and chip-scale antenna for backscattering communication. The MCU communicates with the AFE and generates the data packets and the subcarrier frequency. This subcarrier is modulated on the main 915 MHz carrier by means of on-off-keying. A prototype receiver has been designed to be able to evaluate the wireless link.

Up to three wireless tags were tested simultaneously with different subcarrier frequencies. Provided that the power levels of these subcarriers do not differ more than 6 dB, the receiver can distinguish between the different tags and thus FDMA on a backscatter link has been demonstrated. Furthermore, it was proven that using multiple, orthogonally oriented antennas on a tag can increase the backscattered power by an order of magnitude while providing more immunity to the location and orientation of the tag. Power consumption has been measured for 2 scenarios. For a 500 Hz sampling rate scenario, the complete system consumes 14.5 mW. For a 20 kHz sampling rate scenario, the power consumption amounts to 20.3 mW. In-vivo measurements of the AFE have been performed, showing a potential improvement over the current measurement set-up at the EMC. This improvement is mostly found in the reduction of 50 Hz interference and the compactness of the set-up. Additionally it was found that a signal resolution of 8 bit can be enough for epileptic seizure detection, which means the requirement on the wireless link can be reduced.

Preface

A little over a year ago, I was introduced to the Erasmus MC neuroscience department. Soon it became clear that neuroscientists experience engineering challenges everyday, and have a great number of ideas to make new devices that can measure a certain aspect of the brain. I could continue a long-lasting partnership between the Section Bioelectronics at Delft University of Technology and the Erasmus MC neuroscience department. Within the context of previous work in closed-loop epilepsy stimulation of Dr. Marijn van Dongen and Dr. Lieke Kros and the big dream of having a portable wireless ECoG recording device I was allowed to define my own project. This freedom has been great, but in the first weeks of the project, it took quite some time to find a good direction for my thesis work. At first, my ambition was to make a custom IC that could fulfill part of the wireless functionality in an innovative way. However, I came to realize that an IC is a means to an end, and not the goal itself. By building a system with parts that are already developed, more functionality can be made and the innovation can be done on a system level. It occurred to me that by using commercially available components, time and effort can be saved. The research became more application-oriented, which I think made it an enjoyable project for me.

Next to this, I had a great year because of the good company I had both in Delft and Rotterdam. First of all, I would like to thank Professor Wouter Serdijn for the guidance throughout the project, on a scientific as well as a personal level. I think your approach to education is extremely valuable and can make great engineers. Dr. Freek Hoebeek and his colleagues have always given me a warm welcome with a delicious espresso. From them I learned a bit more about this mysterious organ in the human body that defines our entire existence. Dr. Przemysław Pawełczak showed me important work from the Embedded Systems field, that was relevant to my work. Dr. Gerard Jansen managed to bring me back to the telecommunication basics when it was most necessary.

Furthermore, the cooperation with colleague MSc students Farnaz Nassirinia and Matthijs Weskin was very fruitful. Special thanks to Matthijs who taught me how to design a PCB and to Farnaz for the fun hours in the office. The pleasant environment of the Bioelectronics Section provided a relaxed atmosphere, causing me to cycle from The Hague to Delft every day with pleasure. Additional support by staff and students of the 18th and 9th floors in their respective fields of expertise has certainly contributed to increasing the quality of my work. Last but not least, I would like to thank my family and friends for their support during this long project.

Ide Swager
August 26, 2016

Contents

1

Introduction

With the rapid advancement and miniaturization of electronics, many new applications can be explored. The demand of the medical world for smart, implantable, low-power electronics is increasing. On the one hand, to conduct fundamental research on different aspects of the body, on the other hand to cure diseases and handicaps. Within neuroscience, epilepsy is a disease that forms an important research topic. The neuroscience department of the Erasmus Medical Centre (EMC) has been working for years to analyze epilepsy and come up with alternative treatments. With the development of neural stimulation a new treatment has emerged. Both electrical and optogenetic stimulation are being explored as potential new treatments. However, in order to decide when and where to apply stimulation, neural readout electronics are required as well. This means that the system should be able to interpret the brain activity and detect an epileptic seizure, after which electrical or optogenetic stimulation can be used to suppress it. This is a so-called closed-loop approach: neither patient nor doctor needs to interact with the system. The research is mostly fundamental, which means it can not be conducted on humans yet. Instead, mice are most often used in neuroscience research, for their practical convenience and similarity to humans in terms of brain anatomy. In order to have a reliable test environment, a miniature device is needed that measures the brain signal and can stimulate on demand, while allowing the mouse to move around freely.

Current solutions for monitoring neural signals mostly consist of bulky set-ups with sales prices exceeding 10.000 euros [1]. Some smaller parties like Neurologger have developed a portable neural recording device for mice, however it works with SD-card storage, is not realtime and uses a battery [2]. Dedicated ICs have been developed that can record neural signals and send them using a passive communication link [3]. This implementation only works for one subject at a time. A discrete realization for rats has been developed in [4], but this solution has high power consumption and can not support multiple animals simultaneously.

Together with MSc students Farnaz Nassirinia and Matthijs Weskin, our goal was to make a device that can be carried by a mouse and that can be used with multiple animals simultaneously. Farnaz Nassirinia focused on the wireless power transfer and driving electronics for the optogenetic stimulation LEDs. The Analog Front-End (AFE) was developed in close cooperation with Matthijs Weskin, who focused his MSc Thesis on the development of a recording system for olivary recordings in mice. The focus of my work was placed on the uplink wireless communication. The most important design requirement is that the ElectroCorticoGram (ECoG) of multiple mice can be examined simultaneously while they are able to move around freely. This allows for analysis of social interaction between mice on a neuroscience level. In the current laboratory environment at the EMC, mice are mounted with their head, limiting their interaction with the environment or other mice.

Table 1.1 compares the commercial and scientific systems that have been developed for the same application. The comparison is made based on the design requirements discussed in Chapter 4. Please note that the goal stated in Table 1.1 is the goal of the combined project with Farnaz Nassirinia and Matthijs Weskin.

Table 1.1: Comparison of current work compared to the end goal of the combined effort of this work and the work of Weskin and Nassirinia.

	Thomas [3]	Newbehavior AG [2]	CED Ltd. [1]	Gagnon [4]	**This work**
Wireless	✓	✓	-	✓	✓
Realtime	✓	-	✓	✓	✓
Multi-animal	-	✓	-	-	✓
No. of channels	10	4	8	32	3
Power supply	Wireless	Battery	Wire	Battery	Wireless
Stimulation	-	-	✓	✓	✓
Portable	✓	✓	-	✓	✓

At the start of the project, it was not clear whether an implementation on chip or a discrete implementation would be the best choice for this work with respect to the design requirements and time available. During the literature research phase it became clear that many publications in BioCAS related to neuroscience are focusing on system level designs. The reason for this is that the medical scientists using new technologies need fully functioning devices. A small part of a system that shows a marginal improvement over its predecessors in literature is not practically usable in a medical setting. Additionally, commercial discrete components are readily available for medical applications. Therefore, it was decided to focus on developing a minimum size discrete implementation of a low-power wireless uplink that would allow ECoG readout of multiple mice simultaneously. To realize this system, the backscattering technique in combination with Frequency Division Multiple Access (FDMA) was used to achieve an order of magnitude reduction in power consumption and eliminate the need for intense processing and downlink communication. Passive wireless communication, or backscattering, is used ubiquitously in Radio Frequency Identification (RFID) technology. The communication is performed by changing the reflective properties of the antenna, consuming very little power. To the best knowledge of the author, the combination of backscattering, FDMA and bitrates required for ECoG has never been implemented before.

To come to a well-funded decision about what part to focus on, an overview was made in Chapter 5 between commercial Integrated Circuits (ICs) that could be used to fulfill the functionality of toplevel design. These ICs were mostly compared in terms of size, power and compatibility with the other systems described in Chapter 5. For the AFE as well as the wireless communication uplink, many ICs exist. However, when looking at the power consumption, size and functionality, it becomes clear that there are more interesting opportunities in creating a low-power wireless uplink that can work well with multiple animals. Specifically, no commercial solution for passive wireless communication exists. By choosing a passive communication implementation - making the wireless data transmission highly asymmetrical - the power consumption of the total system on the mouse can be significantly reduced.

A compact overview of the medical background is given in Chapter 2. The current state of the art in system design and passive wireless communication is described in Chapter 3. To clarify the different project boundaries a toplevel schematic was developed. Its requirements are described in Chapter 4, whereas the toplevel design itself is discussed in detail in Chapter 5. The system is further developed on component level in Chapter 6. After developing the necessary PCBs, the system and its components were tested electrically in Chapter 7, while the AFE was tested in-vivo in Chapter 8. In the final chapters conclusions on the performance are drawn and recommendations for future research are suggested.

2

Medical Background

In this chapter, the medical aspects of epilepsy and properties of the relevant biosignals are described. The first section contains information about epilepsy, its causes, treatments and current challenges. In Section 2.2, different biosignals are briefly explained.

2.1. Epilepsy

Epilepsy is a broad syndrome and has been described since the ancient Greek and Egyptian civilizations. Patients suffering from epilepsy have been limited in their activities and have been experiencing social stigma, isolation and discrimination. In 1954, Penfield and Jasper first conceptualized that epilepsy might be caused by structures in the brain that are electrically unstable [5]. Approximately 65 million people suffer from epilepsy world-wide [6].

Multiple organizations, like the International League Against Epilepsy (ILAE) and the International Bureau for Epilepsy (IBE) have been working for decades on exact definitions and classifications of epilepsy [7]. This is because terms like *epilepsy* and *seizure* are being used extensively in the medical world by people with different professions and backgrounds. Epilepsy can have many causes, ranging from genetic background, to traumatic experiences and unhealthy life-style. Seizures can originate in different regions in the brain. Symptoms can range from generalized absence to muscle contractions and body-wide spasms. Patients do not remember the seizures in most cases. Heavy brain damage can be sustained during seizures. This limits the patients in their freedom, because seizures can be life threatening in many situations (e.g. while driving a car).

Treatment has evolved over the years and currently exists in two directions. By neurosurgical resection on certain parts of the brain or removing the connection between the two brain halves, the symptoms can be reduced to a minimum. Most patients currently take anti-convulsant drugs to suppress the seizures. For about 60% to 70% of the patients these methods work. However, a significant part of the epileptic patients cannot be completely helped by current treatment methods [8]. Next to that, invasive brain surgery is a high risk operation that can involve loss of brain functionality. For this reason, research has been exploring the use of stimulation to cure epilepsy. This research is often conducted on animals in an early phase. At the Erasmus Medical Centre (EMC) Neuroscience department, predominantly mice are used. To be able to better understand epilepsy and decide when and where to apply neural stimulation, it is desired to measure different biopotentials. These are described in the next section.

2.2. Biopotentials

To clarify the physiological background of epilepsy and the resulting requirements on the electronics, this section explains the basics of biopotentials and more specifically the Electrocorticogram or ECoG. The ECoG or intracranial Electroencephalogram (iEEG) entails measurement of the electrical signal of the brain under the skull, at or below the *Dura Mater* [9]. This is one of three protective layers around the brain, below the skull bone. This should not be confused with ECG (Electrocardiogram, the electrical signal of the heart measured on the chest) or EEG (Electroencephalogram, the electrical signal of the brain measured outside the skull).

The human body makes extensive use of electrical and chemical signaling as a means of communication throughout the body [10]. These signals can be measured in many locations. An Electromyogram is another example of such a signal; this involves measuring the electrical signal that causes contraction of muscle tissue.

Depending on the location of measurement, the surrounding tissue (which may be of an isolating nature) and function of the tissue, these biological signals have different characteristics. As this project only involves measuring the brain signal beneath the skull, the ECoG will be treated more extensively in the following subsection.

2.2.1. Electrocorticogram

Measuring an ECoG requires invasive surgery. An example ECoG of a mouse suffering from seizures is displayed in Figure 2.1. The effect of epilepsy on the brain can be seen in this figure, occurring in between the red lines at 84 - 86 seconds and 94 - 100 seconds. During a seizure, so-called Generalized Spike and Wave Discharges (GSWDs) occur, with a frequency below 10 Hz. GSWDs are caused by hyper-synchronized cortical action potentials that fire in a burst-pause rhythm. The amplitude of these GSWD's is generally much higher than the baseline ECoG. The characteristics of seizures and the GSWDs differ between epilepsy types, but these differences will not be discussed in this work.

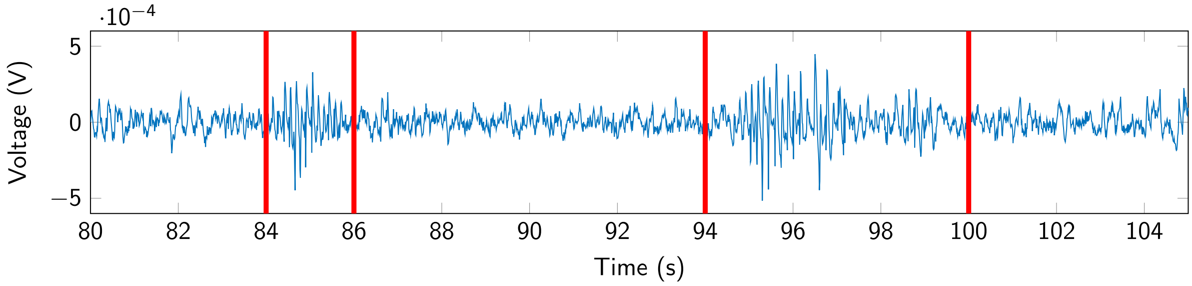

Figure 2.1: Example ECoG recorded from a mouse, filtered and amplified by the Analog Front-End (AFE) created in this work.

One of the biggest advantages of measuring an ECoG compared to an EEG is the improved spatial and temporal resolution of the signal [11]. Bony tissue functions as an electrical insulator, so when measuring outside of the skull, amplitude and bandwidth are reduced. Most often an electrode array with a common reference electrode is used to measure across multiple locations on the neural cortex. Further advantages of ECoG compared to EEG include a better Signal-to-Noise Ratio (SNR) and reduced vulnerability for artifacts [11].

A distinction can be made based on the frequency content. At the lower frequencies - lower than 300 Hz - the so-called Local Field Potential (LFP) is present. This is caused by synaptic membrane currents and other sources, that are lowpass filtered by the neural tissue. At the higher frequencies - from 300 Hz to 10 kHz - multi-unit activity caused by action potentials can be identified [9]. The most important impact on the measurement system would be the sampling rate needed for the two types. When measuring action potentials, the sampling rate should be at least 20 kHz, increasing the bitrate with a factor of 40 compared to measuring LFP's.

The ECoG potentials were measured with the existing electrode set-up of the EMC Neuroscience department, consisting of ball-tipped silver wires making contact with the dura mater. Three ECoG channels are positioned at cortical regions of the brain that are important for epileptic seizures (primary motor and sensor cortex). One reference electrode is placed on the posterior side of the brain. Recordings with a glass electrode were conducted as well, to assess if the AFE could handle this type of electrode.

3

State of the Art

A large range of brain disorders that are difficult, impractical or expensive to treat by medicine, like Epilepsy, Parkinson's disease, depression, Tourette syndrome and many others could eventually be treated by stimulation [12]. The term *electroceuticals* has been coined for such electronic treatments. Next to these disorders that could be treated with stimulation, patients suffering from paralysis of any form, like ALS patients, MS patients, or paraplegics, could be helped with systems that read their brain activity and control (artificial) limbs. To achieve this, brain-machine interfaces are needed. Brain-machine interfaces are neural recording devices, that are preferably portable and fully implantable [13]. The most important reason to make them fully implantable is hygienic: a permanent connection through the skin (percutaneous connection) can cause irritation and infection [14]. This implies that either 1) a battery is implanted with the device, 2) the device harvests its energy from the surroundings, or 3) the device is powered wirelessly. The first solution is used in pacemakers, whereas the third solution is used in cochlear implants. Energy harvesting can be done in many domains: thermal, mechanical, solar, chemical, and electrical to name a few. An example of a chemical glucose energy harvester to be used in the human body can be found in [15]. This produces 3.4 μWcm^{-2} of steady-state power. In comparison, wireless power links can achieve mW's of transferred power.

The field of wirelessly-powered biomedical implants has been growing extensively in the last decade [16]. This can be clearly seen in the number of publications in this field in the last few years as depicted in Figure 3.1. Because this area of research is relatively new, there is still enough room for improvement, but there is sufficient state-of-the-art work to learn from as well.

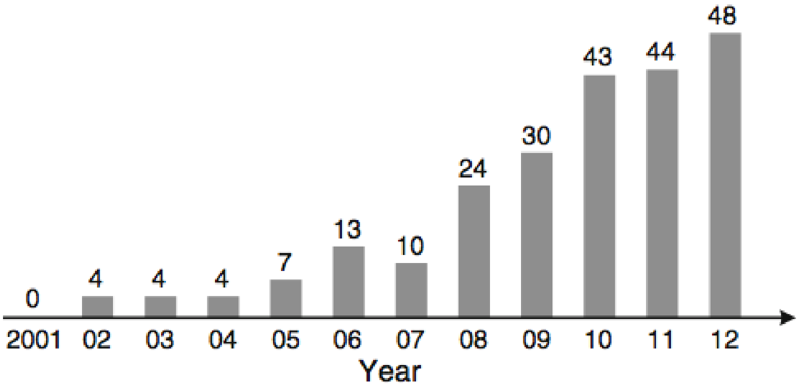

Figure 3.1: Number of publications found on IEEE XPlore concerning WPT applied to implants [16].

This chapter summarizes the relevant literature that has been analyzed for this work. A much broader field of literature was examined in the course of this work, but this is not relevant for the final design so it is not explicitly included in the thesis. A subdivision has been made in the following sections based on the designflow of this work: System level designs (3.1), Backscattering communication (3.2), Analog Front-End (AFE) (3.3) and Power Management (3.4).

3.1. System level designs

A growing number of publications focusses on the design of an entire system, especially in the Transactions on BioCAS journal. Therefore some of these promising developments in complete system designs relevant to this work are treated here. Many designs use commercial off-the-shelf (COTS) components to some extent to realize a quick prototype. One reason for this, is that projects like this one are often conducted in cooperation with an academic hospital. In the end, they need a practically working solution. This asks for a system level approach to a lot of bioelectronics challenges.

The starting point for this research was the work by dr. ir. Marijn van Dongen in cooperation with dr. Lieke Kros of the Erasmus MC Neuroscience department [17]. The system used in this research is described in detail in [18]. Figure 3.2 displays an overview of the system and the implementation of the analog filter. As can be seen, this set-up is completely realized with COTS components. The main purpose of this set-up was to demonstrate the efficacy of the epilepsy detection filter that was implemented in the Beaglebone board. The EEG recorder depicted in this schedule is the Power1401 recording device by Cambridge Electronic Design. Filtering electronics were implemented on a Printed Circuit Board (PCB). This set-up showed that closed-loop epilepsy stimulation is realizable. However, it is large and it is impossible to power it wirelessly. Neuroscientists would ideally want the mice to move freely, without constrictions and with as less stress as possible. Additionally, social experiments with multiple animals are desired. One of the first priorities of this work is therefore to miniaturize the set-up and make it wireless.

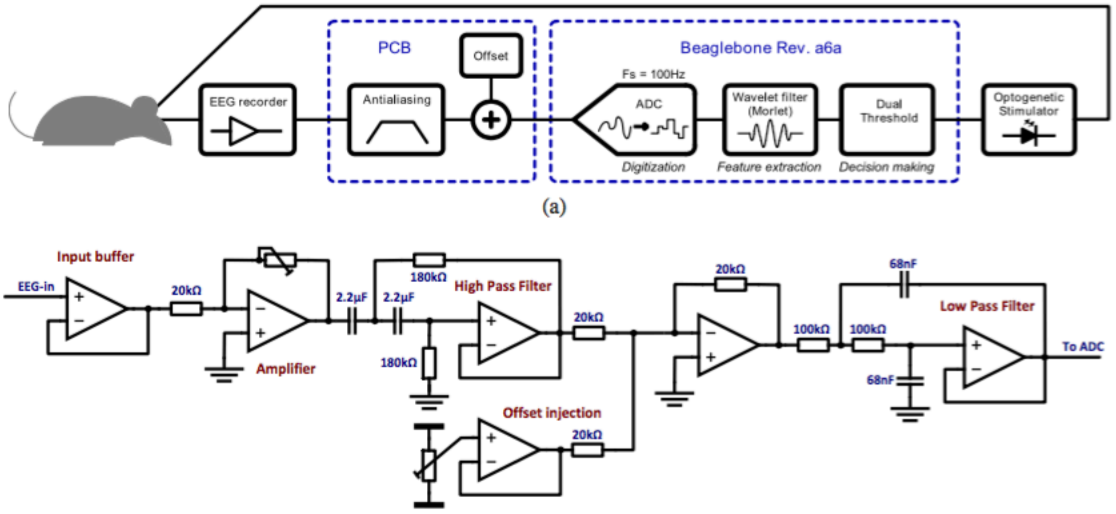

Figure 3.2: Overview of the closed-loop realtime epileptic seizure suppression [18].

An important state of the art work examined for this thesis is a neural interface designed for use on insects [3, 19]. A complete SoC was developed to monitor the neural signals of a dragonfly. This SoC is wirelessly powered via the 902 - 928 MHz ISM band and is capable of measuring 10 neural and 4 EMG signals with an 11 bit resolution. The device weighs 38 mg and measures 6.8 by 4.6 mm. This IC could be a great solution to monitor mice. The architecture of the SoC is depicted in Figure 3.3. However, as can be seen in the design, a big disadvantage of this device is that it is neither programmable nor adaptable. Multiple animal support is not built-in, and can not be easily added either. The range of the system is restricted, and in some combinations of polarization and distance, power to the IC is lost. Complete system on chip integration has major power benefits, but reduces the flexibility. In conversation with the EMC neuroscience department, it became clear that flexibility of the set-up is important in animal research. As experiments change and other devices are replaced, the electronics must be able to adapt to these changes.

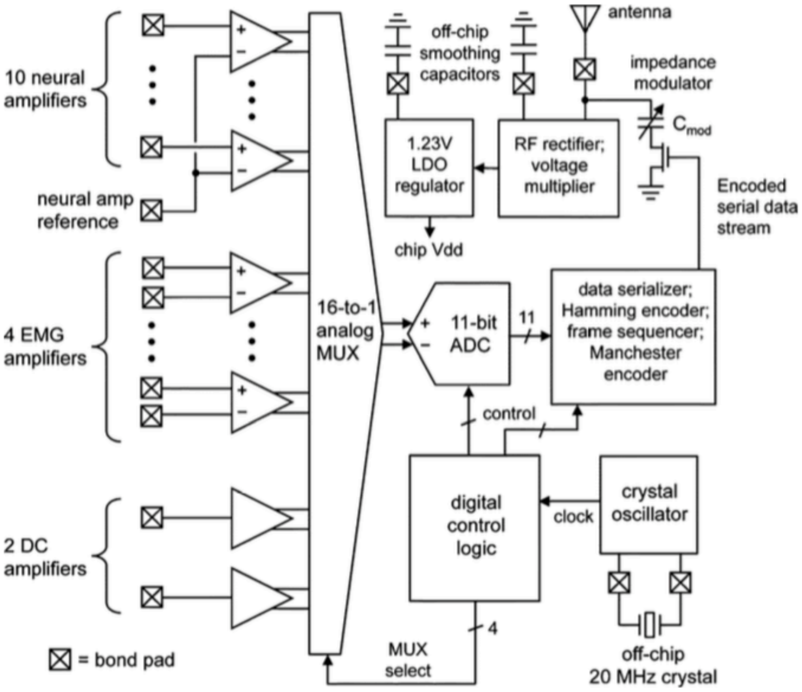

Figure 3.3: System architecture of the dragonfly monitoring SoC [3].

One of the disadvantages of having only one wireless link for power and communication, is that the sharing of this link reduces the performance of both the power and communication links. On the plus side, for one frequency only one antenna is needed. Andre Mansano, Yongjia Li et al. have developed a wireless ECG sensor node that uses two wireless links: one at 13.56 MHz for power supply and the other at 402 MHz for uplink data transfer [20]. Because the 402 MHz link is passive and is not used for power transfer, no compromises have to be made in modulation depth to allow for power harvesting. Figure 3.4 displays the toplevel design of the combined work of Yongjia Li and Andre Mansano.

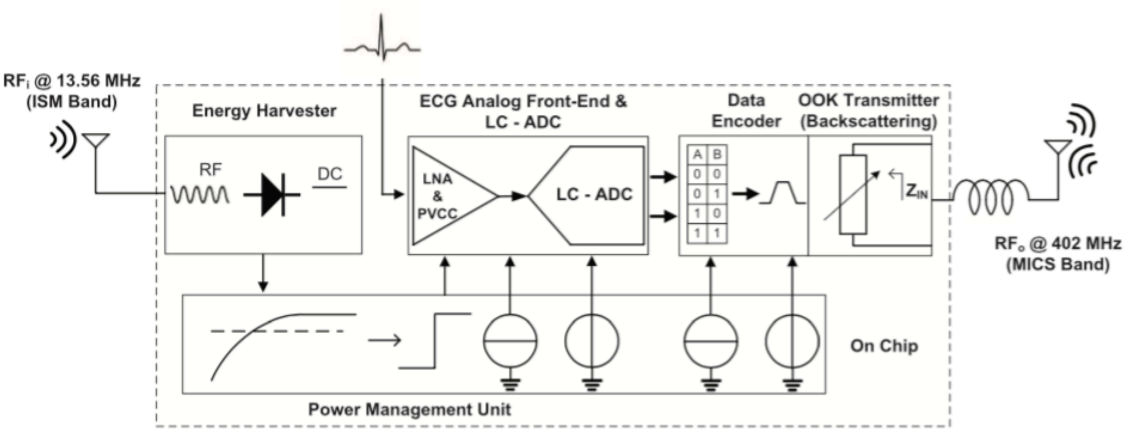

Figure 3.4: Autonomous wireless ECG sensor node toplevel design, employing two wireless links [20].

Another - commercially available - solution that has been used by the EMC neuroscience department is the Neurologger by NewBehavior AG, Switzerland [2]. The company promotes capability for multiple animals, but a battery is used to power the device and flash storage is used to save the data.

Real-time monitoring and closed-loop stimulation is therefore impossible with this system. This product is one of the few implementations that support multiple animal experiments. The devices, mounted on multiple mice, are displayed in Figure 3.5. Not much is known or published about the inner workings of the device, other than that the AD8609 op-amps by Analog Devices are used.

Figure 3.5: Neurologger device on multiple mice [2].

3.2. Backscattering communication

Backscattering - otherwise known as back telemetry or load shift keying - is a means of transferring data via an RF link. The basic principle is that the impedance of the load on the implant side is modified by means of a switching action. This change in impedance can be detected on the receiving side of the link, and can thus be used to transfer data. It is simple and energy-efficient but therefore limited in data rate, distance and encoding options [21]. It is used extensively for commercial RFID (Radio Frequency Identification) tags: plastic cards containing rudimentary electronics can be powered up wirelessly by an external energy source and consequently transmit their identity or other data by means of modulation of the antenna impedance.

This type of communication is considered for use in experimental implants more and more. One of the main reasons for this is its simplicity and low-power requirement for the *tag* or sensor. Backscattering eliminates the need for a dedicated transmitter, which can drastically reduce the total power consumption of an implant [19]. To explain how this is possible, the next paragraphs will discuss the working principles and different strategies used in backscatter systems.

3.2.1. Principle of operation

A backscatter system used for RFID is displayed in Figure 3.6. The reader transmits a carrier signal (either directional or omni-directional), which can be reflected by multiple objects. The tag itself has an antenna that is designed for resonance at the carrier frequency. To achieve this, an impedance matching network is needed. By periodically changing this matching network, the antenna will reflect the electromagnetic waves differently. It is this difference in reflection properties that forms the data transfer from tag to reader. The information is present in the sidebands around the carrier frequency.

At the reader side, demodulation and extensive filtering is needed to recover the information. The most important cause for this is the level of the signal power; as there is no dedicated transmitter at the tag, the signal strength of the tag-to-reader signal is very low compared to the total received power at the reader [22]. A basic illustration of the electronics at the tag side is shown in Figure 3.8. In [22] an extensive derivation is done on how the information of the switching action is superimposed on the carrier frequency. The resulting power in the sidebands can be expressed as in Equation 3.1 [22].

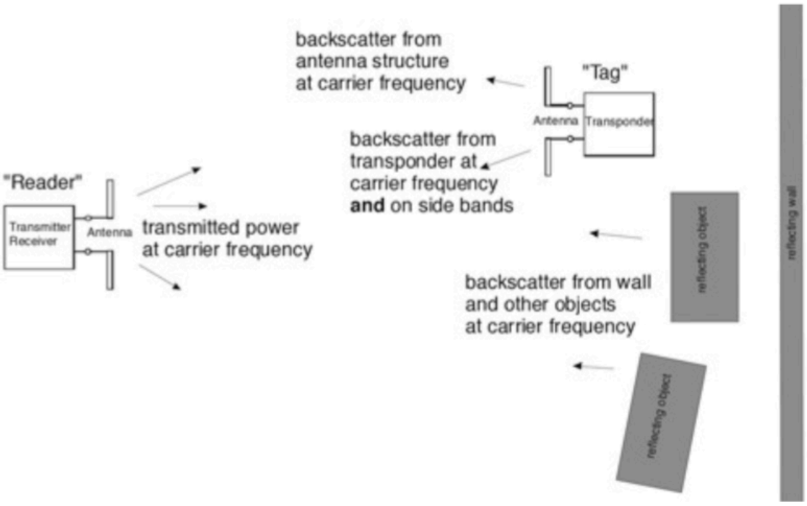

Figure 3.6: RFID system using backscattering [22].

In this expression, only the first spectral lines of the square wave modulation are considered, as the higher (odd) harmonics reduce in amplitude by a factor of $(2n-1)$. For example, the 3rd harmonic amplitude is reduced by $20 \cdot log(3) = 9.5dB$ with regard to the main one. In the equation, r_1 and r_2 are the complex reflection coefficients corresponding to the two states switched at the frequency f_{mod} and $|a|$ is the magnitude of the wave traveling through the antenna. ϕ_Δ is the phase difference between the complex reflection coefficients. The carrier frequency is ω_c.

$$\begin{aligned} s_{bM+}(t) &= \frac{|a|}{\pi}|r_1 - r_2|cos[(\omega_c + \omega_{mod})t + \phi_a + \phi_\Delta] \\ s_{bM-}(t) &= \frac{|a|}{\pi}|r_1 - r_2|cos[(\omega_c - \omega_{mod})t + \phi_a + \phi_\Delta] \end{aligned} \tag{3.1}$$

The total power in the sidebands corresponds to the sum of the power in the individual sidebands, which can be expressed as follows in Equation 3.2 below. As can be seen, the more the reflection coefficients differ in phase and magnitude, the greater the power in the sidebands, and thus the greater the signal power. Theoretically the sideband power can be maximized, but often, the real and/or complex impedance values of antenna's and tags cannot be freely changed to specific values. The maximum achievable modulation depth depends on the type modulation. For PSK, the states can be switched between open-circuit and short-circuit, yielding a phase difference of $180°$. The modulation states are complex conjugates of each other in this case. For On-Off Keying (OOK), the maximum modulation is half of this, switching from a matched load to either open-circuit or short-circuit. In Figure 3.7, the open, short and matched states are indicated on a smith chart. A short circuit is more reliable when switching on high frequencies [23].

$$P_{sb} = \frac{|a|^2}{\pi^2}|r_1 - r_2|^2 \tag{3.2}$$

Another way to consider the signal power is to consider the power dissipated in the antenna impedance. According to [24], the radiated power by an antenna is defined by the power absorbed by the real antenna impedance $R_{antenna}$. This is calculated for the matched and short circuit in Equation 3.3, where U_{ant} is the AC voltage across the antenna [24].

$$P_{rad,matched} = \frac{U_{ant}^2}{8R_{antenna}} \quad , \quad P_{rad,short} = \frac{U_{ant}^2}{2R_{antenna}} \tag{3.3}$$

The average radiated power is then the difference between these two powers (assuming equal number of 1's and 0's in large data sets), which amounts to $P_{avg} = \frac{3U_0^2}{8R_{antenna}}$.

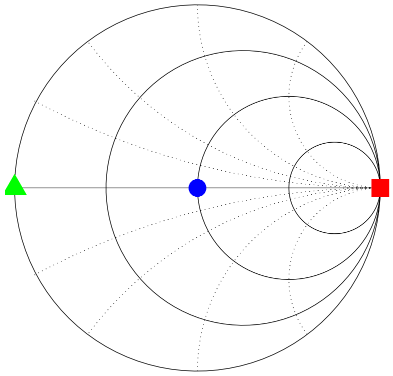

Figure 3.7: Smith chart indicating short (green triangle), matched (blue dot) and open (red square) modulation loads.

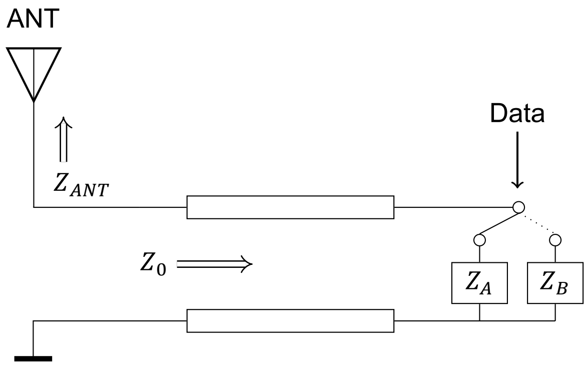

Figure 3.8: Equivalent tag circuit showing the antenna, transmission line with characteristic impedance Z_0 and two modulation loads Z_A and Z_B.

3.2.2. Multiple access

In RFID situations, it often occurs that multiple tags are located within the reach of the reader: interference between the tags is highly likely. To handle interference and enable the reader to communicate with all the tags within its reach, multiple techniques can be used.

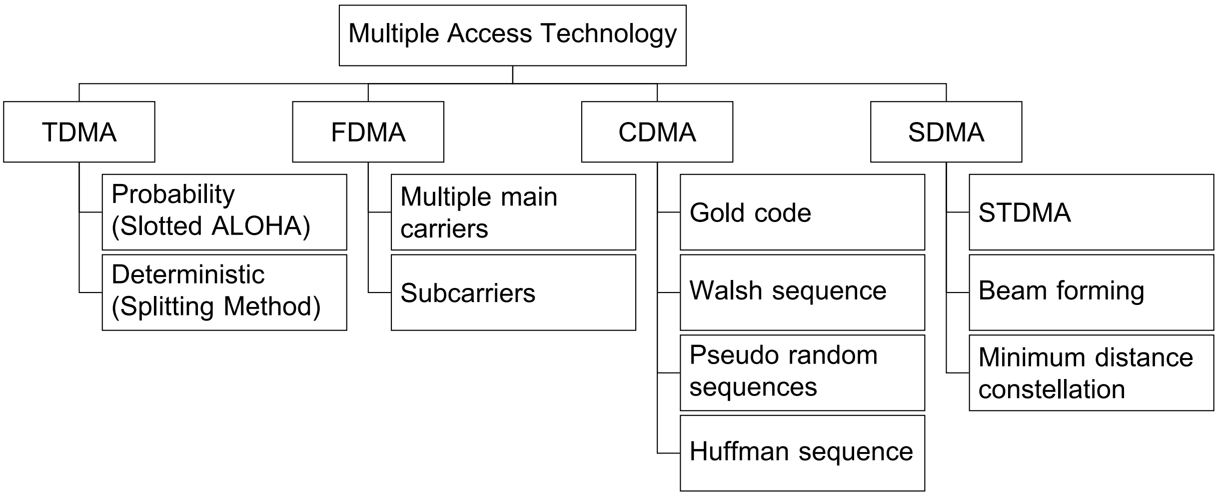

Figure 3.9: Overview of different multiple access technologies and their implementations.

An overview of all different multiple access techniques and their implementations is given in Figure 3.9. Each tag can modulate one of the above aspects in a unique way, so the reader can distinguish multiple tags. Modulation of each one of these fields corresponds to existing techniques: FDMA, CDMA, TDMA, SDMA. Phase and amplitude modulation in the field of backscattering are hard to distinguish, so are not used as multiple access methods.

TDMA
TDMA is often used in RFID and other telecommunication systems [25]. TDMA involves scheduling time slots per tag, which would mean that the tags would need to be synchronized by the reader by means of downlink communication. This would mean added complexity to the tag circuit and could mean that temporary storage of the neural signals is needed. As the most important design goals of the tag are size, weight and power consumption, added complexity should be avoided. Therefore, it was decided not to investigate TDMA any further.

CDMA
In Code Division Multiple Access, or CDMA, data is encoded before transmission with different orthogonal spreading codes. At the transmitter, the different tags can be distinguished by applying these codes again. CDMA does not require time slotting, potentially increasing the throughput of communication systems. The fundamental difference between CDMA and TDMA is illustrated in Figure 3.11. CDMA is used in cellular communications and has been researched for RFID applications as well. The optimum choice between CDMA and TDMA depends on the specific application and the number of tags to read out. As can be seen in Figure 3.12, there is a trade-off between the throughput and the traffic rate of the communication system. TDMA can handle more tags at a lower throughput rate, whereas CDMA is useful when less tags need more throughput. This trade-off is determined by the length of the *spreading codes* of the CDMA system. The spreading codes are the specific codes with which the data is encoded before transmitting. Different coding systems exist, such as Gold codes and Kasami codes. Gold codes are very popular and used in technologies like WLAN and UMTS. In [25], the implementation uses Gold codes for an RFID application. A simplified example of two orthogonal codes is shown in Figure 3.10. One important disadvantage of using CDMA follows from the use of these codes. Processing power is needed for every broadcast, taking processor time and increasing power consumption.

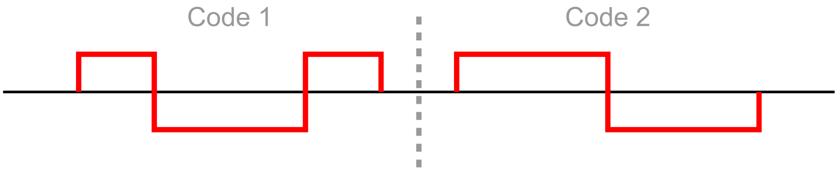

Figure 3.10: CDMA orthogonal codes example.

SDMA
In this relatively new multiple access technology, multiple tags can be read out by making use of spatial information. Often this spatial information is deduced from the angle of arrival of the signal, using an array of reader antennas. It is similar to beam-forming techniques used in audio technology. Reader complexity - both in hardware and software - increases rapidly in SDMA systems. Combination of SDMA with other multiple access technologies, like TDMA, needs further development [26].

FDMA
Frequency Division Multiple Access uses frequency modulation to distinguish multiple tags from each other. Around the main carrier, different frequency bands are used by different tags. This is done by modulating the reflected waves at different frequencies. In this method, it is not needed to create time slots to avoid collisions. The base station of such a system should have good filtering capabilities to filter out each individual tag. FDMA is extensively used in satellite communication. The application of FDMA to (semi-)passive backscattering communication systems to enable multiple access has been explored incidentally in the field of wireless sensor networks [27] [28]. However, these systems were designed for a high number of tags - from 10’s of tags, up to 1000 tags - operating at bitrates of bit/s or several kbit/s. In [27], the FDMA is realized by using different tuning components in each tag. In view

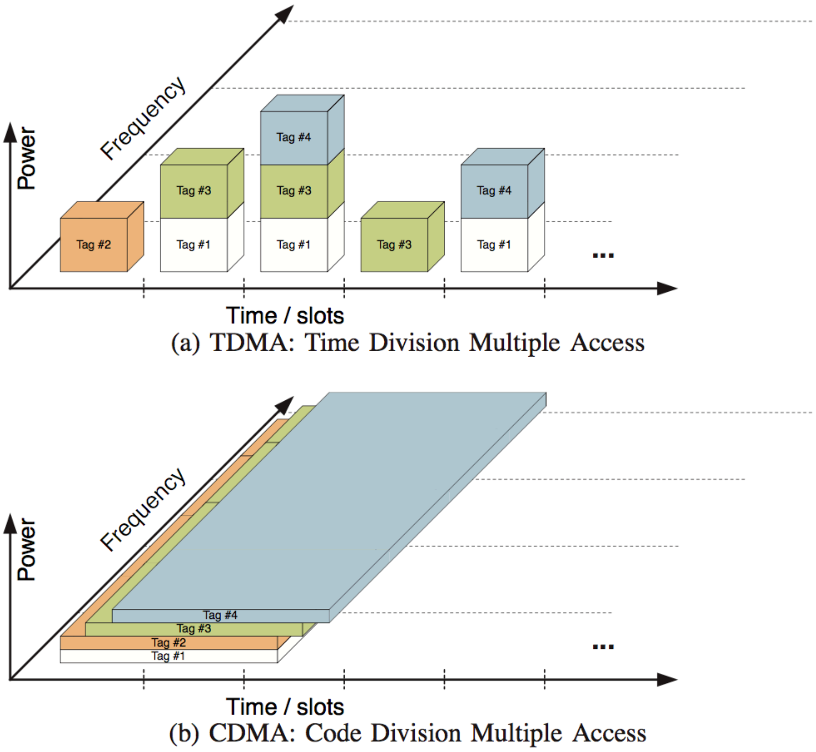

Figure 3.11: TDMA vs. CDMA [25].

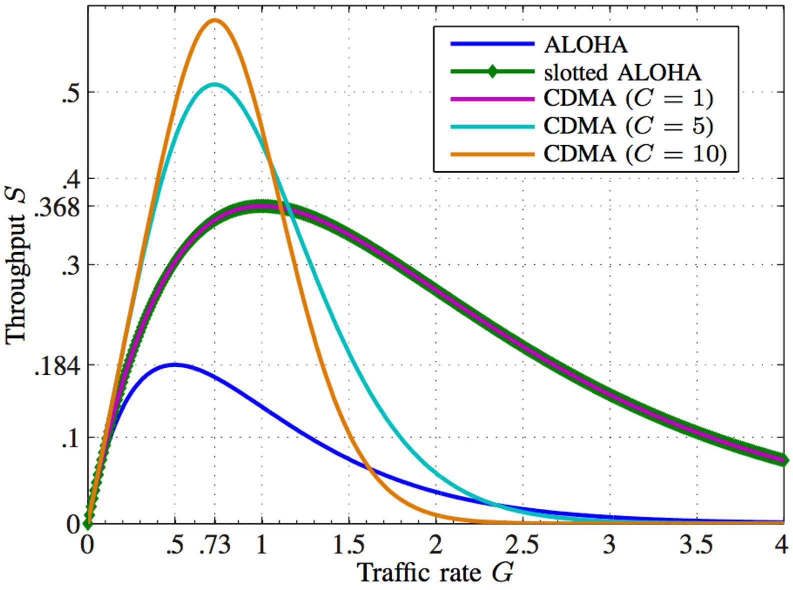

Figure 3.12: TDMA vs. CDMA in terms of throughput and traffic rate [25].

of flexibility and programmability, this is undesired. Economically, it is inconvenient as well, because multiple different tags have to be produced. The design of [28] creates the subcarriers digitally in the tag. In this way, each tag can be programmed to have its subcarrier in a certain frequency. This work focused on the application of wireless sensing with bitrates of 10 bit/s and hundreds of nodes, making the requirements and limitations completely different.

A potential disadvantage of FDMA is the fact that high Q filters might be needed at the receiver side to differentiate between different tags. Additionally, there is limited bandwidth to distribute the different tags in legal terms, putting a hard limit on commercial applications of multiple access using FDMA. On the plus side, heavy processing by the microcontroller (MCU) is not needed, saving power and reducing the requirements on the MCU to be used.

A related technology to FDMA is OFDMA, a digital modulation scheme that harnesses the Fast Fourier Transform (FFT) to spread information across the frequency spectrum. It is used in the LTE standard in cellular communications. OFDMA requires intense digital processing at both sides, because all the data has to be Fourier transformed in realtime. One big advantage compared to FDMA is that high Q filters are not needed. However, due to the stringent power requirements at the tag side, heavy processing is not an option.

3.2.3. Modulation strategies

Many encoding strategies have been developed over the years, starting from simple On-Off Keying (OOK) and Binary Phase Shift Keying (BPSK) to complex 256-QAM (Quadrature Amplitude Modulation) schemes. In the case of backscattering communication systems, OOK and BPSK are often used because of their simplicity. However, there have been successful attempts to use 8-QAM and even 16-QAM in backscattering configurations [29], [30]. The most important advantage of using more complex encoding strategies is the increased data rate that can be achieved. However, the backscatterd signal power remains the same. To keep the Bit Error Ratio (BER) acceptable, the requirements on the receiver are increased.

3.3. Analog front-end (AFE)

In order to acquire ECoG data, a low-noise, high amplification and digitization front-end is needed. ECoG signals are in the order of 10's of μVolts and vary from low frequencies of several Hz to about 10 kHz for single cell action potential recording. To make a completely new and integrated AFE consisting of biopotential-amplifiers, filters, a multiplexer and an Analog-to-Digital Converter (ADC) is beyond the scope of an MSc thesis project.

Many state of the art publications in wireless biopotential recording have used commercially available AFE's. The AFE developed in [3] has been further developed into a commercial product, the Intantech RHD2132. In [4] it is implemented in a wireless optogenetic headstage for rats. In [31] a real-time spike sorting system used the RHD2132 and an FPGA.

3.4. Power Management

One of the challenges of developing implants - especially for small animals like mice - is supplying energy to the electronics. Multiple options are available, like using a battery, connecting a transcutaneous cable, or supplying the energy wirelessly [32]. Using a transcutaneous cable like [33] can be a good solution, but it limits the freedom of the animal and can cause infections as well. A battery powered solution as in [34] can be effective but increases the size and weight of the implant. Wireless power transfer seems to be the best option for flexibility and ease-of-use. Farnaz Nassirinia has worked on the wireless power transfer and downlink communication by means of inductive coupling. To have a better understanding of the wireless power transfer, the reader is referred to the work of Farnaz Nassirinia. This work will not elaborate further on wireless power transfer. To evaluate the system developed in this work, a battery solution has been used.

4

Design Specifications

The main challenges of designing electronics for implants are caused by the strict requirements in terms of power management, size, biocompatibility and safety for the patient. In this project, the main challenges were found in power management and minimum size. This chapter is devoted to a detailed description of the specifications for the design, as well as the reasons for these specifications. As this project was conducted for the Erasmus Medical Centre (EMC) neuroscience department, detailed electrical specifications would have to be deduced from the experience of the neuroscientists. This posed an additional challenge to the early design phase. In the next sections, the design specifications are discussed per category.

4.1. Size

Different species of house mice are used for the experiments, in different stages of development [17]. This results in very small animals that have to be fitted with the implant. A commonly used strain of laboratory mouse is C57BL/6. In the EMC neuroscience department, genetic mutant mice are used. Figure 4.1 displays the weight during growth and development of the mouse.

The mice are experimented on when they are 4 to 33 weeks old [17]. As can be seen in Figure 4.1, the mice weigh around 20 g. An acceptable limit for the weight to carry is 10% of the body weight, according to the EMC neuroscientists. This results in a weight requirement of 2 g maximum. This same requirement is used by [32] as well for similar research on mice.

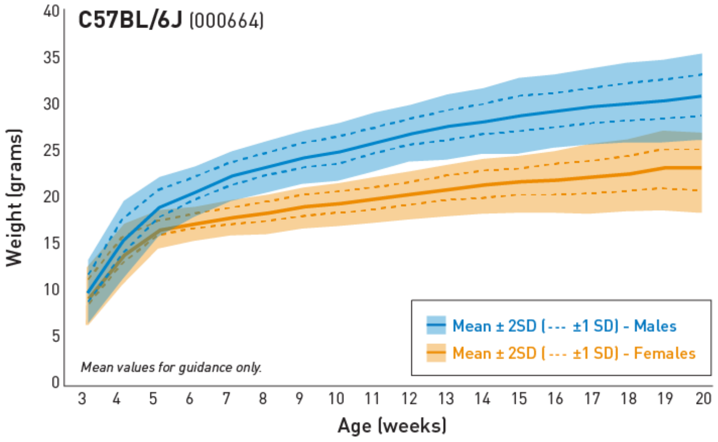

Figure 4.1: Weight of the C57BL/6 mice at different ages [35].

In October 2015, 3 five week old mice have been measured. The length of the head is about 12 mm and the width amounts to 8 mm on average. This data and the expertise of the neuroscientists was used to set a design requirement for the size of the implant including external electronics. In order to provide the mice with enough freedom at young age, the size should not exceed a volume of 1 cm^3 and a surface area of 9x9 mm^2.

4.2. Power

The power requirement is mostly determined by the fact that the amount of power available by wireless transfer or battery is very limited. Next to that, an increase in temperature of the tissue surrounding the implant should be kept to a minimum [21]. This means the design effort should be focused on minimizing power consumption at the side of the mouse.

4.3. Data

Most experiments in the EMC neuroscience department use between 3 to 6 electrodes. As a starting point, a minimum number of 3 electrodes was chosen to be the design criterium.

For biomedical systems, depending on the application, ADC resolutions are as low as 7 bit [36]. Power consumption and limited data rates in wireless devices form a strong incentive to work with low resolutions. To make a requirement for resolution, the needed dynamic range must be considered. If the smallest signal would be in the 10 μV range, and the largest signal in the mV range, the required dynamic range of the ADC would be $20log(10^2) = 40dB$ over the required signal bandwidth. To achieve this, at least a 7 bit resolution is needed, according to Equation 4.1. Other aspects like ADC linearity, accuracy and jitter that can degrade the resolution have not been taken into account in this number. In the author's opinion, a resolution of 10 bit would be minimum for this application, whereas a higher resolution like 12 or 16 bit would be more robust.

$$SNR = 20 * log_{10}(2^n) + 20 * log_{10}(\frac{3}{2}) \approx 6.02 * n + 1.72 \tag{4.1}$$

Finally, the required sampling rate depends on the type of ECoG signal that is to be measured. Single cell action potential recordings need a sampling rate of 20 kHz, while summed local field potentials of groups of cells require a sampling rate of 500 Hz. The resulting bitrate can be calculated with Equation 4.2. For 3 channels at an arbitrary 16 bits resolution and 20 kHz sampling rate this amounts to 0.96 Mbit/s. Lower sampling at 500 Hz reduces the bitrate with a factor of 40 to 24 kbit/s.

$$Bitrate = f_{sampling} \cdot Resolution \cdot N_{channels} \tag{4.2}$$

4.4. Multiple animal support

Animal experiments in the fields of psychology and social interaction can yield valuable information to researchers. By enabling the ECoG measurement on mice in multi-animal experiments, neural data can be combined with social interaction in order to gain more insight. Therefore, the goal of making the wireless front-end work for multiple animals was added. Multi animal ECoG monitoring is still a new topic; many ECoG monitoring publications are by their design unable to support multiple animals. As it concerned a first prototype, the design goal was set to support 2 animals simultaneously, with the potential to expand to 4 animals.

4.5. Flexibility

The device will be used for animal neuroscience experiments. Experiments and methods change continuously, so the hardware should be able to cope with these changes. In one experiment, 3 channels at 500 Hz sampling might be needed, while in another experiment, 2 channels need to be sampling at 20 kHz. Making this adaptable implies that a high degree of flexibility needs to be built into the device.

5

Toplevel design

In the previous chapter, the specifications for the design have been determined. These specifications have set the boundaries for the toplevel design. This chapter describes the steps taken and choices made in the early design process.

In this stage of the design, a decision for either a chip-level or discrete realization had not been made yet. In order to build a prototype quickly, a discrete realization was chosen as a first step. After evaluating the discrete realization, some parts could be developed into a custom IC in a later stage. It was decided to focus on a discrete realization because of the broad nature of the project. Figure 5.1 displays an overview of the combined projects. With respect to the top part of Figure 5.1, electrodes are placed in the mouse brain to collect the ECoG, while optodes are placed in the brain to allow for opto-genetic stimulation. There are separate wireless links for power and data transfer, each with their own control units. The parts encircled by the red dashed line are implemented in this work.

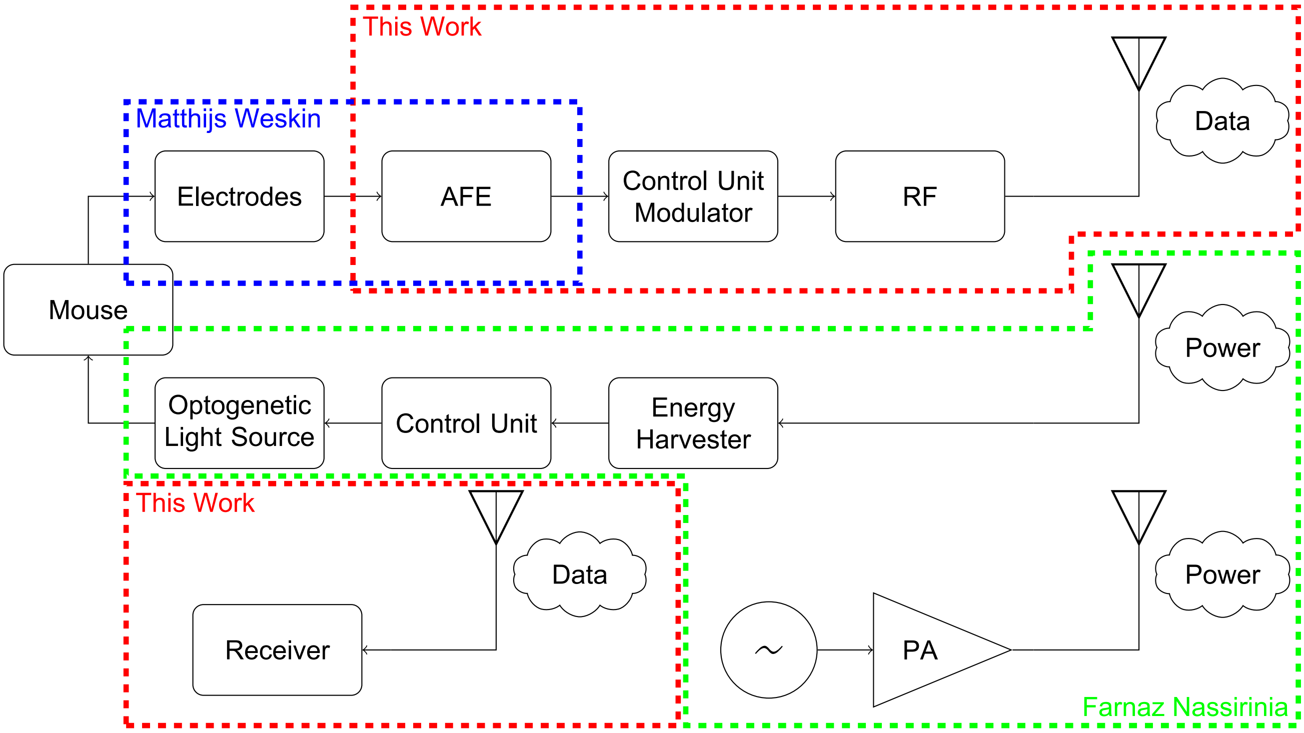

Figure 5.1: Toplevel design using a wireless power transfer and a dedicated transmitter; red areas indicate scope covered by this work. Blue area has been covered by Matthijs Weskin and the green area has been covered by Farnaz Nassirinia.

Three potentially viable toplevel designs were identified and further developed. Next to that, an overview of COTS IC's was made that could fit the requirements of the subsystems.

5.1. Evaluation of COTS components

The COTS components were evaluated in three rough categories: Analog Front-End (AFE), transceivers and control units. The reader is referred to Tables 5.1, 5.2 and 5.3 for the details. In the AFE category, both amplifiers and ADC's are listed.

5.1.1. Analog Front-end

As the field of AFEs for neural recording is relatively new, not many high quality IC's are available on the market. However, the RHD 2132 IC by Intantech is a 32 channel neural amplifier array, multiplexed to a 16-bit SAR ADC with adjustable filtering and offset removal. Other notable IC's in this segment are the ADS1299 and ADS1293 by TI, although the ADS1293 has been developed with ECG as the main application. The ADS1299 has 8 channels. The voltage gain of the amplifiers is 24 at most, which is quite low compared to the voltage gain of 192 of the RHD2132 amplifiers. However, at a power consumption of 40 mW for 8 channels in quiescent mode it can not compete with the RHD2132 at all. The RHD2132 has a power consumption of about 4.4 mW while sampling 32 channels at 2 kHz. The ADUCM360 is based on an MCU with a built-in ADC, but does not have any built-in amplifiers. Mostly because of the high level of integration of all the required components of an AFE, and proven ECoG recording capabilities [4], the choice was made to use the RHD2132 IC as the AFE.

5.1.2. Transceiver

The transceiver IC's are listed in Table 5.2. There is a variety of receivers, with different carrier frequencies and options. The Zarlink and Nordic products are specifically tailored for implants, while the others in the list are more general transceivers. As can be derived from the table, power consumption during transmission is very high. This is one of the most important reasons to focus on the custom wireless backscattering system as a means of communication. Next to this, multiple access technology other than TDMA is hard or impossible to build with most of the transceivers. Additionally, most of the IC's can not handle the targeted 0.96 Mbit/s bitrate. For lower bitrate systems with less stringent power consumption criteria, these IC's might be an excellent choice.

5.1.3. Control unit

The control unit was picked after the decision to use the Intantech RHD2132 IC as the AFE. This meant the control unit had to have at least one Serial Peripheral Interface (SPI) that could handle the bitrate of 0.96 Mbit/s. Other requirements that follow from Chapter 4 include small size and low power consumption. At this point the choice between a Microcontroller Unit (MCU), or a Field Programmable Gate Array (FPGA) had to be made. Table 5.1 shows an overview of the trade-offs between some of the available devices. The low-power Cortex M0+ MCU's belong to the lowest power MCU's available. The FPGA Spartan 6 is used by [4] as part of a neural headstage for a rat. A Complex Programmable Logic Device (CPLD) is a small, low complexity version of an FPGA [37]. Both Xilinx and LatticeSemi have a low-power, small-size CPLD: Coolrunner II and iCE5LP1K respectively.

The Spartan-6 FPGA is very powerful compared to the other devices listed in the table. The design goal for this project is to bring as much of the complexity to the basestation as possible. Using this FPGA would then be overkill in terms of performance and a waste of space and power. The CPLD's have similar specs, while the CoolRunner II is a bit bigger. In terms of speed, the MCU is by far the slowest. The SPI communication is fast enough to handle 0.96 Mbit/s, but for generating the modulation including encoding, it might not be fast enough. The iCE5LP1K looks like the best pick at this point. However, an important aspect for rapid prototyping is ease of use. FPGA's and CPLD's can be challenging to use and adapt, especially if the end-users do not have a background in embedded development. Another small issue for future biomedical designs, is that FDA/CE approval of medical devices containing FPGA's and CPLD's is much harder to acquire. This is based on the fact that FPGA's and CPLD's are essentially devices that can change their hardware, requiring new tests for safety and compliance after every design modification.

Taking all these considerations into account, it was decided to pick the Cortex M0+ as the control unit.

Table 5.1: Trade-offs between MCU, FPGA and CPLD. *has been measured in this work

	Cortex M0+	**Spartan 6**	**iCE5LP1K**	**Coolrunner II**
Manufacturer	NXP	Xilinx	LatticeSemi	Xilinx
Type	MCU	FPGA	CPLD	CPLD
Frequency Max.	48 MHz	1+ GHz	275 MHz	323 MHz
Power static (mW)	2 μW	10+ mW	71 μW	50 μV
Power practical (mW)	10 mW *	30+ mW	mW's	mW's
SPI	✓	✓	✓	✓
Size (mm^2)	2x2	8x8	2.08x2.08	6x6
Programming	C/ASM	VHDL	VHDL	VHDL
RF switching	-	✓	✓	✓
Parallel processing	-	✓	✓	✓

5.2. Final toplevel design: backscattering with FDMA and COTS components

The final conceptual implementation entails the use of backscattering. With respect to Figure 5.2, a battery is used to power the system and the RHD2132 by Intantech is used as the AFE. The RHD2132 is controlled by the Cortex M0+ MCU that prepares the data for transmission as well. Because of the passive nature of the communication link, low power operation is achievable. The modulator is a switching element that will modulate the antenna impedance, thereby providing the means of communication. In Figure 5.2, the switching action is determined by the MCU that takes the data from the front-end, adds additional information like channel number and parity bits, and then prepares the packet in a certain encoding scheme. The schematic of Figure 5.2 will be referenced to throughout this thesis as the *tag*, which is a term from the RFID field that signifies the passive element of the backscattering system.

As can be seen in Table 5.2, conventional wireless transmission IC's would consume at least 10's of mW's of power, making a big impact on power consumption. Table 5.3 shows that some of the AFEs consume power an order of magnitude lower than that. By choosing a backscattering approach to wireless communication, the power requirement of the total system could be strongly reduced. However, backscattered signals are weak compared to traditional transmitters, as there is no active element providing power to the antenna. The information in the sidebands of a backscattered signal could be more than 40 dB below main carrier reflections [22]. This places heavy requirements on the design of the basestation receiver, which is also designed in this work.

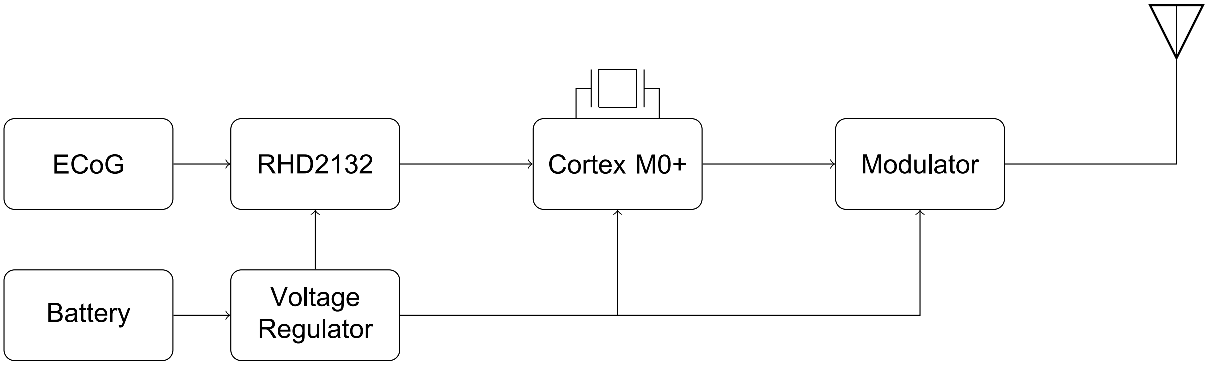

Figure 5.2: Final toplevel design using backscattering communication built with COTS components.

Table 5.2: Overview of commercially available off-the-shelf (COTS) transceiver IC's.

Brand	Name	RX	TX	Power Tx (mW)	Power idle (mW)	Size (mm^2)	Frequency	Notes
Zarlink	ZL70103	✓	✓	-	3.00	4.5x5.5	2.4 GHz	Tailored for implants; MICS
Zarlink	ZL70120	✓	✓	-	-	-	Basestation IC for ZL70103	
ST	BlueNRG	✓	✓	24	16	2.56x2.66	2.4 GHz	BLE IC
ST	Spirit1	✓	✓	63	18	4x4	-	
AD	ADF7020	✓	✓	-	20	7x7	ISM	
LT	LT5503	✓	✓	-	21.6	N/A	WLAN	
Nordic	nRF24L01+	✓	✓	-	40	4x4		Biomedical Low-Power

Table 5.3: Overview of commercially available off-the-shelf (COTS) AFEs.

Brand	Name	Ampl.	ADC	Channels	Power (mW)	Size (mm^2)	Noise	Type	Notes
TI	ADS1293	✓	✓	3	1.2	5x5	-	ECG	Broad front-end for ECG leads
TI	ADS1299	✓	✓	8	40	12.2x11.8	-	EEG	Broad front-end, 5mW/ch
Intantech	RHD2132	✓	✓	32	2-5	8x8	-	EEG	Multiplexed ADC, channels selectable
AD	ADUCM360		✓	x	6	7x7	-	General	Microcontroller with AFE

5.3. Alternative design: battery powered solution with active transmitter

This system is built with COTS components as well. The total system weight will increase because of the battery. The Zarlink ZL70103 transceiver IC is used for communication instead of the backscatter modulation. The ZL70103 communicates via SPI as well, so the control unit should have two SPI interfaces or one SPI interface that is fast enough to communicate with the AFE and transceiver simultaneously. Some important limitations of the ZL70103 are the low maximum achievable bitrate (515 kbit/s), the carrier frequencies it was designed for (402-405 MHz and 433.5-434.4 MHz) and the fact that only TDMA is available in terms of multiple access technologies. This topology could be an option if more power is available and a standard communication format (at low bitrates) is desired.

5.4. Alternative design: custom energy harvesting IC with backscattering modulation

In this implementation, the design focus is on making a custom energy harvesting IC with clock recovery and backscatter modulation. By fabricating these components on chip, the size can be reduced significantly. The AFE and control unit are implemented by COTS parts. Refer to Figure 5.3 for an overview of the schematic. A battery and clock crystal are not needed, but an energy storage capacitor is required to make the energy supply more reliable. When harvesting power from the communication link, a trade-off between link reliability and maximum energy harvesting needs to be made. Many passive communication systems are forward-link limited, which means the power transfer limits the maximum operating distance. The clock recovery and energy harvesting circuits have been designed and used in many biomedical systems: it is hard to be innovative in this field.

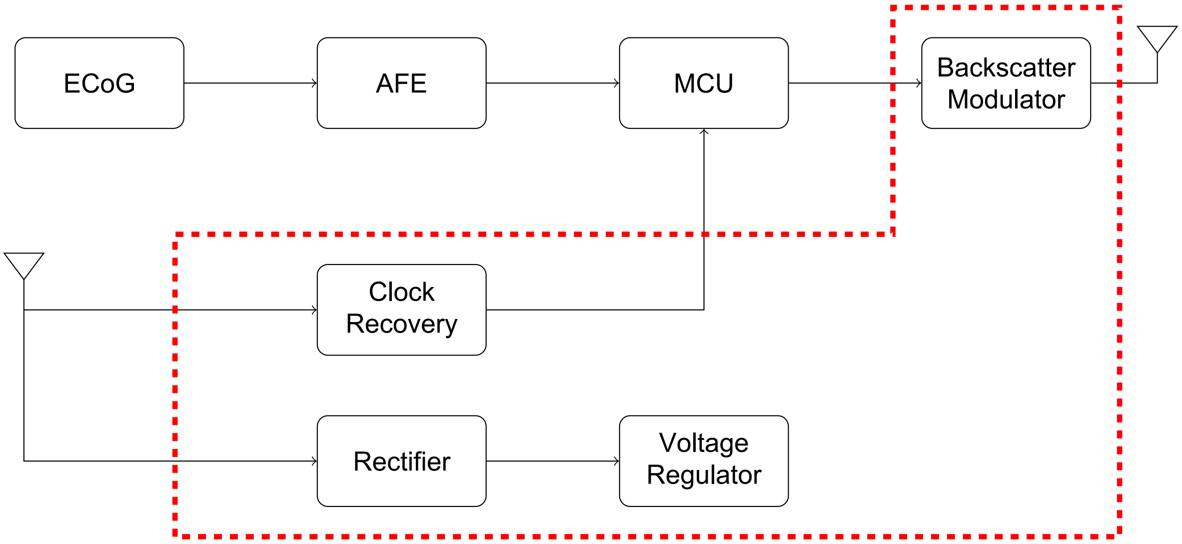

Figure 5.3: Toplevel view of an alternative design using a custom IC with energy harvesting, clock recovery and backscattering modulation; the IC functionality is defined by the red area.

5.5. Conclusions

In this chapter, the relevance of this work within a larger combination of projects has been clarified. Different alternatives for the toplevel design have been discussed based on the specifications stated in Chapter 4. On a component level, COTS ICs have been evaluated. Based on this evaluation, it has been concluded that the toplevel design could be built with COTS components. Furthermore, it has been discussed that the biggest reduction in power consumption of the total system can be achieved by building a custom wireless link using backscattering.

6

Subsystem designs

After the toplevel design choices had been made, the design of the subsystems was initiated. The different components are discussed per section: the wireless link (Section 6.1), the receiver (Section 6.2), AFE (Section 6.3), MCU (Section 6.4) and power management (Section 6.5). As discussed in the introduction, the Analog Front-End (AFE) was developed and tested in cooperation with Matthijs Weskin. Since the specifications regarding the AFE of this work and the work of Matthijs Weskin were similar, a collaboration turned out to be very helpful. Therefore, some of the sections in this chapter have been co-authored. This will be indicated at the beginning of the respective sections.

6.1. Wireless link

To have a structured approach to the design of the backscattering system, the design was split into different aspects. To assess the viability of multiple access applied to backscattering, link budget and modulation simulations were conducted before starting with the practical implementation. The following list summarizes the design aspects that are further investigated in the next subsections.

1. Multiple access method used (CDMA, FDMA, TDMA, etc.)
2. Main carrier frequency
3. Subcarrier planning
4. Modulation method
5. Encoding strategy
6. Antenna system
7. Practical RF considerations

6.1.1. Multiple access method

Following from the design specifications for low tag complexity and low power consumption, FDMA has been selected as the most promising method to use for the multiple animal support. TDMA requires synchronization between tag and receiver (downlink communication). Implementing a downlink will increase the tag complexity, size and power consumption. CDMA involves processing the data before transmission to embed the spreading codes, increasing the requirements on the MCU and increasing power consumption. For a more thorough treatment of multiple access technologies, the reader is referred to Chapter 3.

FDMA can be made with a low load on the MCU. By digitally controlling the individual subcarriers with the MCU, a flexible solution can be developed for multiple animals. Figure 6.1 illustrates the concept of FDMA that will be used in this work. For every mouse, a unique subcarrier frequency is generated (blue waveform). The ECoG data is modulated by On-Off Keying (OOK) on this subcarrier

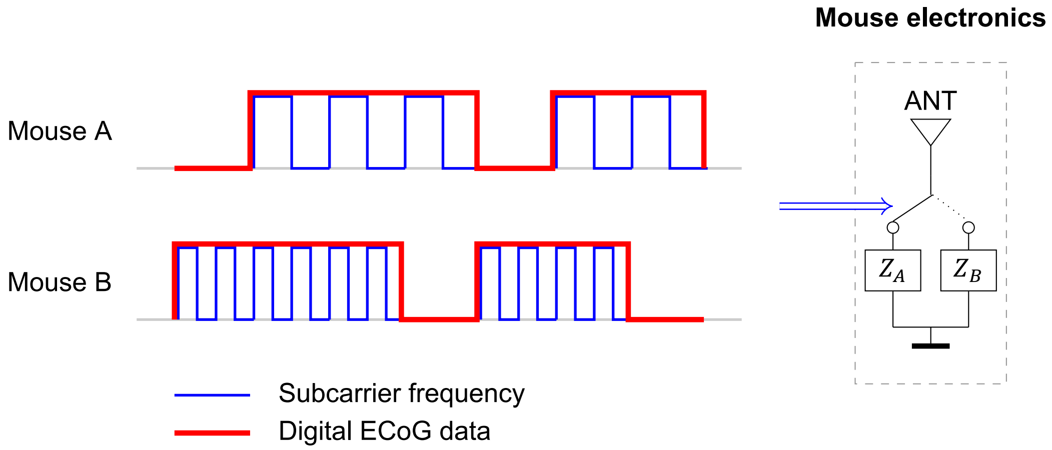

Figure 6.1: Conceptual FDMA implementation at the side of the mouse.

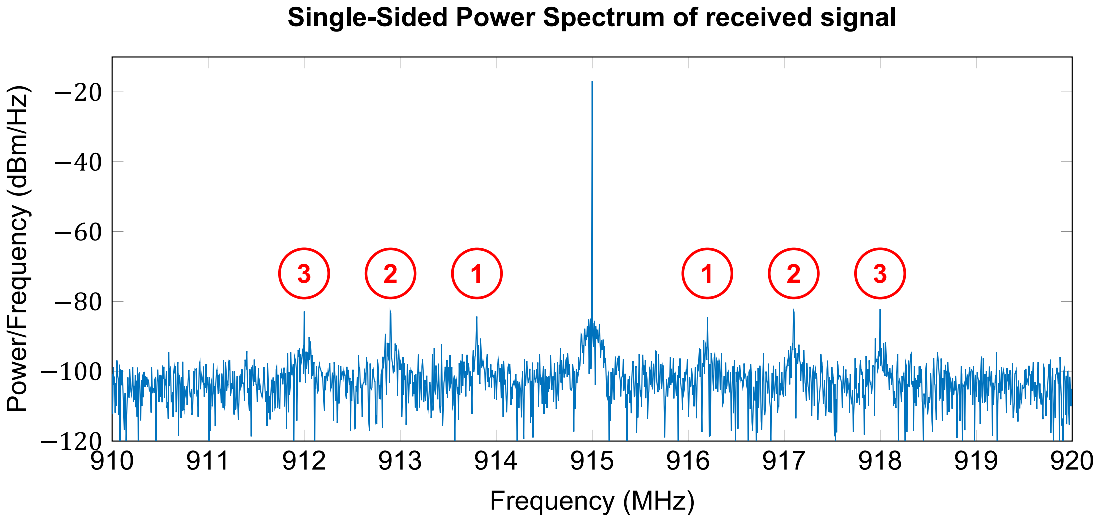

Figure 6.2: Bistatic configuration at 915 MHz, with 3 devices applying FDMA; numbers indicate the subcarrier frequencies at 1.2, 2.1 and 3 MHz respectively.

(red waveform). The blue waveform is used to control the switch that modulates the antenna load. The antenna reflection of the main carrier changes with the speed of the subcarrier frequency. In the receiver, this changing reflection can be filtered out if the subcarrier frequencies are known.

To verify the efficacy of FDMA, simulations were conducted in MATLAB. A sinusoidal main carrier at 915 MHz was generated, and 3 subcarriers were modulated with OOK on the main carrier. The main carrier was simulated to be about 60 dB stronger than the backscattered signals. A total of 30 bits was sent at a bitrate of 24 kbit/s. Additive white gaussian noise was added (SNR = 20 dB) and the link budget models of [38] were used. Figure 6.2 displays the FFT of the received signal. After coherent downcoversion, a 10^{th} order IIR bandpass filter was used to filter out the individual subcarrier frequencies. This resulted in successful recovery of the bits.

6.1.2. Main carrier frequency

The link budget was used for evaluating the choice of main carrier frequency. Extensive link budget simulations and experiments have been conducted on RFID tag systems by [38], using different setups, antenna configurations and environments. Besides different frequencies, monostatic and bistatic basestation configurations were evaluated. The difference between a monostatic and bistatic configuration is the use of 1 or 2 antennas in the basestation. In case 2 basestation antennas are used, the distance between them can influence the link budget. Figure 6.3 illustrates the different configurations, which will be further elaborated on in Subsection 6.1.6. For now, the relevant equations will be used to evaluate different carrier frequencies. Equation 6.1 states the two relations for the received power for a monostatic and bistatic design [38]. With respect to Equation 6.1, P_T is the transmitted power by the reader, G_T, G_R and G_{tag} the gains of the different antennas, λ the wavelength of the carrier, X the polarization mismatch, M the modulation factor, r the distance, θ the on-object gain penalty, B the path blockage and F the fade margin. For the monostatic case, G_{TR} indicates the gain of the single basestation antenna.

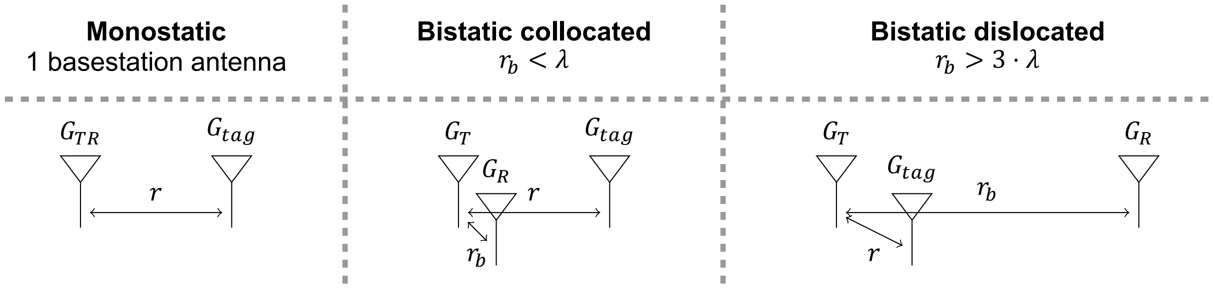

Figure 6.3: Monostatic, bistatic collocated and bistatic dislocated configurations.

$$\begin{aligned} P_{Recv,Monostatic} &= \frac{P_T G_{TR}^2 G_{tag}^2 \lambda^4 X^2 M}{(4\pi r)^4 \theta^2 B^2 F_M} \\ P_{Recv,Bistatic} &= \frac{P_T G_T G_R G_{tag}^2 \lambda^4 X^2 M}{(4\pi r)^4 \theta^2 B^2 F_B} \end{aligned} \tag{6.1}$$

The maximum transmitted power P_T is mainly limited by FCC / EC regulations, just like the usage of different frequency bands, limiting the choice of λ. Fade margin is a factor that takes the effect of multipath fading into account. At a given link outage probability and Rician K factor, the fade margin expresses the amount of additional power that should be transmitted to achieve the given outage probability. The fade margins calculated in [38] were used in this work, as similar conditions are used. The modulation factor can be influenced by the type of backscattering that is employed and the encoding used. Polarization mismatch X is a parameter that cannot be controlled in itself, but it can be improved by certain design choices with respect to antenna configuration and the polarization of the base station signal.

The fact that the wavelength appears in the equation for the link budget, is fundamentally not caused by the intrinsic gain itself, but by the *effective antenna aperture* - the effectiveness with which an antenna can 'collect' electromagnetic radiation in a certain wavelength. It depends on the gain of the antenna G and λ, as stated in Equation 6.2.

$$A_{eff} = \frac{G\lambda^2}{4\pi} \tag{6.2}$$

One of the most used bands in medical wearable and implantable electronics are the MICS Bands (Medical Implantable Communications Service Band) and ISM Bands (Industrial Scientific and Medical Band). Table 6.1 lists the different bands and frequencies with their most important properties and other services present on this band [39–42]. Different licensing methods apply. WMTS and MICS (MedRadio) are both licensed by rule, which means individual licenses are not required. Others are unlicensed, which means that potential interference from other devices must be accepted. A relatively new band that was created by the FCC in 2012 is the Medical Body Area Network band (MBAN), which consists of the 2.36 GHz - 2.4 GHz band.

There are ample bands to choose from, but the bandwidth criterium eliminates many of the lower frequencies. According to the Shannon-Hartley theorem, displayed in Equation 6.3, the fundamental capacity of a channel is limited by its bandwidth B and its SNR assuming a gaussian white noise distribution.

$$C = B * log_2(1 + \frac{S}{N}) \tag{6.3}$$

Next to this, when FDMA is used, additional bandwidth is required depending on the number of wireless devices to support simultaneously. From the specifications described in Chapter 4, the bandwidth should support 4 animals. For each animal, a different subcarrier frequency is modulated on the main carrier. This subcarrier frequency should be a factor of N higher than the bitrate, where N depends on the minimum number of cycles that are required for each bit. Around each subcarrier, a certain bandwidth is needed to separate the signals from different animals. This bandwidth is a function of the bitrate, guard band, and encoding, which will be further elaborated on in Subsections 6.1.3 and 6.1.5 respectively. In case of a 0.96 Mbit/s bitrate, Manchester encoding and a 500 kHz guard band, about 4.34 MHz of bandwidth is required for each subcarrier.

Table 6.1: Overview of ISM, WMTS, Amateur and MICS bands sorted on available bandwidth [39–42].

Band	f_C **(Hz)**	**Channel (Hz)**	**BW (Hz)**	**Other usages**
ISM	245G	244G-246G	2G	
ISM	122.5G	122G-123G	1G	
ISM	61.25G	61G-61.5G	500M	
Amateur EU	10.25G	10G-10.5G	500M	
ISM	24.125G	24G-24.25G	250M	
Amateur EU	5.75G	5.65G-5.85G	200M	WLAN (5.47G-5725G)
ISM	5.8G	5.725G-5.875G	150M	WLAN (5.47G-5725G)
Amateur EU	2375M	2300-2450M	150M	WLAN, BT (2.4G-2.4835G)
ISM	2.45G	2.4G-2.5G	100M	WLAN, BT
Amateur EU	1270M	1240M-1300M	60M	GLONASS, GALILEO
MBAN	2.38G	2.36G-2.40G	40M	
ISM	915M	902M-928M	26M	GSM (880M-915M)
Amateur EU	1792.5M	1785M-1800M	15M	GSM ($<$ 1785M, $>$ 1805M)
Amateur EU	435M	430M-440M	10M	Sensors, Radiolocation
Amateur EU	3405M	3400M-3410M	10M	Radiolocation
MICS	416M	413-419	6M	
MICS	429M	426-432	6M	
MICS	441M	438-444	6M	
MICS	454M	451-457	6M	
WMTS	611M	608-614	6M	
MICS	402.5M	401-406	5M	
WMTS	1397.5M	1395-1400	5M	
WMTS	1429.5M	1427-1432	5M	

Generally, the higher the frequency, the higher the available bandwidth in a channel. However, at higher frequencies free space loss increases and more power will be needed. Next to this, the commercial antenna designs for high frequencies do not necessarily compensate for the lower link budget caused by the drop in wavelength (Equation 6.2). Another aspect to take into account is the fact that many other devices operate in some of the frequency bands. The most important potential interferers are WLAN and Bluetooth at 2.4GHz and 5.47 GHz and cellular networks between 700 MHz - 930 MHz and 1800 MHz - 1900 MHz depending on the region. Neuroscientists carry around smartphones which they generally do not consider to be a potential hazard for the accuracy and reliability of electronic

Table 6.2: Link budget parameters used in the simulation.

f	P_T	$G_{T,R}$	G_{tag}	X	M	θ / θ_{alu}	B	F_M	F_B
915 MHz	252 mW	12 dB	-4 dB	0.5	0.25	1.2 / 10.4	1	126	32
2.38 GHz	63 mW	18 dB	0.5 dB	0.5	0.25	1.2 / 10.4	1	60	10
5.8 GHz	159 mW	14 dB	-1.5 dB	0.5	0.25	1.2 / 10.4	1	50	6.3

measurements. This could be a potential disadvantage of using the more popular frequencies.

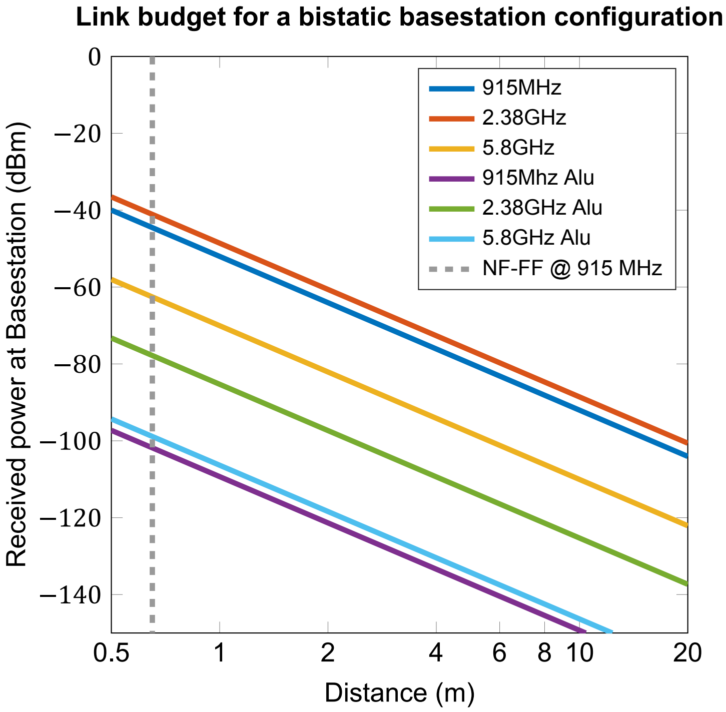

Figure 6.4: Bistatic configuration with different carrier frequencies.

Taking the above considerations in mind, the bands at 2.38 GHz and 5.80 GHz could satisfy the requirements. The 5.80 GHz band has small commercial antennas available, but the 2.38 GHz band is forced to make use of antennas designed for 2.45 GHz (WiFi / Bluetooth). The 902 MHz - 928 MHz ISM band is a lower frequency band that has enough bandwidth to allow 4 subcarriers without a guard band to operate at a bitrate of 0.7 Mbit/s with Manchester encoding. By choosing another encoding method, the 0.96 Mbit/s requirement could still be achieved. The link budgets of these carrier frequencies in a bistatic basestation with passive tag configuration have been plotted in Figure 6.4. Two cases are distinguished for each carrier frequency: low (ideal) on-object gain penalty (θ), and on-object gain penalty associated with aluminum. These values, taken from [43], are listed in Table 6.2. The threshold for far field operation is indicated with the grey dotted line for 915 MHz. Gain values of commercially available antennas for tag and basestation were used in this simulation. As can be seen, the 5.80 GHz band has about 20 dB worse performance than the 915 MHz and 2.38 GHz bands. This is mainly due to the large drop in wavelength, and the commercial tag antenna that can not compensate for this in terms of antenna efficiency.

From all the above considerations and the link budget estimations, the 915 MHz ISM carrier frequency was picked for implementation. It is the lowest frequency band that has enough bandwidth for at least 2 subcarriers at a bitrate of 0.96 Mbit/s, and it could support 4 subcarriers by using another encoding method. Some GSM interference can be present, depending on the region where the device is operated. In The Netherlands, the 900-915 MHz T-Mobile band can cause interference. After downconversion to baseband, this interference is converted to 6 MHz and higher frequencies. This limits the bandwidth in the ISM band significantly. However, during evaluation of the prototype with the Cortex M0+ MCU, it was found that a bitrate of 0.96 Mbit/s is not realizable. This is further discussed in Section 6.4. Consequently, lower bitrates were used for the prototype, relaxing the bandwidth requirements.

6.1.3. Subcarriers

The choice of subcarrier frequencies and spacing is a trade-off between bitrate, Bit Error Ratio (BER) and processing intensity at the receiver side. The number of channels to measure and the sampling rate of those channels have a big impact on bitrate. This section explains in detail the design choices made on the subcarriers, for two different scenarios: measuring 3 channels at 500 Hz sampling rate and measuring 3 channels at 20 kHz sampling rate.

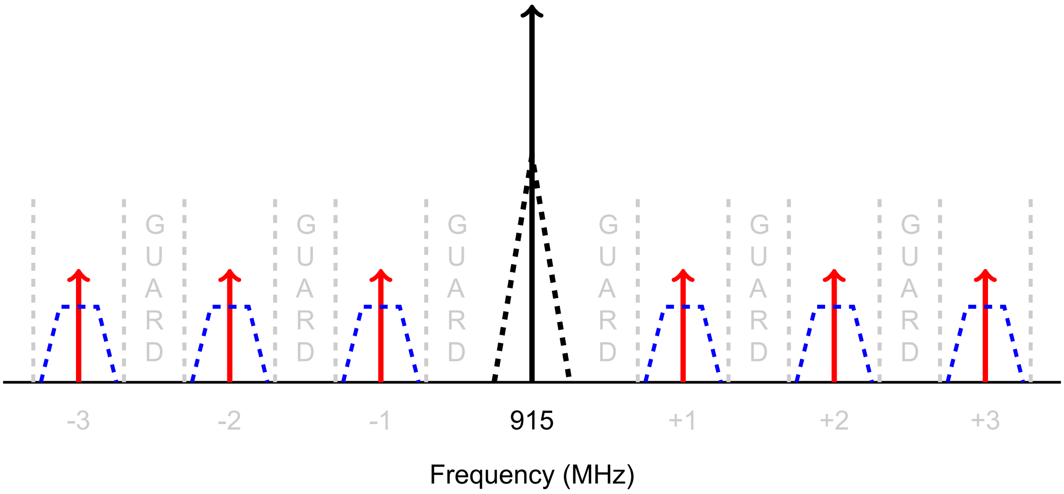

Figure 6.5: Overview of main carrier including phase noise and spectral regrowth, subcarriers and guard bands; power difference between subcarriers and main carrier is not to scale.

The main carrier, three arbitrary subcarriers and guard bands are displayed in Figure 6.5. Around the main carrier some noise is present due to phase noise of the oscillator and spectral regrowth caused by non-linearities in the amplifiers. This will be further discussed in Section 6.2. Guard bands are necessary to protect against co-channel interference [44]. Typical RFID systems in the 915 MHz ISM band use 500 kHz channels separated by 500 kHz [24]. The size of the guard band for this work will be evaluated per scenario.

Sampling 3 channels at 500 Hz

When sampling 3 channels at 500 Hz with a 16 bit resolution, the bitrate is 24 kbit/s. As the frequency spectrum of Manchester encoding ranges to twice the bitrate, the spectrum around the subcarrier spreads from -48 kHz to +48 kHz. Since the modulation signal is a square wave, there will be odd harmonics of this signal that decay with a factor $(2n-1)^{-1}$ in the spectrum. As a starting point for this scenario, a guard band of 200 kHz was chosen, while the bandwidth around the subcarriers taken into account was $\pm$ 200 kHz.

Subcarrier frequency planning can be optimized for maximum guard band size. A geometric optimization with the GGPLAB toolbox by Stanford [45] yields the results of Table 6.3. The optimization was performed for a scenario of the full single-sided bandwidth (915-928 MHz) and of the bandwidth limited by GSM interference (915-921 MHz). For each subcarrier, the 3^{rd} and 5^{th} harmonic are given. Only the harmonics of the lowest subcarrier are potential interferers for the other subcarriers. In case the full ISM band can be used, up to 9 subcarriers can be planned with these geometric rules. Without higher harmonics, up to 20 subcarriers can be planned in this bandwidth. In Figure 6.6, the guard band size is plotted as a function of the number of subcarriers, without taking into account the higher harmonics. This demonstrates the limits of the system in this scenario. To allow for high flexibility and a design with as few discrete components as possible, the subcarrier generation is performed digitally within the MCU. This process is described in Section 6.4.

Table 6.3: Subcarrier planning, units in MHz; 3^{rd} and 5^{th} harmonics are stated for each subcarrier.

13 MHz BW f_{sc}	3^{rd}	5^{th}	**6 MHz BW** f_{sc}	3^{rd}	5^{th}
1.20	3.60	6.00	1.20	3.60	6.00
5.07	15.2	25.3	2.73	8.20	13.7
8.93	26.8	44.67	4.26	12.8	21.3
12.8	38.4	64.0	5.40	16.2	28.0

Sampling 3 channels at 20 kHz
The bitrate in this scenario would amount to 0.96 Mbit/s, resulting in a bandwidth around the subcarrier of ± 1.92 MHz in case of Manchester encoding. To support 4 subcarriers, a higher carrier frequency with more bandwidth or other encoding should be used. As will be discussed in Section 6.4, the MCU is operating above its limits at these bitrates. For these reasons, all experiments are conducted with the low bitrate scenario.

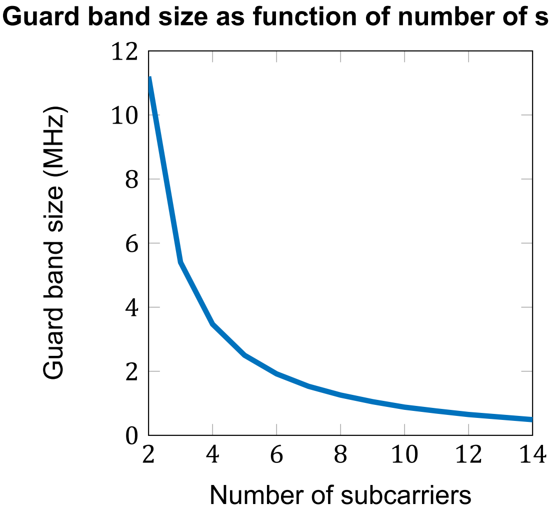

Figure 6.6: Guard band size as a function of number of subcarriers.

6.1.4. Modulation type

As most backscattering systems make use of passive tags with a strict power requirement, the modulation types are often of low complexity. There are two main approaches: Amplitude Shift Keying (ASK) and Phase Shift Keying (PSK). Generally, ASK systems are of lower complexity than PSK systems [23], whereas PSK systems may have a slightly lower BER. On the other hand, ASK might have a slightly greater maximum range. As low complexity is an important design goal for the electronics, ASK was chosen as the modulation method. The simplest form of ASK is used, which is OOK.

The BER can be used as an indication of the performance of a digital communication link. Equation 6.4 states the general equation for BER when a gaussian white noise distribution is assumed [46]. When using a Low-Pass Filter (LPF) instead of a matched filter, the BER deteriorates roughly by a factor of 2. This factor is included in Equation 6.4, as an LPF will be used in this work. Matched filters work based on the assumption that only gaussian white noise is present, whereas interference between subcarriers is expected in this system. With respect to Equation 6.4, E_d is the difference between the bit energy levels and N_0 is the noise power. The term T refers to the time dedicated to transmitting 1 bit, while A indicates the amplitude of the carrier frequency. By increasing this time, BER is improved,

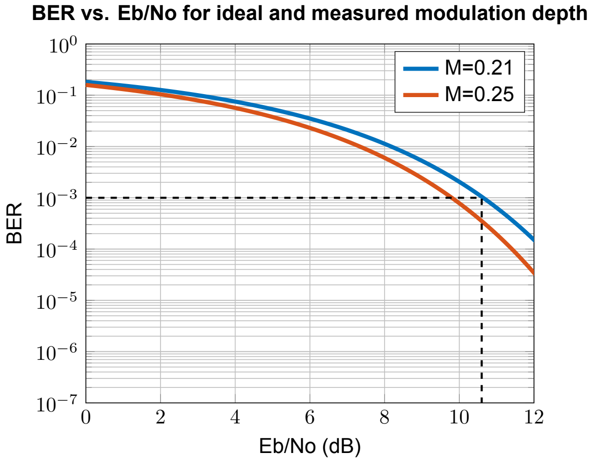

Figure 6.7: BER simulated for theoretical and measured modulation depth.

but the maximum achievable bitrate is reduced.

When employing backscattering, E_d is determined by the modulation states as described in Equation 6.5 [23]. $\Gamma_{A,B}$ are the reflection coefficients, which will be discussed in Subsection 6.1.6. Note that in this equation the subcarrier frequency is used, which means the BER is evaluated after downconversion from the main carrier. By using Equations 6.5 and 6.6, the BER of the system can be written in terms of E_b/N_0 as in Equation 6.7 and plotted in Figure 6.7 for two different values of modulation depth. Ideal reflection coefficients are assumed for the red curve, while measured reflection coefficients are used to calculate the blue curve. Another way to derive E_b/N_0 is stated in Equation 6.8, where CNR is the Carrier-To-Noise Ratio, B is the bandwidth used for the signal, and f_b is the bitrate of the signal. This will be used in Chapter 7 to evaluate the BER.

$$BER = Q\left(\sqrt{\frac{E_d}{2N_0}}\right) \tag{6.4}$$

$$E_{d,backscatter} = \int_0^T [\Gamma_A A \cdot cos(\omega_{sc}t + \theta) - \Gamma_B A \cdot cos(\omega_{sc}t + \theta)]^2 dt = \frac{1}{2} T A^2 (\Gamma_A - \Gamma_B)^2 \tag{6.5}$$

$$E_b = \frac{A^2 T}{2} \tag{6.6}$$

$$BER = Q\left(\sqrt{\frac{E_b}{N_0} \cdot |\Gamma_A - \Gamma_B|^2}\right) \tag{6.7}$$

$$CNR = \frac{E_b}{N_0} \cdot \frac{f_b}{B} \tag{6.8}$$

6.1.5. Encoding method

Encoding methods can improve the detection of bits at the receiving side of a communication channel. Furthermore, the line code has an impact on the spectral properties of the signal [47].

Manchester coding is a low complexity encoding scheme with a transition at every clock cycle and is used in many different communication standards, such as Ethernet [46]. The basic principle is that the data to be sent is modified by an Exclusive OR (XOR) operation with the data clock signal. A disadvantage of Manchester coding is that the spectral bandwidth of the encoded signal has twice the bandwidth of the bitrate.

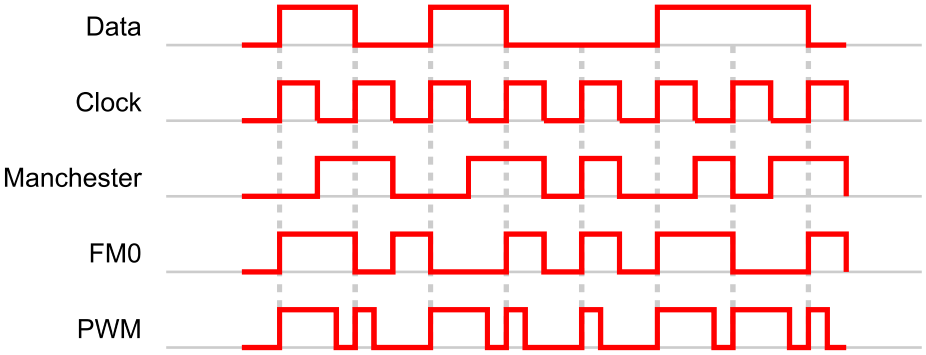

Figure 6.8: Encoding methods compared.

In RFID systems, FM0 encoding is often used [24]. This form of encoding works on the basis of transitions as well. At the beginning and end of each symbol, a transition occurs. A ’0’ has a transition in the middle of the symbol period, while a ’1’ has none. The resulting signal waveform is exactly the same as manchester encoding, although the information is present in a different aspect.

Pulse Width Modulation (PWM) is another encoding scheme used in different electronic systems. Each symbol has the same duration, but the duty cycle is different for each symbol. The trade-off to be made is between the frequency spectrum and the separation of symbols. Pulse Interval Encoding (PIE) is another encoding method that is used in RFID, that is similar to PWM [24]. In the case of PIE the symbol duration is not the same for all bits, which means the transmission time is dependent on the number of bits sent. A schematic representation of the mentioned encoding methods is displayed in Figure 6.8.

It was decided to use Manchester encoding for this work, because of its simplicity. PIE and PWM both have a wider spectrum for the same bitrate, increasing the potential interference between subcarriers.

6.1.6. Antenna systems

For both the basestation and the tag, different antenna configurations have been considered. The designs and their performance are discussed in this subsection.

Basestation

For the basestation, the following design trade-offs were considered:

- Type of basestation antenna
- Linear or circular polarization
- Placement of antenna with respect to cage
- Monostatic versus bistatic antenna configuration

Gain is an important aspect of antennas, that takes into account efficiency and directivity [48]. For this application, an antenna direction towards the floor of the cage, where the animals are moving around, is desirable. The beam width should be wide enough to cover the floor of the cage. Patch antennas have a relatively wide beam angle that covers the floor of the cage with ease. The beam angle might be a bit too wide, resulting in less isolation between the transmitting and receiving antenna. This can be partly compensated by placing the antennas at minima of the wavelength. A commercial patch antenna designed by Taoglas for the 915 MHz ISM band was selected for the first prototype [49].

Taking into account the fact that power will be provided by means of inductive coupling using a coil around the sides of the cage, placing antennas on the side is not an option. The conductive nature of the antennas would alter the field properties of the coil, and have a negative impact on the wireless power transfer. Placing the antennas on the bottom of the cage is not ideal either, as the mice may cause a Non-Line-Of-Sight (NLOS) signal propagation. Therefore, it was decided to place the basestation antennas on the top of the cage. The height of the antenna above the tag antenna was designed to

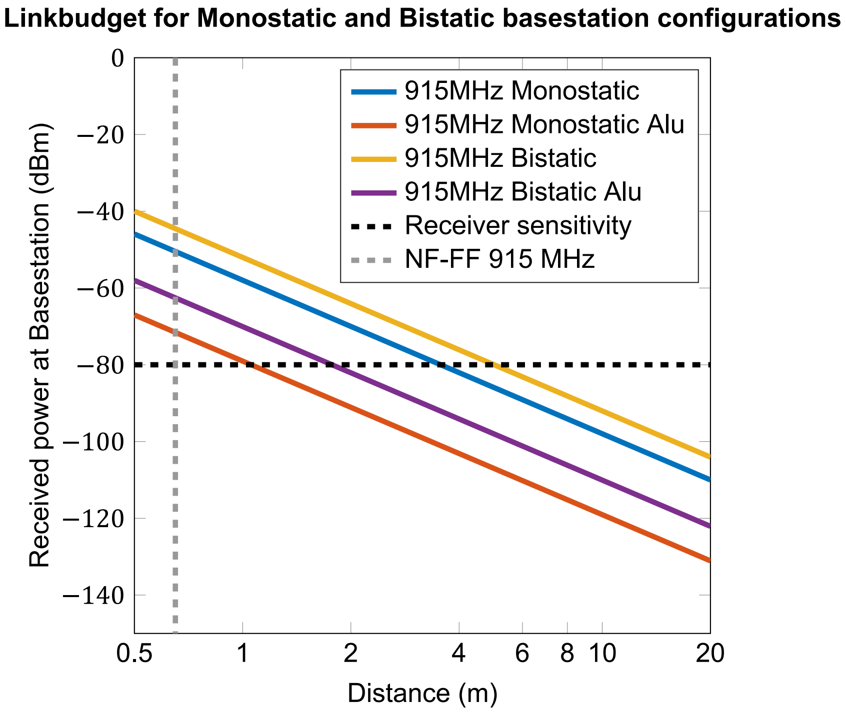

Figure 6.9: Monostatic vs. Bistatic dislocated basestation operating @ 915 MHz.

be 1 wavelength at 915 MHz, which is 32 cm. At every half wavelength there is a maximum for received power. This is near field operation, at the edge of the transition region (Refer to Section A.2 in Appendix A for more). What this means for the design, is that accurate simulation of the antenna configuration would require complex numerical calculation methods. Radiation patterns from datasheets are most often defined for the far field, so their use in the design phase is limited.

Polarization is another important factor to take into account. Linear, circular or elliptical polarization can be used to enhance certain properties of a communication link. The main disadvantage of circular polarization is that it lacks the ability to reduce self-interference between the two basestation antennas in a bistatic configuration [38]. Next to this, circularly polarized antennas exhibit an average signal loss compared to linear polarized antennas. For these reasons, linear polarized antennas were used in the design of the wireless link. The reader is referred to Section A.1 in Appendix A for more background on polarization.

The final important design decision to be made was the choice between a monostatic or bistatic basestation antenna configuration. The performance of a bistatic basestation can be significantly better than a monostatic basestation [38, 50]. In a bistatic design, a distinction can be made based on the spacing between the basestation antennas: collocated (within a few wavelengths) and dislocated basestations. In a monostatic basestation a circulator is needed to isolate the transmitted signal from the low-power received signal. This component offers less isolation than a bistatic configuration. Figure 6.9 depicts the link budget simulation for the different configurations. The bistatic configuration has been modeled for the dislocated case only, using the data from [38]. These models do not apply to the near field, so they should not be interpreted below a distance of 2 wavelengths (grey dotted line in the figure). Antenna gains were used of COTS components that were targeted for implementation in the device. A receiver sensitivity design goal is indicated in the graph with the black dotted line. A design goal of -80 dBm would allow the system to operate in a worst case at a 2 m distance, which is sufficient for the cage environment.

For this work, a collocated bistatic configuration has been used. The prototype cage measured 40 cm by 40 cm, so separation of antennas by more than a couple of wavelengths (n times 32 cm) would not be possible in a practical solution. Even more so because the wireless power transfer works with a

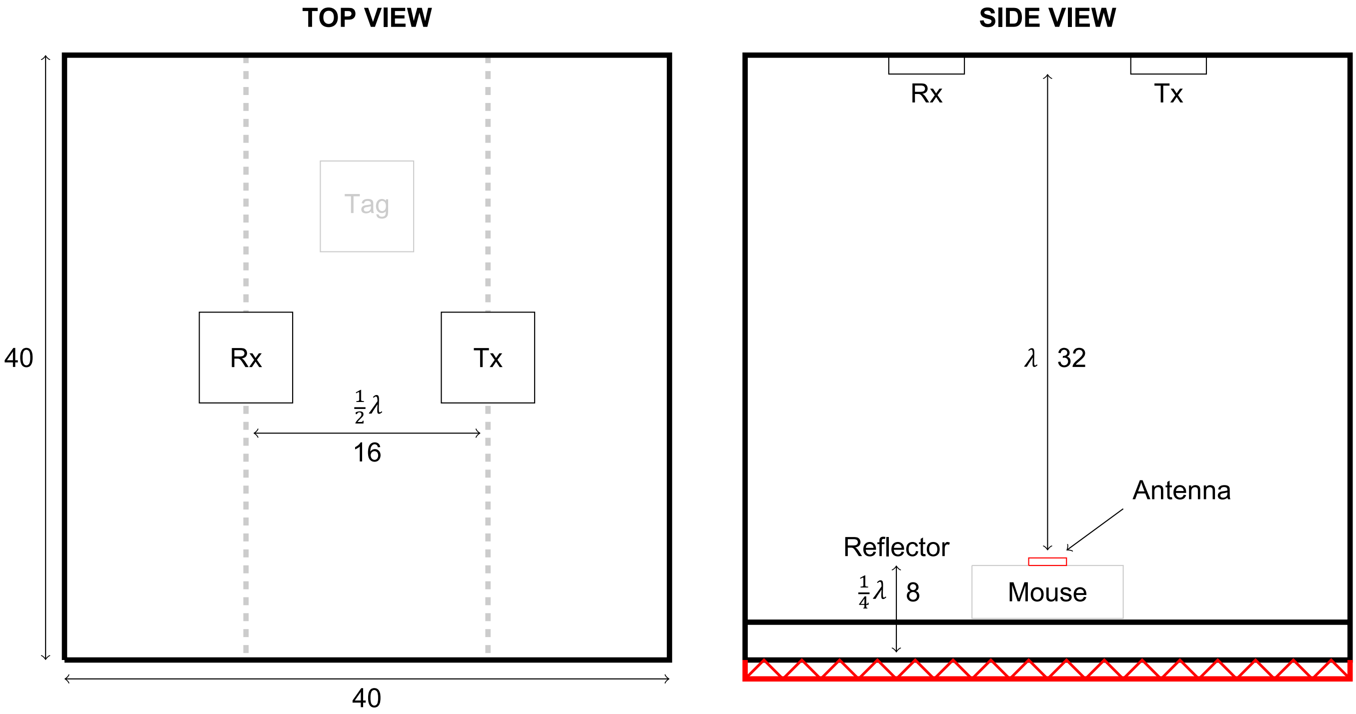

Figure 6.10: Top and side views of the wireless communication set-up in the cage environment, dimensions in cm.

primary coil around the cage that acts as a shield, disturbing the electromagnetic waves traveling from outside of the cage to the inside of the cage. The performance of a bistatic collocated configuration is slightly worse than a dislocated bistatic configuration, but better than a monostatic configuration [38]. The two antennas are spaced by half a wave length, as was experimentally found by varying the distance from 0 to 40 cm. Schematic drawings of the set-up as viewed from the side and the top are depicted in Figure 6.10.

Tag

At the side of the tag, modulation depth and antenna gain need to be maximized within the size and power constraints. The antenna has been selected for minimum size and an omnidirectional radiation pattern. The 0915AT43A0026 antenna by Johanson Technology is developed for small form factor applications of the 915 MHz ISM band, measuring 7x2x0.8 mm [51]. This is a roughly omnidirectional ceramic antenna with an average gain of -4 dBi. A small additional space on the PCB next to the antenna is needed for optimal performance.

The modulation depth of the tag is determined by the impedances used. The impedances ($Z_{A,B}$) can be expressed in a reflection coefficient ($\Gamma_{A,B}$) by normalizing it with respect to the antenna impedance Z_{ANT} (Equation 6.9). These reflection coefficients determine the difference in reflected energy for the 2 modulation states. This difference is called the modulation depth and is defined in Equation 6.10. For maximum depth (M = 1), Z_A should equal 0 Ω (short) and Z_B should approach an infinite resistance (open). On the smith chart shown in Figure 6.11, the short and open are indicated by the green triangle and blue square respectively. However, there is a practical disadvantage in using an open modulation load. Switching to an open circuit can be unreliable at high frequencies [23], leading to an ill-defined modulation impedance. For a more extensive explanation, the reader is referred to [23], Chapter 4. Moreover, when switching between an ideal open and ideal short, a 180° phase change occurs. This means that PSK modulation is performed, instead of the desired ASK modulation. To realize ASK, a matched impedance should be used as one of the modulation loads. In this case, the impedance is matched to the antenna impedance, which is 50 Ω in this work. When the load is matched to the source, maximum power transfer occurs [24], so the load absorbs maximum power from the RF signal. In the smith chart, this impedance is located in the center. When maximum power is absorbed, a minimum amount of power is reflected towards the basestation. The resulting modulation depth ideally amounts to 0.25 in this case.

$$\Gamma_{A,B} = \frac{Z_{A,B} - \overline{Z_{ANT}}}{Z_{A,B} + Z_{ANT}} \tag{6.9}$$

$$M = \frac{1}{4} \cdot |\Gamma_A - \Gamma_B|^2 \tag{6.10}$$

For the switch, different options have been evaluated, based on their speed, on resistance, off resistance and parasitic capacitance. The main finding is that RF transistors are fast enough, but often have a high on resistance, and therefore the modulation depth is reduced. Regular switching transistors are pushed to their operating limit at 915 MHz. The total propagation delay of these discrete transistors could be as high as 100 ns. The maximum switching frequency for the subcarriers would be 12 MHz, which amounts to a pulse width of 41.5 ns at a 50% duty cycle. A rise time in the order of 20 ns or larger is not acceptable in this case. OptiMOS, FemtoFET, NexFET, HEXFET, StriPFET, LDMOS and JFET transistors were examined and simulated in HFSS when models were available.

The best COTS alternative is the ADG901 Single Pole Single Throw (SPST) RF switch by Analog Devices [52]. It is developed to switch high frequency signals at high speeds with low on resistance. The ADG901 has 50 Ω resistors built in one of the switching states, which reduces the need for an external 50 Ω resistor for the matched impedance state. The modulation depth of the switch itself was evaluated using the evaluation board provided by Analog Devices and measured by the HP8753E network analyzer. The results of the two states are plotted as red dots in the smith chart in Figure 6.11. As can be seen, the 50 Ω state is matched quite well with a value of 52.2 + 0.2j Ω in the center of the chart, however, the conducting state is 4.1 - 35.2j Ω. This can be caused by the SMA connectors, PCB microstrips, solder joints and the internal resistance of the RF switch. The datasheet specifies the insertion loss at 1 GHz to be 0.8 dB. The measured insertion loss is equal to 0.95 dB, which is a 20% deviation from the datasheet. Furthermore, a significant parasitic capacitance is present. To put this non-ideality in perspective, the reduction in modulation depth can be calculated. The modulation depth becomes 0.206, which is an absolute modulation depth loss of about 5%, and a relative loss of almost 20%. The imaginary part of the conducting state is in this case not a problem, as it is the absolute distance between the modulation points that determines the modulation depth.

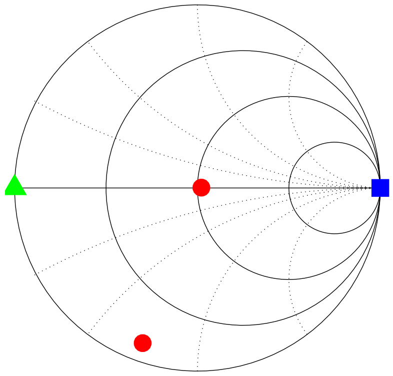

Figure 6.11: Smith chart of measured modulation states; red dots = measured on PCB, green triangle = ideal short circuit load, blue square = ideal open circuit load.

A PCB was developed with the antenna, RF switch and 3 connectors for V_{dd}, GND and the control signal. Via shielding is applied to ensure that the upper and bottom ground planes are at the same potential throughout the PCB. The microstrip running from the antenna to the switch was designed to have a characteristic impedance of 50 Ω to minimize reflections. The layout is printed in Figure D.1 in Appendix D.

6.1.7. Practical RF considerations

In a practical environment, RF communication is influenced by many variables: reflection of the signal by nearby objects, diffraction around nearby objects and orientation of the antennas relative to each other to name a few. In this subsection, these influences are discussed and countermeasures are explained.

The antenna would be moving and tilting due to the movement of the mice. This results in polarization mismatch and consequently deteriorated reception of the wireless signal. An option for making the reception more reliable, is using multiple antennas per tag, oriented in a way such that reception is guaranteed in multiple directions. By orthogonally aligning 2 antennas, 1 vertical and 1 horizontal with respect to the cage floor, reception would be more constant in case the mouse is on its side. This was already suggested as a significant future improvement in RFID systems [50]. In Chapter 7 the effectiveness of using 2 antennas on 1 tag will be demonstrated.

Fading due to reflection can be used advantageously. By using reflectors at a certain distance, the reflected field can create constructive interference, and reduce the influence of other objects around the cage. As depicted in Figure 6.10, a reflector at the bottom of the cage, about a quarter wavelength from the mouse antenna, was implemented to reduce the effect of floor reflections. Reflections by the floor are one of the main contributors to fading in RFID systems [24]. By placing the reflector at a quarter wavelength distance, constructive interference is created at the point of the tag antenna. When the mouse moves vertically, this constructive interference will be reduced. Destructive interference would be maximum if the mouse moves the antenna a quarter wavelength higher. However, as the mice are only a couple of centimeters in length, this situation will not be likely.

Isolating the RF signals within the cage is another option to reduce floor reflections, but at a wavelength of 32 cm, the absorbers would need to be impractically large. The sides of the cage cannot be used as reflectors, as the mouse will move within the cage, destructive interference could occur.

Diffraction will not be an issue, because there are no objects planned in the cage that would block line of sight. For the effect of diffraction, the reader is referred to Section A.3 in Appendix A.

A final concern in this system is the interference between multiple tags. Although FDMA is used to allow the different tags to communicate simultaneously, the antennas in close proximity of each other could still cause a deterioration in signal strength. This will be discussed further in Chapter 7.

6.2. Receiver design

The receiver has been implemented with discrete components provided by Minicircuits. The design schematic is depicted in Figure 6.12. The signal received by the antenna is amplified by a ZRL-3500 LNA and then the ZFY-11 mixer is used to coherently downconvert the signal from 915 MHz to baseband. After low-pass filtering at 32 MHz, the ZHL-6A amplifier further amplifies the downconverted signal with about +25 dB of gain. Finally, the signal is digitized by the Rhode&Schwarz RTO 1044 digital storage oscilloscope. The Agilent 8648C signal generator has been used to generate the 915 MHz carrier at its maximum +22 dBm power output. After splitting this signal (-3 dB) with the ZFSC-2-4 splitter, one part of the signal is fed to the transmitting antenna. The power level would be roughly 19 dBm, resulting in an Effective Isotropic Radiated Power (EIRP) of 20 dBm in the direction of the cage floor. The maximum power allowed in the 915 MHz ISM band is 36 dBm EIRP. This means that there is room for boosting signal power by using a higher power signal generator or an extra amplifier. The mixer which is driven by the other output of the divider can benefit from a slightly higher LO input level, as this would reduce conversion loss. In a first design iteration, an extra amplifier had been used to boost the power, but its maximum output power at the 1 dB compression point would only allow for a 6 dB theoretical gain. The extra gain had been measured to be 4.7 dB, at the cost of higher noise levels and spectral regrowth around the main carrier. Spectral regrowth is caused by non-linearity in amplifiers that generate intermodulation products with the phase noise present in the signal. This could interfere with the subcarriers.

MATLAB has been used to analyze the received data and extract the different subcarriers. This approach to building a receiver, where a large part of the signal processing is performed in the digital domain, is called Software Defined Radio (SDR). A noise analysis of the receiver has been performed to quantify the detection limit of the receiver. This is discussed in the next subsection.

6.2.1. Noise analysis

The component properties are listed in Table 6.4. After referring all noise figures to the input of the LNA, the total noise figure (NF) of the receiver is 2.55 dB. This means that the SNR at the output is 2.55 dB worse than at the input of the receiver. The total gain of the system is 40.3 dB. The receiver detection threshold or *minimum detectable signal* (MDS) can then be approximated by Equation 6.11. With respect to Equation 6.11, k_B is the Boltzmann constant, T_0 is the temperature of the receiver system in Kelvin, B is the receiver bandwidth and NF is the calculated noise figure. With T_0 estimated at 290 K, a receiver bandwidth of 32 MHz and the required SNR set to 10 dB, the MDS equals -86.4 dBm. Based on the link budget simulations, this should be enough. However, the receiver bandwidth can be much lower. Currently, the additional filtering is performed in MATLAB. For a future receiver design, the MDS could be improved to -93.6 dBm when implementing a 6 MHz LPF.

$$MDS_{dBm} = 10 \cdot log_{10}\,(k_B T_0 B \cdot 1000) + NF + SNR_{required} \tag{6.11}$$

Table 6.4: Parameters of the receiver components.

	G (dB)	NF (dB)	$IP3$ (dBm)	$P1dB$ (dBm)
LNA	24	2.2	43	24
Mixer	-7.7	7.7	-	20
LPF	-0.21	0.21	-	-
PA	25	7.6	34	22

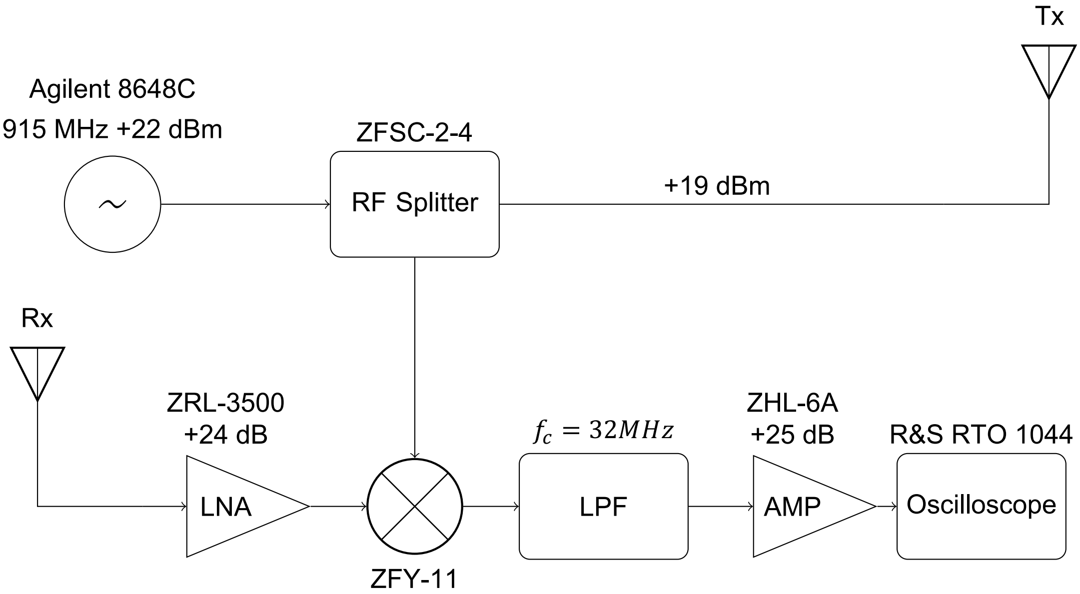

Figure 6.12: Receiver hardware architecture.

6.2.2. Digital implementation

The detection part of the receiver has been built completely in MATLAB. To demodulate the signal from the oscilloscope and eventually extract the data per mouse, the following steps are taken:

- Apply LPF at 6 MHz to reduce noise and GSM-interference
- Apply BPF around $f_{subcarrier} \pm BW$
- Take the absolute value of the Hilbert transform

- Apply LPF with data bandwidth
- Smooth the waveform to improve thresholding
- Calculate dynamic threshold between 0 and 1
- Apply threshold to acquire digital signal
- Decode the Manchester encoding
- Extract the sample data from the packet

The MATLAB code for this approach can be found in Appendix B. The filters are Infinite Input Response (IIR) filters of 10^{th} order, a passband ripple of 0.2 dB and a stopband attenuation of 100 dB. A smoothing factor of 500 kHz is applied. The threshold is calculated dynamically by taking the average over the entire sampling window of the oscilloscope (10 ms). To decode the Manchester encoding, a basic algorithm has been developed that checks the relative timing between signal transitions. This approach does not yield a realtime implementation. That is due to the experimental nature of the hardware used in the set-up. To make this SDR realtime, there are two options: 1) implement a high speed ADC to digitize the signal (replacing the oscilloscope) in combination with an FPGA; 2) perform the subcarrier downconversion to baseband in hardware, and use a slower multichannel ADC to digitize the subcarriers individually. This implementation would need some form of synchronization with the subcarrier frequency to ensure coherent downconversion, making it more hardware intensive.

6.3. Analog front-end

As discussed in Chapter 5, the RHD2132 IC by Intantech has been identified as the best option for a COTS implementation of the AFE. The RHD2132 was placed on a 4 layer PCB, which is shown in Figure D.2 in Appendix D. The AFE has been tested individually and as a part of the total system. For the system level design, a PCB should be developed that integrates the AFE with the MCU, RF Switch, antenna and a voltage regulator. The AFE has been evaluated electrically and in-vivo. To evaluate the AFE and minimize interference, a measurement set-up was constructed to shield and protect the AFE, which is displayed in Figure 6.13. The AFE was placed in a small Faraday cage together with the voltage regulator. Mini-XLR connectors were implemented in the Faraday cage to connect the electrodes with shielded twisted-pair cables. This is necessary to reduce the 50 Hz interference via capacitive and inductive coupling. The RHD2132 communicates with the MCU by means of the SPI interface. Communication with the PC is performed via a UART interface. For an in-depth treatment of the in-vivo measurement set-up for the AFE, the reader is referred to the work of Matthijs Weskin.

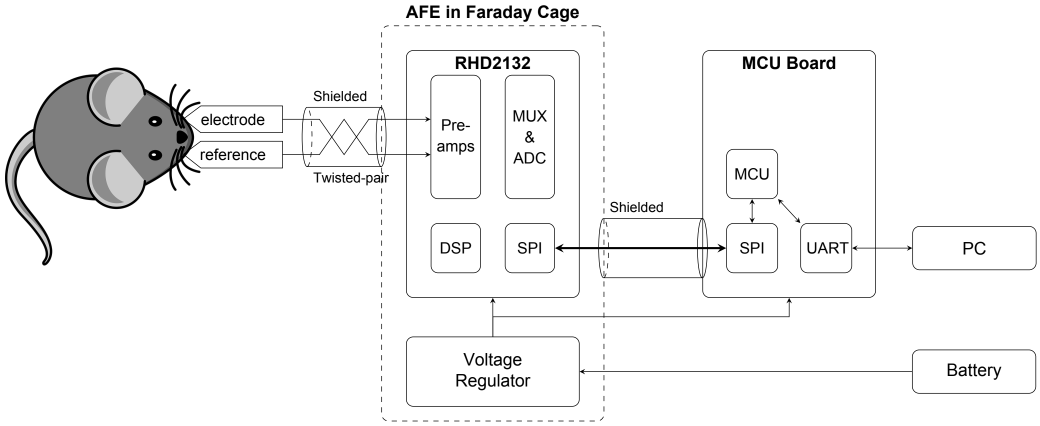

Figure 6.13: AFE system overview, co-authored by Matthijs Weskin.

6.4. Processing unit

As described in Chapter 5, the Cortex M0+ MCU in the NXP Kinetis KL02 package was picked as the central processing unit. To facilitate rapid development, the FRDM-KL02Z development board by Freescale (NXP) was used for programming and debugging the MCU. The main tasks for the MCU are communication with the AFE via SPI at regular sampling intervals and generation of the subcarriers and data packets to be modulated on the carrier by the RF switch.

6.4.1. AFE communication

For this task, the timer and SPI peripherals are used. One of the timer channels generates interrupts at the required sample frequency multiplied by the number of channels that need to be read. The interrupt function initiates the SPI communication, increments the channel counter and calls the data transmission function. When all these functions finish, the MCU is set in wait-for-interrupt (WFI) mode to conserve power until the next interrupt is triggered.

6.4.2. Data transmission and subcarrier generation

This function is more elaborate and multiple options have been explored. As indicated before, a fully digital implementation was preferred to minimize size. Nonetheless, some other options came up during the implementation that are worth mentioning:

- Timer-based, fully digital
- Use SPI/DMA and external logic gates
- Use a Voltage Controlled Oscillator (VCO) and external logic gates

When leaving the chip-select (CS) pin high in the SPI communication, the AFE will ignore the commands sent to it. By using an XOR logic gate that is turned on by the CS pin, the data will be Manchester encoded at the XOR output. By feeding this into an AND logic gate with the subcarrier frequency as the second input, the data signal is modulated on the subcarrier frequency. In this way, the MCU core is idle during data transmission. One important disadvantage is that the SPI clock determines the dataspeed of the transmission, which means that the SPI clock might have to be changed between every sample. A module that can perform the task instead of the SPI module is the Direct Memory Access (DMA) module. The DMA allows outputting data registers on pins, without loading the MCU core. The KL02 implementation of the Cortex M0+ does not have a DMA peripheral, so this could not be tested.

Another, even more hardware oriented approach, would be to use a VCO to generate the subcarrier frequency, instead of the timer module. The VCO can be controlled by the Digital-to-Analog Converter (DAC) onboard the MCU. By using an AND gate with the VCO and data string as input, the data is modulated on the subcarrier. A potential advantage of using a VCO is that the frequency is adjustable in a linear instead of ”binary division” scale of the MCU. Potential disadvantages of a VCO are the frequency error of the VCO and the required resolution of the DAC.

The most compact option is a timer-based fully digital implementation. The working principle is illustrated in Figure 6.14. The timer module counts up to a certain number, M. One of the channels of the timer is set to toggle its output pin when the timer reaches value D < M. When the timer module reaches M, the counter overflows, and the pin is toggled again. In this way, a wave with a certain frequency (by M) and duty cycle (by D) can be created without loading the MCU core. The modulation of the data onto this generated subcarrier frequency is performed by turning the timer output pin on and off. The data has to be encoded to the desired scheme (e.g. Manchester) by the MCU core. The timing of the bits is performed by building in a specific number of ASM NOP commands. The number of NOP commands per bit is determined by the desired bit energy (E_b). The program has been designed with symmetry in mind, so that transmitting a ’1’ costs the same number of instructions as transmitting a ’0’.

As the bitrate increases, the bit energy decreases, deteriorating the SNR and BER. Another effect at higher bitrates is that the amount of NOP commands per bit reduces, making the timing depend more on the execution of the encoding instructions than on the number of NOP instructions. This limits the bitrate to about 320 kbit/s, depending on the required BER. To make sure these issues would not influence the measurements, the low bitrate scenario of 3 channels sampling at 500 Hz was used in all measurements. The measured generated frequencies by the MCU are displayed in Table 6.5. The data was sent in packets of 24 bits, containing 5 header bits and 3 footer bits. In both the header and footer bits 3 consecutive 1's were transmitted. The remaining two header bits were reserved for error correction purposes. Error correction has not been implemented.

Table 6.5: Subcarrier planning with MCU implementation, units in MHz; 3^{rd} and 5^{th} harmonics are stated for each subcarrier.

f_{sc}	3^{rd}	5^{th}
1.20	3.60	6.00
2.10	6.10	10.5
3.00	9.00	15.0

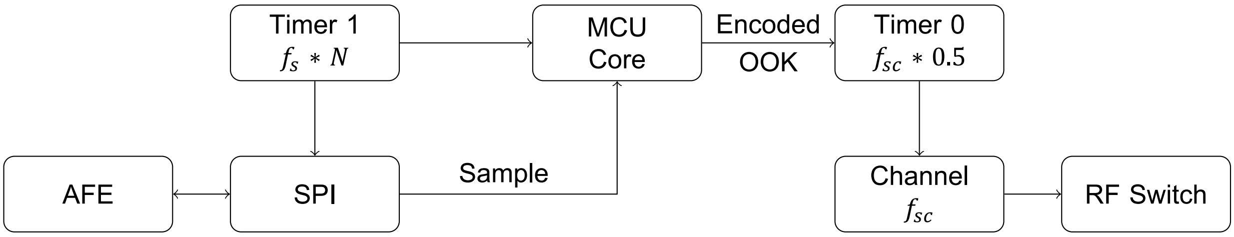

Figure 6.14: Timer-based digital implementation for subcarrier generation.

6.4.3. MCU limitations on bitrate

To achieve the targeted 0.96 Mbit/s bitrate with Manchester encoding, the subcarrier frequency should be set to 1.92 MHz to have at least one subcarrier period in each bit. As discussed in the previous subsection, the timing would not be accurate in this case. Furthermore, bit energy would be reduced, resulting in poor SNR (for a graphical impression of cycles per bit, refer to Figure 6.1). Higher subcarrier frequencies should be used to have enough subcarrier cycles per bit.

The upper limit for subcarrier frequency generation in the MCU is 12 MHz, which constrains the choice of subcarriers (Appendix C states the possible frequencies). As each subcarrier requires at least 3.84 MHz of bandwidth around it, only one other subcarrier can be used in this scenario. To conclude, the current implementation with the Cortex M0+ is limited in two ways: 1) subcarrier frequency generation and 2) inaccuracy of timing at higher bitrates.

6.5. Power management

The power supply has been developed with 3 AA batteries and the 3.3 V fixed LDO LP38690 by TI [53]. This implementation was used to power the AFE and MCU during in-vivo measurements. For the final design, a smaller solution is needed. For the battery, hearing aid batteries could fit the specifications. For example, the Duracell ZA13 Zinc-Air batteries have an energy content of 300 mAh at a voltage of 1.4V with cylindrical dimensions of 7.9x5.4mm. However, in this case a DC-DC converter is needed to boost the voltage to 3.3 V. Watch batteries designed by Seiko are smaller, but have a lower energy content, reducing the time the device can be used without interruption. Another option is to use custom lithium polymer battery packs that operate at 3.7 V, so an LDO can be used. These battery packs can be designed thin and flexible, making them easier to integrate in the final product. As future projects would probably involve integration with a wireless power link, a practical implementation of these options was not further developed.

6.6. Conclusions

In this chapter, the design choices have been discussed per component. For the wireless link, the carrier frequency has been set to 915 MHz. To allow for multi-animal operation, FDMA has been used for its simplicity at the tag side and the fact that synchronization between tags is not needed. Simplicity has been an important design goal for all decisions taken with respect to the wireless link. In Section 6.2, a minimum viable receiver has been designed to evaluate the wireless capabilities. For a functional realtime receiver, a more capable receiver will have to be designed employing either a flexible SDR approach with a high-speed ADC, or a more hardware oriented approach with normal ADCs.

The AFE design that was developed in cooperation with Matthijs Weskin has been briefly analyzed. Proper EMI shielding, careful PCB design and other interference reducing techniques are key to a high performing AFE. The MCU operating procedures have been discussed, showing the limitations of using an MCU with respect to speed and subcarrier frequency generation. In future designs, use of a CPLD or FPGA should be considered. Power management has not been thoroughly discussed, as this work might be combined with the WPT work of Farnaz Nassirinia.

7

Electrical Measurements

In this chapter, the electrical measurements conducted outside of the hospital environment are presented. A subdivision is made between the measurements of individual subsystems (Section 7.1) and the complete design (Section 7.2). For in-vivo measurements, the reader is referred to Chapter 8.

7.1. Subsytems

The measurements of the individual subsystems are discussed in this section. They will be treated in the same order as was done in Chapter 6.

7.1.1. Wireless link

To test the wireless link systematically, a grid set-up was built, using a reversed wooden table, wooden planks, painting tape, and markers. This is displayed in Figure 7.1. A grid of 3 by 3 measurement points was used. Figure 7.1a shows a photo of the set-up, while Figure 7.1b explains the measurement points. The numbers in circles represent tag positions, while the combination of letters and numbers in squares represent basestation antenna positions. The following measurements will be elaborated on in this section:

- Basestation
  - Orientation of antennas
- Single tag
  - One antenna
  - Two antennas
  - Placement
  - Orientation
- BER
- Multiple tags
- Measurements in the Wireless Power Transfer (WPT) cage

Basestation

What lacks from this list is a variation of basestation antenna positions. The reason for this is that there are not many options to do so. As explained in Subsection 6.1.6, the sides and bottom of the cage are not an option. The antennas should be spaced apart by half a wavelength, and by symmetry, a centralized position in the cage is best for overall performance around the cage. Since it is a symmetrical structure, the positions of the transmitting and receiving antennas can be interchanged. This has been verified by experiments. What remains is the rotation of the antennas relative to each other. In this

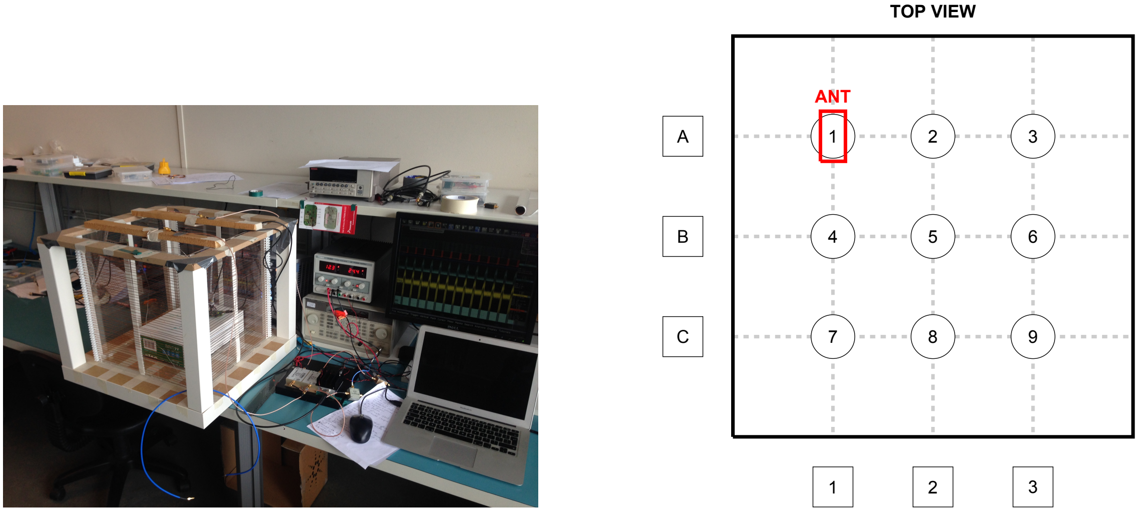

(a) Measurement set-up.

(b) Measurement points in the cage environment; circles represent tag positions, while the combination of squares yield basestation antenna positions.

Figure 7.1: RF measurement set-up.

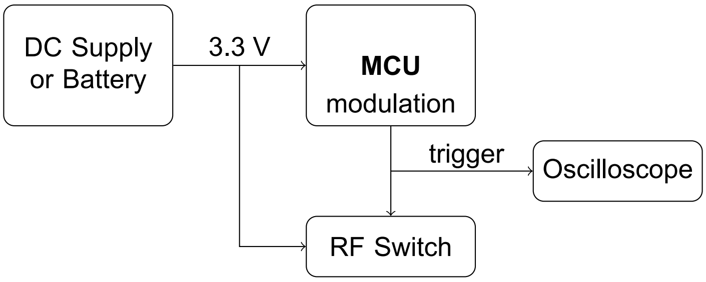

Figure 7.2: Set-up of the electronics at the tag side during measurement.

regard, the following observations were made. When aligning the antennas in the same plane at an angle of 0° or 180°, the ideal spacing is $\frac{1}{2}\lambda$. When aligning the antennas at an angle of 90° in the same plane, the ideal spacing is $\frac{1}{4}\lambda$. Since the antennas are placed within each others near field, electric and magnetic fields are not well characterized. Strong destructive interference can occur when placing the antennas at a certain distance of each other. Therefore, the ideal spacing of the antennas was empirically determined by observing the signal strength of the FDMA sidebands.

Single tag

To allow for a visual performance comparison between positions, orientations and the number of antennas, four different situations have been measured on a measurement grid. The four situations are the following:

- **Normal**: tag antenna aligned with grid, facing north as indicated in Figure 7.1;
- **90H**: 90° rotated in the horizontal plane compared to normal;
- **90V**: 90° rotated in the vertical plane compared to normal;
- **2 Antennas**: 2 orthogonally oriented antennas are used to backscatter.

The signal generator was set to +22 dBm output power and the basestation antennas were placed in the same plane on the A2 and C2 positions, with a 180° orientation. The PCB with antenna and RF switch, connected to and powered by the MCU, was placed on specific points of the grid (Figure 7.2).

The grid measurement data is represented in Figures 7.3 and 7.4 as follows. The signal from the oscilloscope is filtered ±200 kHz around the subcarrier at 4.8 MHz using a 10^{th} order IIR bandpass filter. Using the MATLAB function *bandpower*, the energy contained in this bandwidth is calculated. By then plotting these energies in a heatmap, an estimate of the distribution of the backscatter signal strength throughout the cage can be acquired. All measurements have been conducted with the same sample size and sampling rate, within a short time span of each other. Figure 7.4 contains the same information as Figure 7.3, but with the scale normalized to the combined range of all four situations.

As can be seen in Figure 7.4, the overall signal strength is much better while using two orthogonally aligned antennas. This is to be expected, as the orthogonally aligned antennas can compensate for each others weak spots. The 90V rotated configuration performs better than the other two alignments in terms of absolute power received. The relative variability in signal strength throughout the cage is similar for all cases except the 90V case. In all the graphs, the signal strength seems to be increasing from the left side to the right side. At the right side of the cage there was no object present within 2 meters that could serve as a strong reflector. However, the signal generator, oscilloscope and other measurement devices could be influencing the field in this way. To reduce the influence of the environment on the measurements, tests in an anechoic chamber should be conducted. This has not been done in this work.

BER

In order to measure the Bit Error Rate (BER), a dataset of 2 seconds was saved, amounting to 3000 packets. With 24 bits per packet, this amounts to 72 kbit (order of 10^5 bits). The test was conducted with the sample data $0xAA55$, which corresponds to alternating 1's and 0's. The sample rate was 50 MSa/s and the same filter specifications described in Section 6.2 have been used. By demodulating in MATLAB, a Bit Error Ratio (BER) in the order of 10^{-3} can then be estimated. One effect that might influence the BER negatively is the fact that to sample so many packets, the oscilloscope triggers samples of 75 packets consecutively. Sometimes the trigger is not performed correctly and the first packet of the 75 packets is corrupted by the triggering itself. This problem will not occur when a real-time receiver is used, which will be discussed in the recommendations. As discussed in Section 6.2, the Manchester decoding algorithm could not handle large datasets well. For this reason, an alternative approximation of the BER was done by using the definition for CNR stated in Equation 6.8. The subcarrier-to-noise ratio (SCNR) is calculated to be 7.45 dB from the data of Figure 7.6 and approximating the white noise from the receiver noise analysis. Assuming a bandwidth of 200 kHz and bitrate of 85.7 kBit/s, the E_b/N_0 is estimated to be 13 dB. When using the measured reflection coefficients $\Gamma_{A,B}$, this yields a BER of $5.4 \cdot 10^{-4}$. However, imperfect matching of the antenna to the switch and other non-idealities are not taken into account, so this could serve as a best case indication for BER.

Measurements in WPT Cage

Measurements in the WPT cage, constructed by Farnaz Nassirinia, have been performed to get an indication of the effect of the primary coil on the performance. This is important, because in future work, this work may be integrated with the work of Farnaz Nassirinia. The primary coil of the WPT

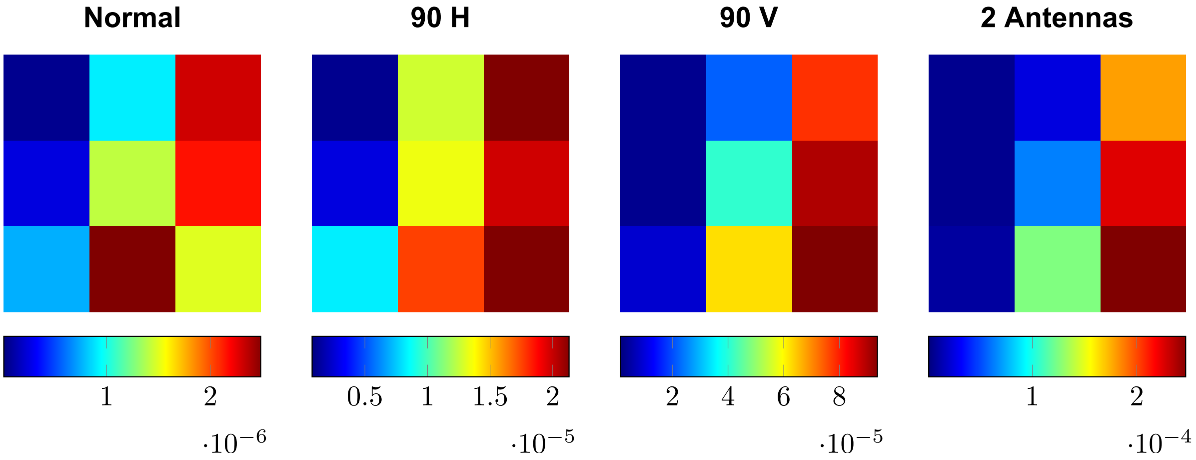

Figure 7.3: Different tag configurations, color mapping per configuration; units in W.

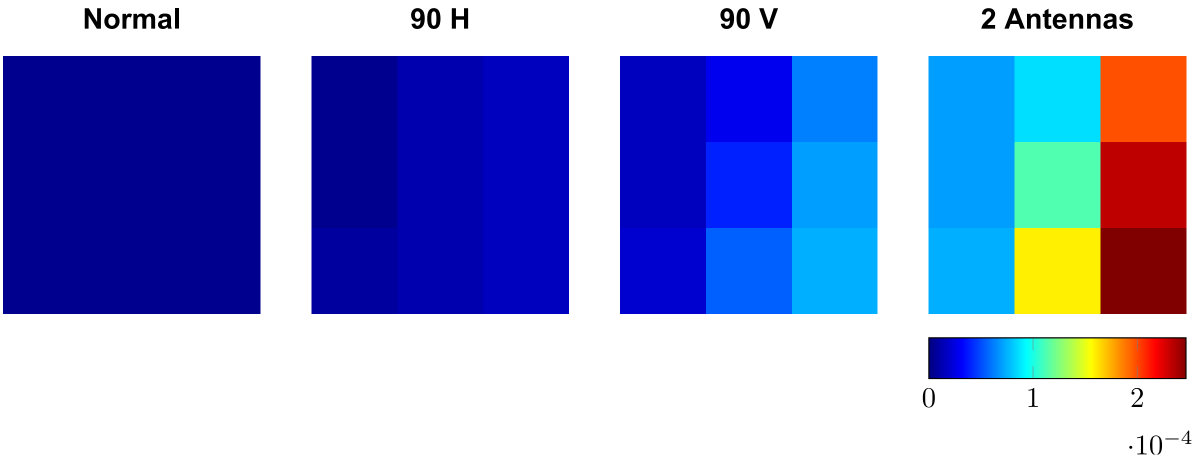

Figure 7.4: Different tag configurations, equal color mapping for all configurations; units in W.

system is wound around the cage from top to bottom with a spacing of 0.5 cm between wires. It was expected that the primary coil would have a detrimental effect on the received signal power. The cage is closed on all sides, except for the top, so the connections between the DC power supply and the oscilloscope had to run vertically through the cage. The wires caused some amplitude variations in the receiver. Therefore, measurements with a battery powered solution were performed as well. The results of these measurements are plotted in the heatmaps of Figure 7.5, using the same color mapping. The wired solution performs worse by almost an order of magnitude. When comparing the scale of this heatmap with that of Figure 7.3, the signal strength within the cage is orders of magnitude lower in some places. This could mean that when integrating the WPT with the wireless communication of this work, the system might function less effectively. However, in a final design it could be considered to use a battery instead of WPT. This is further discussed in Chapter 9.

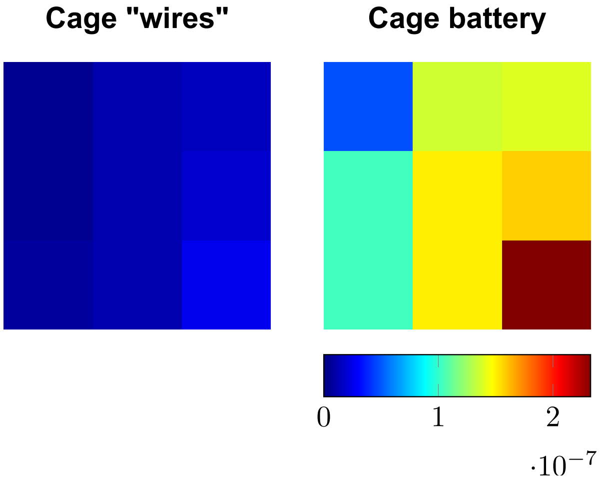

Figure 7.5: Measurement in cage, using battery power and wired power, equal color mapping; units in W.

Multiple tags

This section demonstrates the use of multiple tags that simultaneously transmit data. A test with 2 tags had been conducted as a first step, but those results are not presented in this work. The maximum amount of tags tested was 3. The signal after downconversion from the main carrier, along with its frequency spectrum, is depicted in Figure 7.6. Peaks in the frequency spectrum can be seen at 1.2 MHz, 2.1 MHz and 3 MHz. In Figure 7.7, the frequency spectrum around the main carrier is displayed. The 3 subcarriers are indicated by the red crosses. Strong interference from the GSM band can be seen starting at 922 MHz and higher. After downconversion to baseband, these are present at 6 MHz and higher. This is an important reason to avoid using subcarrier frequencies above 5 MHz and a severe limitation of using the 915 MHz ISM band outside of a shielded environment. With the SDR receiver designed in MATLAB, the individual subcarriers are separated, demodulated and decoded. The result of this can be seen in Figure 7.8, displaying the $0xAA55$ sample. The time axes of Figures 7.6 and 7.8 are the same. As can be seen, the three tags are transmitting their sample almost simultaneously, yet it is still possible to retrieve the information of both tags in the receiver. This demonstrates that the concept of FDMA applied to backscattering has succeeded.

Closer to the carrier frequency, the noise power increases. As discussed in Section 6.2, this can have multiple reasons: 1) phase noise of the oscillator 2) spectral regrowth caused by non-linearity in the LNA and 3) mixer $1/f$ noise. Spectral regrowth is minimal, because the additional LNA suggested in 6.2 has not been used. The slope around the main carrier ranges to $1/f^2$, indicating that it is probably caused by oscillator phase noise. After downconversion, the effect seems to have reduced significantly. The reason for this is that the phase noise of the mixer LO input and the mixer RF input are originating from the same signal source. This makes the phase noise highly correlated. This correlation causes a cancellation of phase noise in the mixer. The 1.2 MHz subcarrier power level is about 3 dB higher, but this could be caused by the placement and orientation of the tag as well.

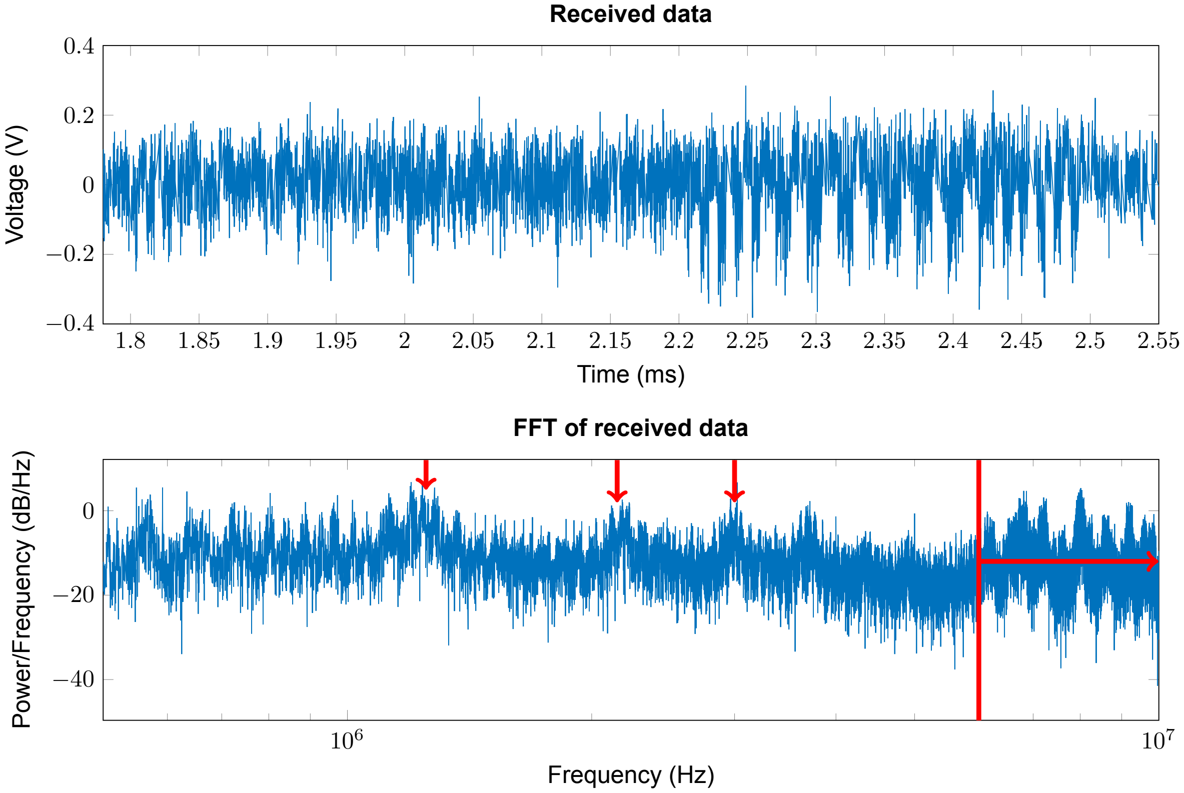
Received data

FFT of received data

Figure 7.6: Received data in in the oscilloscope of 3 tags, around baseband; vertical arrows indicate subcarriers, right arrow indicates GSM interference.

The bitrate of each subcarrier is in this case 85.7kHz (24 bits are sent in 0.28ms). Manchester encoding is used, which means the spectrum ranges to 170.4kHz. The tags were filtered in a ± 200 kHz bandwidth around each subcarrier. In this measurement, the tags were evenly spaced throughout the cage, to create a distance of at least 10 cm between them. By empirically placing and orienting the tags, it was made sure that the signal levels of the 3 tags were roughly the same. The first subcarrier at 2.1 MHz is about a factor of 2 stronger, but this poses no problem to the filtering performed in the receiver. Further testing was done to find out to what extent the receiver can handle the near-far issue. At a subcarrier power difference of 10 dB, the subcarriers can still be filtered up to a point that they are distinguishable, but bit errors are present in every sample of the weaker subcarrier. The reason for this is that it becomes harder to set a bit decision threshold due to the interference of the strong subcarrier

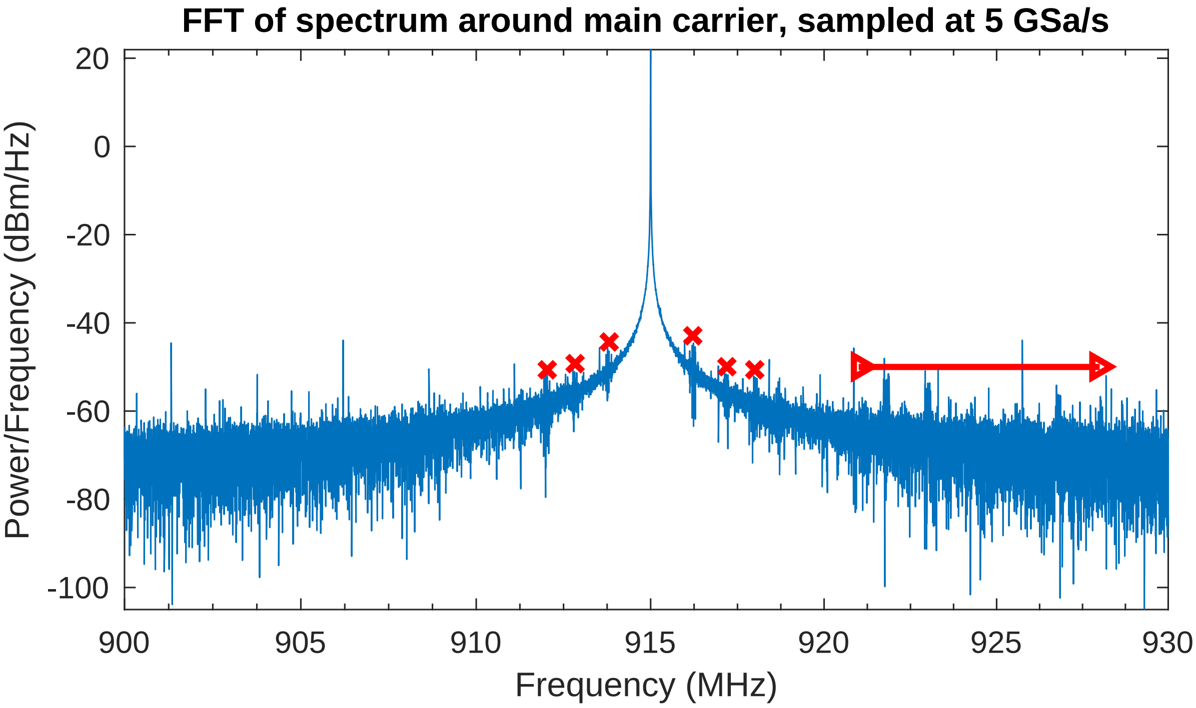

Figure 7.7: Received data in the oscilloscope of 3 tags, spectrum from 900 - 930 MHz; subcarriers are indicated with 'x', while GSM interference is visible on the right, indicated by the arrow.

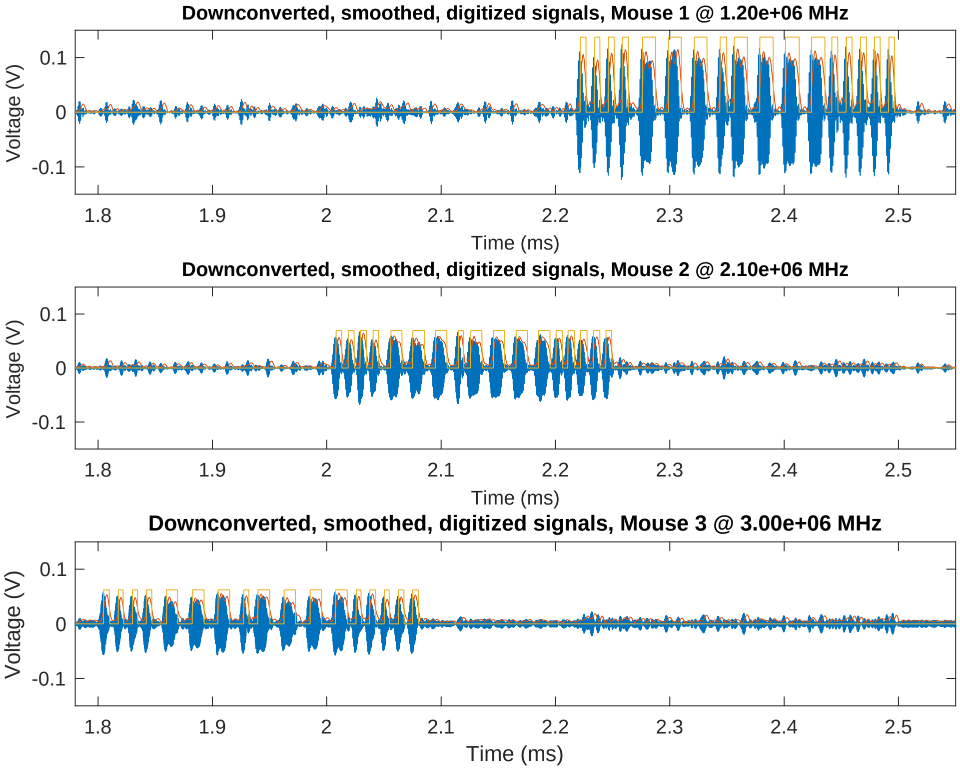

Figure 7.8: Received data in in the oscilloscope of 3 tags, demodulated per subcarrier. Subcarriers signal power is in same order of magnitude.

that is present in the filtered signal of the weak subcarrier. Figure 7.9 shows the near-far effect in the receiver. The subcarriers at 1.2 MHz and 3.0 MHz can be adequately filtered, but the subcarrier at 2.1 MHz is suffering from interference. The extent up to which the system can handle the near-far issue is

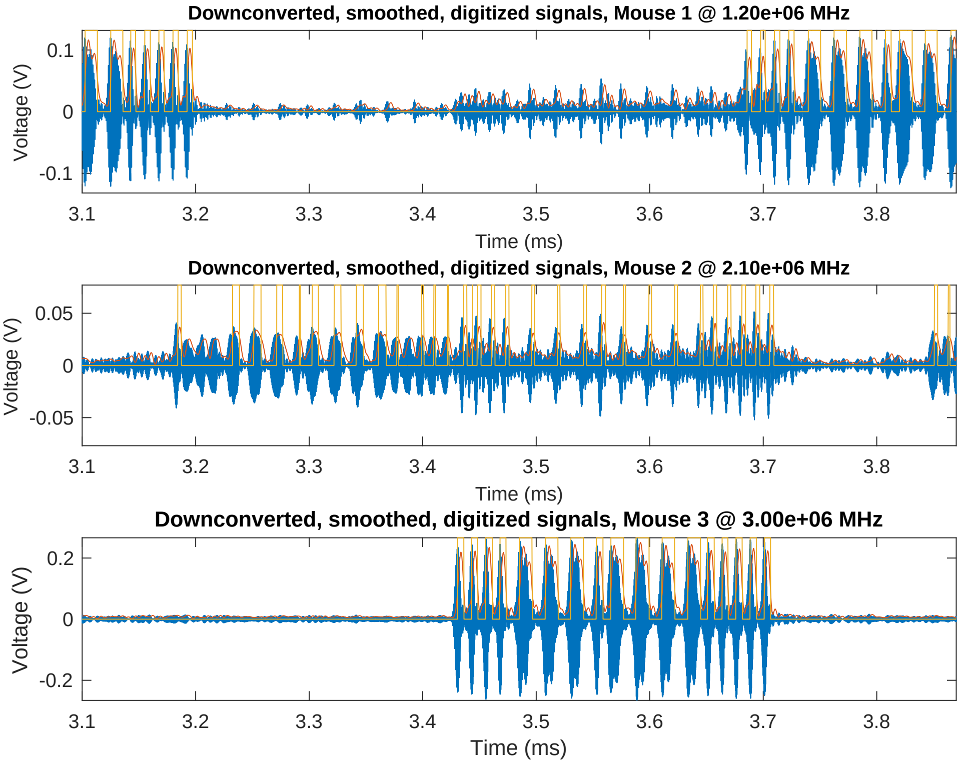

Figure 7.9: Received data in in the oscilloscope of 3 tags, demodulated per subcarrier. Subcarrier signals exhibit 10 dB signal power difference.

determined as well by the guard band between the subcarriers and the higher harmonics.

The antennas could be spaced close to each other or even on top of each other due to behavior of the mice. This will create near-far situations in the receiver as well. By using multiple antennas on all tags, the received signal of the tags will be varying less, and the near-far problem could be reduced. If this is enough to have a reliable link that keeps performing when mice are very close to each other is subject for future research.

7.1.2. Analog front-end[1]

To characterize the AFE, the set-up of Figure 7.10 is used. The Applicos ATX7006 measurement device contains a 20-bits arbitrary waveform generator (AWG20). The waveform generator is connected via

---

[1] This section is partly co-authored by Matthijs Weskin.

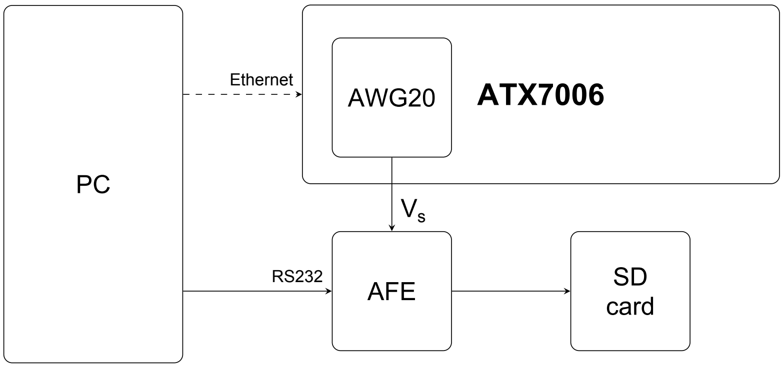

Figure 7.10: Schematic overview of measurement set-up to characterize the Analog Front-End (AFE). The PC controls the ATX7006 via Ethernet and the AFE via RS232. A waveform generator (AWG20) generates a signal to the AFE, which saves data to its SD card.

a custom made shielded twisted pair cable to the AFE, which saves the data to its SD card. Both the waveform generator and the AFE are configured and controlled by a computer (PC).

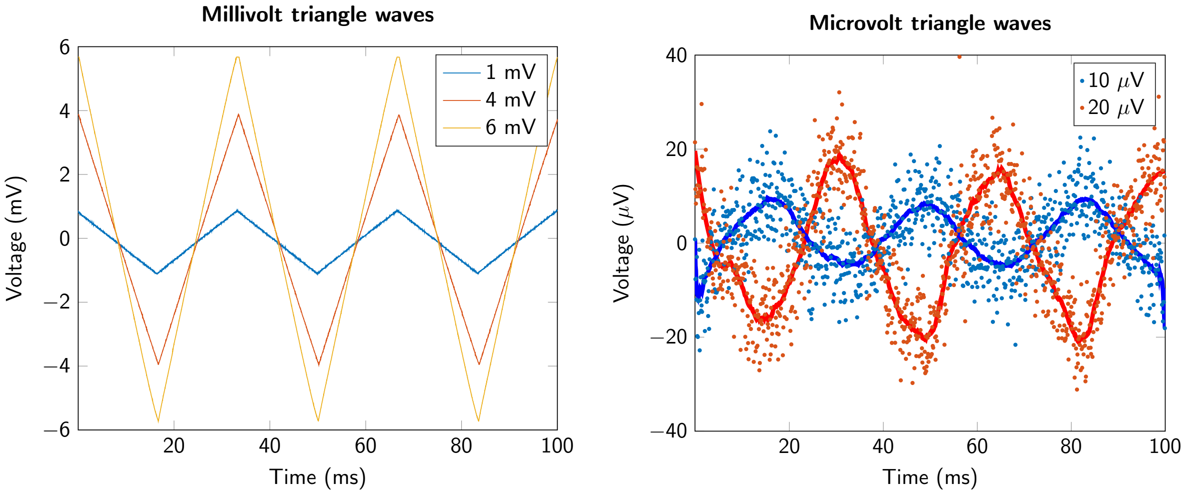

(a) Digitized signal measured with AFE for a triangular input signal with frequency $f = 30$ Hz and amplitudes $V_s = 1$ mV (blue), 4 mV (red) and 6 mV (orange).

(b) Digitised signal measured with AFE for a triangular input signal with frequency $f = 30$ Hz and amplitudes $V_s = 10$ μV (blue) and 20 μV (red).

Figure 7.11: Transient performance of the AFE.

Two sets of measurements are performed. First the linearity of the system is characterized with a triangle wave with different amplitudes ($f = 30$ Hz, $V_s = 10$ μV, 20 μV, 1 mV, 4 mV and 6 mV). The measured triangle waves are shown in Figures 7.11a and 7.11b. At the specified maximum input amplitude of the AFE ($V_s = \pm$ 5.0 mV), the signal is still amplified. With a slightly higher input voltage ($V_s = \pm$ 6 mV) the signal is attenuated and clipping. Reaching the lower limits of the AFE in Figure 7.11b, a triangle wave is still distinguishable, but it becomes distorted and the noise amplitude reaches the same amplitude as the signal ($V_n \approx 10$ μV).

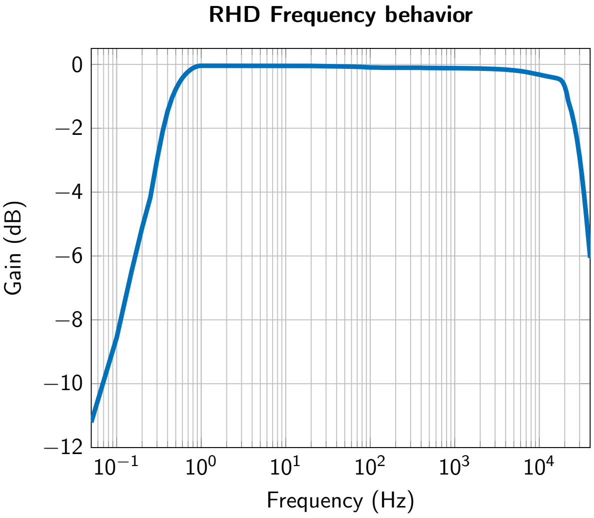

Figure 7.12: Frequency behavior of the AFE.

The second measurement was performed to determine the frequency behavior of the AFE. Sine waves with a constant amplitude and varying frequencies have been applied ($f = 0.5$ Hz to 30 kHz, $V_s = 1$ mV). The frequency behavior is analyzed in MATLAB and plotted in Figure 7.12. The desired bandwidth (1 Hz to 10 kHz) is reached. The signal is slightly attenuated with raising frequency (0.3 dB at 10 kHz, 0.5 dB at 20 kHz), but the passband remains between ± 0.5 dB.

In MATLAB the SNR and the Total Harmonic Distortion (THD) have been analyzed. The SNR (input signal: sine wave, f = 140 Hz, V_s = 1 mV) is 38 dB. This corresponds to a noise level of 8.9 μV_{rms} over the bandwidth of the AFE (30 kHz). The waveform generator and the amplifier in the AFE (the amplifiers of the RHD2132) both introduce noise. The datasheets don't specify an equivalent input-referred noise (in $V/\sqrt{Hz}$). All parts of the system (ATX7006 and RHD2132) must be analyzed further to draw conclusions on the origin of the noise. If the ATX7006 is the main noise contributor, the AFE has a higher SNR than calculated in MATLAB. Furthermore, the bandwidth can be reduced to increase the SNR. The bandwidth is 30 kHz, but can be reduced to 10 kHz. A reduction of the bandwidth with a factor 3 can result in a decrease of a gaussian noise source voltage by a factor $\sqrt{3}$. Increasing the lower cut-off frequency can reduce the effect of 1/f-noise. In this way, the specification of 40 dB set in Chapter 4 is achievable. The THD (input signal: sine wave, f = 140 Hz, V_s = 1 mV) is -46.72 dB.

7.1.3. Processing unit

In this subsection, the performance of the processing unit is evaluated in terms of power, speed and quality of the generated subcarriers.

The modulation output of the MCU is displayed in Figure 7.13. The first thing to note is that the duty cycle of the square wave is around 58%, which means that the composition of the generated harmonics will change. The RF switch threshold is roughly at 1.4 V, meaning that this duty cycle is present in the reflected signal. At an exact 50% duty cycle, only odd harmonics are generated. When deviating from 50%, even harmonics are generated as well. The reason for the duty cycle not being 50%, lies in the fact that the timer module is operating close to its maximum frequencies. The middle transition is triggered by a channel compare value, while the other transition is triggered by the timer overflow value. These might be different operations in the MCU, causing the time difference.

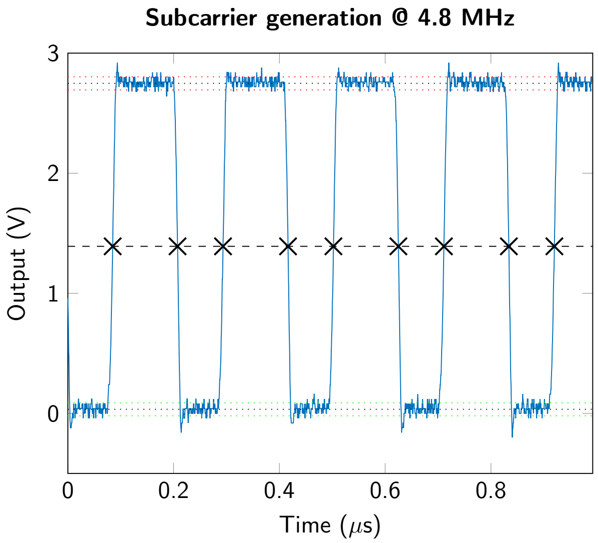

Figure 7.13: Duty cycle measurement of the subcarrier generated by the MCU.

The power consumption of the MCU was measured while sampling 1 channel at 500 Hz. A special jumper on the development board is used that is dedicated to the MCU only. When run from a 3.3 V supply the power consumption is 10.9 mW. When increasing the sampling rate, the standby time of the MCU is reduced, increasing the power consumption. At 20 kHz sampling of 1 channel, this results in a power consumption of 16.8 mW. On the other hand, the standby time can be increased by reducing the time per transmitted bit. However, this will negatively impact the BER, as discussed in Subsection 6.1.4.

As shown in the previous subsection, the SNR of the AFE is about 38 dB. The samples contain 16 bits, which can handle a maximum SNR of roughly 100 dB, limited by quantization noise. By reducing the number of bits sent over the wireless link, the bitrate is reduced, and therefore power consumption and bandwidth are reduced. Depending on the purpose of the recordings, the resolution can be reduced by a different amount. For seizure detection, 8 bits would probably be enough. For closer inspection of the ECoG in between seizures, 12 bits would probably suffice.

7.2. Complete design

The complete design was tested to check the power consumption and make sure that the MCU communicates properly with the AFE. The power consumption without LDO was measured. An overview of these measurement results is listed in Table 7.1. As can be seen, the power consumption is roughly increased by 6 mW when sampling at 20 kHz. Most of the additional power consumption is caused by the MCU, which barely goes into standby mode when sampling at 20 kHz. The power consumption of the RF switch of 0.25 mW barely contributes to the total power consumption. Compared to a conventional RF transmitter that can consume 10's of mW's, the use of backscattering clearly results in a big reduction of power consumption.

Table 7.1: Power consumption of the complete system.

	500 Hz, 1 CH	**20 kHz, 1 CH**
MCU	10.9 mW	16.8 mW
MCU + RHD	14.25 mW	20.1 mW
MCU + RHD + RF	14.5 mW	20.3 mW

7.3. Conclusions

The design has been evaluated electrically in this chapter. Wireless performance has been assessed across the cage environment, and the performance improvement when using 2 antennas per tag has been demonstrated. When analyzing the spectrum around the main carrier, it has been found that GSM interference at 921 MHz and higher is an important downside to using the 915 MHz ISM band. The GSM interference is different per region, but may be reduced by working in a shielded environment. The simple SDR created in MATLAB can demodulate and decode the different subcarrier signals, but for large datasets, systematic errors add up and make accurate BER evaluation impossible. A rough estimation of the BER based on the measured CNR, bandwidth and bitrate yields a BER of $5.8 \cdot 10^{-6}$, which would be impressive for an RFID system. However, this is an indication of best case performance.

Linearity, frequency behavior and the SNR of the AFE have been analyzed. The AFE can operate from 20 μV to 5.0 mV. THD is -46.72 dB with a 1 mV sine wave at 140 Hz. The built-in filters of the RHD2132 work properly, although the order of the filters is low and additional digital filtering is needed. A slight passband attenuation of -0.5 dB occurs at 10 kHz and higher frequencies. The approximate SNR is 38 dB with a 1 mV sine wave at 140 Hz. Some parts of the measurement set-up introduce noise, which means the true SNR of the AFE can be higher.

The MCU has been evaluated in terms of power consumption and subcarrier generation. Because the MCU is operating at its limits, the duty cycle is not exactly 50%. For a 4.8 MHz subcarrier, the duty cycle has been measured to be 58%, which means some even harmonics are generated next to the odd harmonics. This increases interference between subcarriers. The power consumption of the total system at a 500 Hz sampling rate equals 14.5 mW, while it is 20.3 mW at a 20 kHz sampling rate. The most significant contribution to power consumption (more than 75%) is due to the MCU. The wireless link has a power consumption of 0.25 mW (2%), which proves that by using backscattering wireless communication, power consumption can be reduced drastically compared to conventional transmitters.

8

In-vivo measurements[1]

In this chapter measurement results of the Analog Front-End (AFE) in the hospital are presented. A subdivision is made between the different measurements that are conducted by the Erasmus Medical Centre (EMC) neuroscience department. The complete system including wireless transmission could not be tested in-vivo, because an integrated miniature version that can be carried by a mouse was not finished in this work.

Three different set-ups have been tested with the AFE: 1) an ECoG cortex electrode 2) a single cell action potential recording 3) an invasive inferior olive recording. For an in-depth analysis of the inferior olive measurements, the development of the custom electrodes for these measurements and analysis of the EMC measurement set-up, please refer to the MSc Thesis of Matthijs Weskin. All measurements were sampled at 60 kHz, one channel at a time. For debugging purposes, the R&S RTO 1044 oscilloscope was recording the audio output of the MCU. This audio output was duplicating the channel recording. The different measurements will be described in the following subsections. A schematic overview of the measurement set-up is depicted in Figure 8.1.

Figure 8.1: Overview of the measurement set-up in Erasmus MC with the AFE connected.

8.1. ECoG

For the ECoG measurements, custom twisted-pair shielded cables were developed to connect the front-end to the electrodes mounted on the mouse head. In the basic recording, one channel was recorded, while the other electrodes were left disconnected. In a measurement to compare this work to the current set-up at Erasmus MC, a splitter was made to be able to measure the same channel with two set-ups. A side-effect of this measurement was that there would be more loading of the source, possibly deteriorating the signal quality. A reference measurement was conducted as well, with the set-up in the same place, but with a disconnected electrode. The set-up is displayed in Figure 8.2. All measurements were conducted with a mouse that has frequent absence seizures, identified by Generalized Spike and Wave Discharges (GSWDs) in the cerebral cortex.

---

[1] This chapter is partly co-authored by Matthijs Weskin.

Table 8.1: Filter specifications

Band pass filter	
Filter response	Infinite Impulse Response
Filter type	Band-pass filter
Filter order	10
Cut-off frequency (low)	0.5 Hz
Stopband attenuation (low)	50 dB
Cut-off frequency (high)	100 Hz
Stopband attenuation (high)	50 dB
Passband ripple	0.2 dB

As a tryout, the audio output of the RHD was fed into the ADC and the amplifier of the EMC set-up. In this way, it was possible to compare the waveforms one-on-one in the Spike2 software. It also ensured that the signals propagated through most of the same path, except for the pre-amplifiers. To summarize, the following measurements were conducted:

1. Reference (shorted input)
2. 1 ECoG channel, no other channels connected
3. 1 ECoG channel, other ECoG channels connected
4. 1 ECoG channel, split between the two set-ups
5. 1 ECoG channel, RHD connected to EMC's ADC
6. 1 ECoG channel, RHD connected to EMC's ADC and amplifier

The first measurement, the reference measurement, was performed to detect possible problems or artifacts in the set-up. No abnormalities were found. The third, fifth and sixth measurements were performed to compare both systems (AFE of this work and existing set-up in EMC). No deviations compared to the second and fourth measurement were noticed, so only measurement 2 and 4 will be discussed in detail.

Individual measurement

Figure 8.3 displays the raw, unfiltered, signal and the signal filtered with a band-pass filter (BPF) from 0.5 Hz - 100 Hz and a notch filter at 50 Hz. The filter specifications of the bandpass filter are listed in Table 8.1 In the raw signal, some low frequency information is still present. This can be caused by movement or breathing of the mouse. The filters pre-programmed in the AFE are of low order and can apparently not filter out the strong low frequency content. Clearly, seizure-like activity can be seen at $t = 0.5$, 4, 20.5 and 36 seconds (marked red in the Figure). A zoom in on the seizure activity around 20 seconds is displayed in Figure 8.4. This figure contains both a raw and filtered version of the signal. The seizure activity (in the form of generalized spike-and-wave discharges, GSWD's) has a strong frequency component below 10 Hz. In the spectrum displayed in Figure 8.5 a peak can be distinguished around 7 Hz (Arrow 2). The high pass component of the filter at 0.5 Hz (Arrow 1) and the notch filter at 50 Hz (Arrow 3) are clearly visible in the filtered spectrum as well. However, as the reader can see, the 50 Hz component in the raw signal is not higher than other signals around 50 Hz, so it is not a strong interferer. In contrast, when looking at the spectrum of the current EMC set-up in Figure 8.7, a 50 Hz peak can be seen even after the 50 Hz notch filter has been applied. The set-up of this work clearly performs better in terms of 50 Hz interference reduction. This is mainly thanks to the closed Faraday cage surrounding the AFE and the shielded twisted-pair cables connecting the electrodes to the AFE.

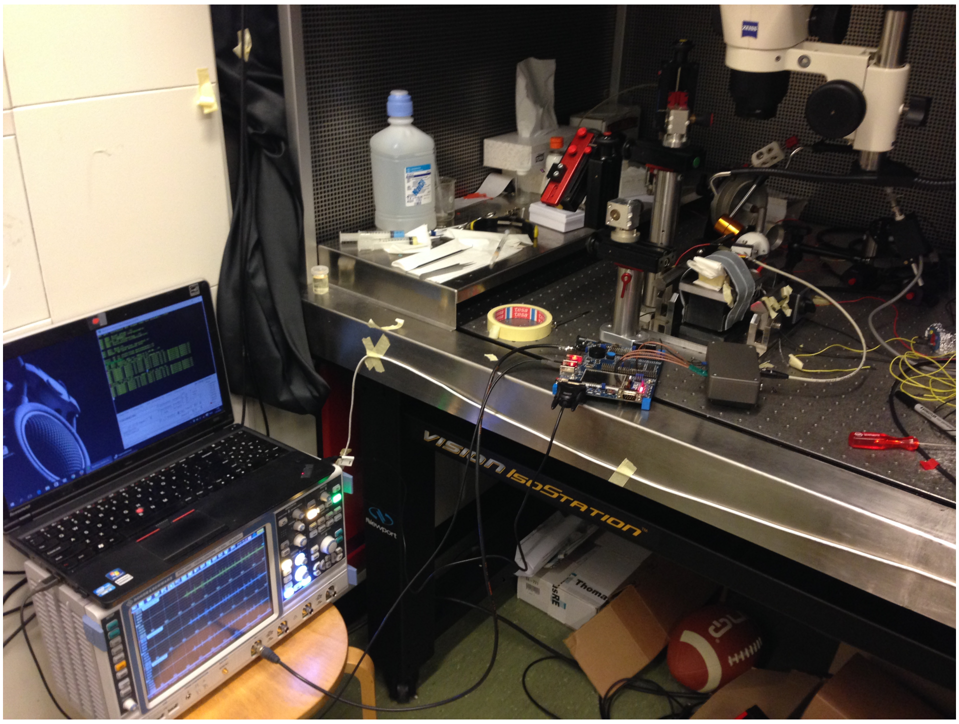

Figure 8.2: Complete ECoG measurement set-up; left: oscilloscope and laptop; centered on the table: MCU and recording device.

Split set-up measurement

By developing a splitter and measuring the same electrode with two different set-ups, a one-on-one comparison could be made between the set-up of this work and the current EMC set-up. The graphs are displayed in Figure 8.6 (raw signal) and Figure 8.8 (after digital filtering). In Figure 8.6 a DC-offset in the EMC measurement is visible (horizontal dashed red line), after filtering (Figure 8.8) the offset is gone. When optically comparing the results of both set-ups (both raw and filtered signals), it seems that the peaks of the AFE are a little bit more pronounced, possibly improving seizure detection. Furthermore, in Figure 8.7 (an FFT of the raw signals) it can be seen there is a wide notch-filter around 50 Hz present in the current EMC set-up. The AFE doesn't have a notch filter and looking at the spectrum it doesn't require one (Arrow 1). In the spectrum a slight peak at 200 Hz is present (Arrow 2). The origin of this frequency is not known. The FFT of the EMC measurement stops at 250 Hz because the signal is sampled at 500 Hz (Arrow 3). In Figure 8.9 an FFT of the filtered signal is shown. The 200 Hz peak is gone, DC-offset is removed (Arrow 1), the 50 Hz notch is still present in the EMC set-up (Arrow 2) and the low pass component of the filter at 100 Hz is clearly visible (Arrow 3). It can be seen that a notch filter is not required in the new set-up, potentially conserving information around 50 Hz. A zoom in on a seizure is depicted in Figure 8.10. As an electrical engineer, it is hard to qualitatively assess the quality of these signals.

When inspecting the Y-axis of the comparison graphs, it can be seen that the scale differs almost 4 orders of magnitude between the two set-ups. Using the AFE, the signal strength is calculated back to the input. This can be done with the EMC set-up as well, but the problem is that the amplification factor of the pre-amplifiers is unknown. The company that manufactured those devices is not manufacturing those amplifiers anymore, and datasheets are not obtainable. In the authors opinion, these set-ups should always work with input referred voltage levels, because the neuroscientists that work with them sometimes start to interpret those voltage levels. But for the current research with seizure detection these voltage levels don't matter yet.

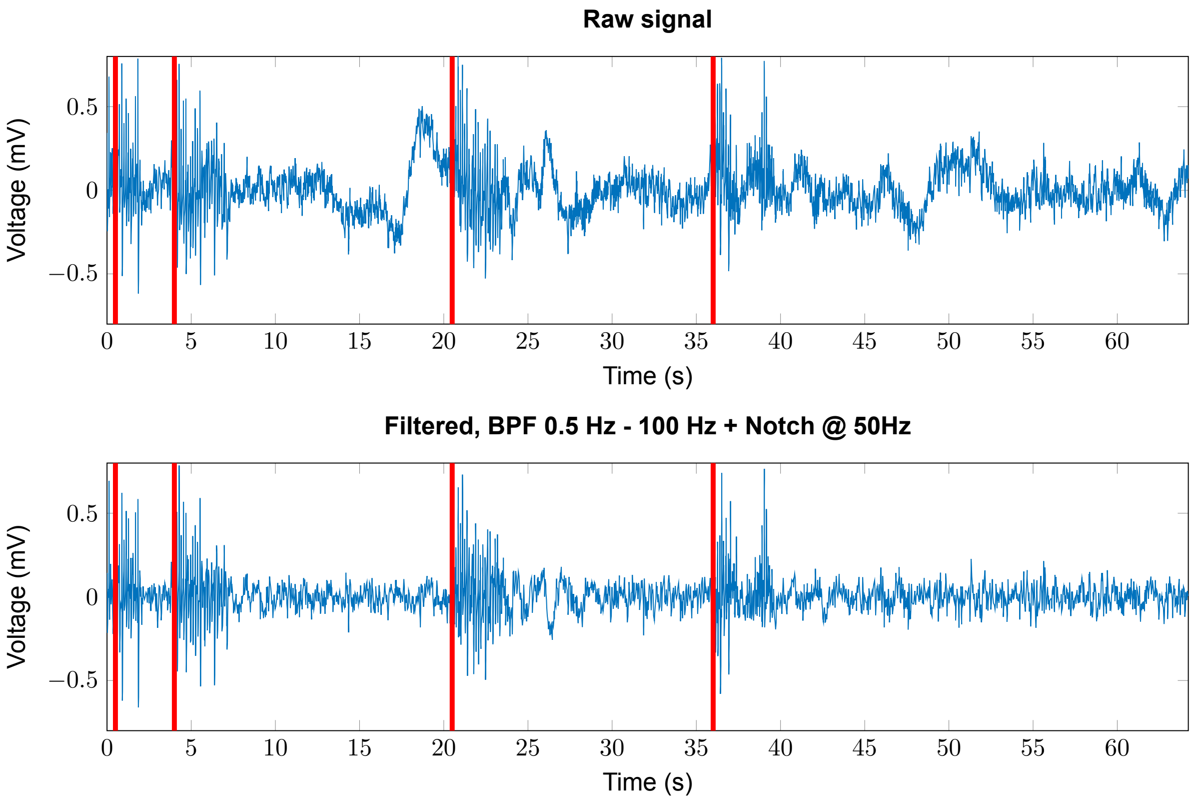

Figure 8.3: Raw and filtered ECoG-signal measured with the AFE. The red lines indicate epileptic seizures.

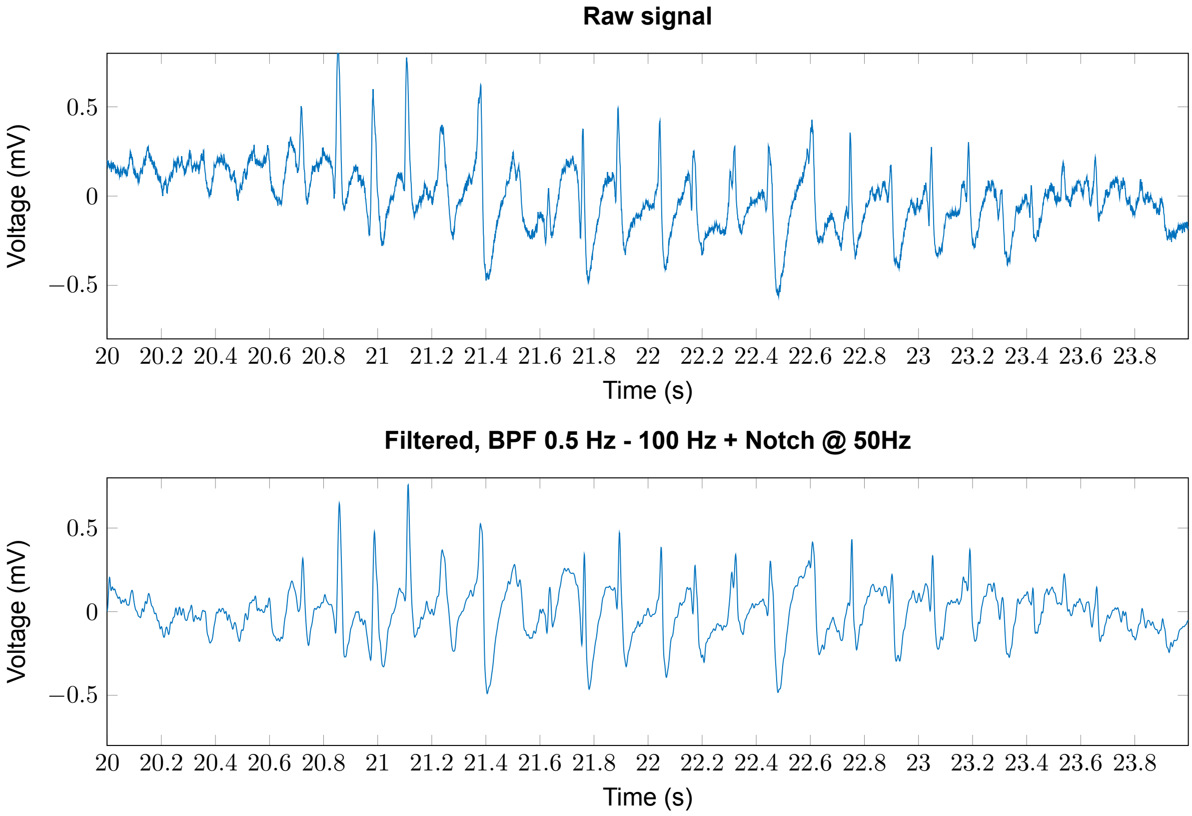

Figure 8.4: Raw and filtered ECoG-signal measured with the AFE, zoomed in on an epileptic seizures.

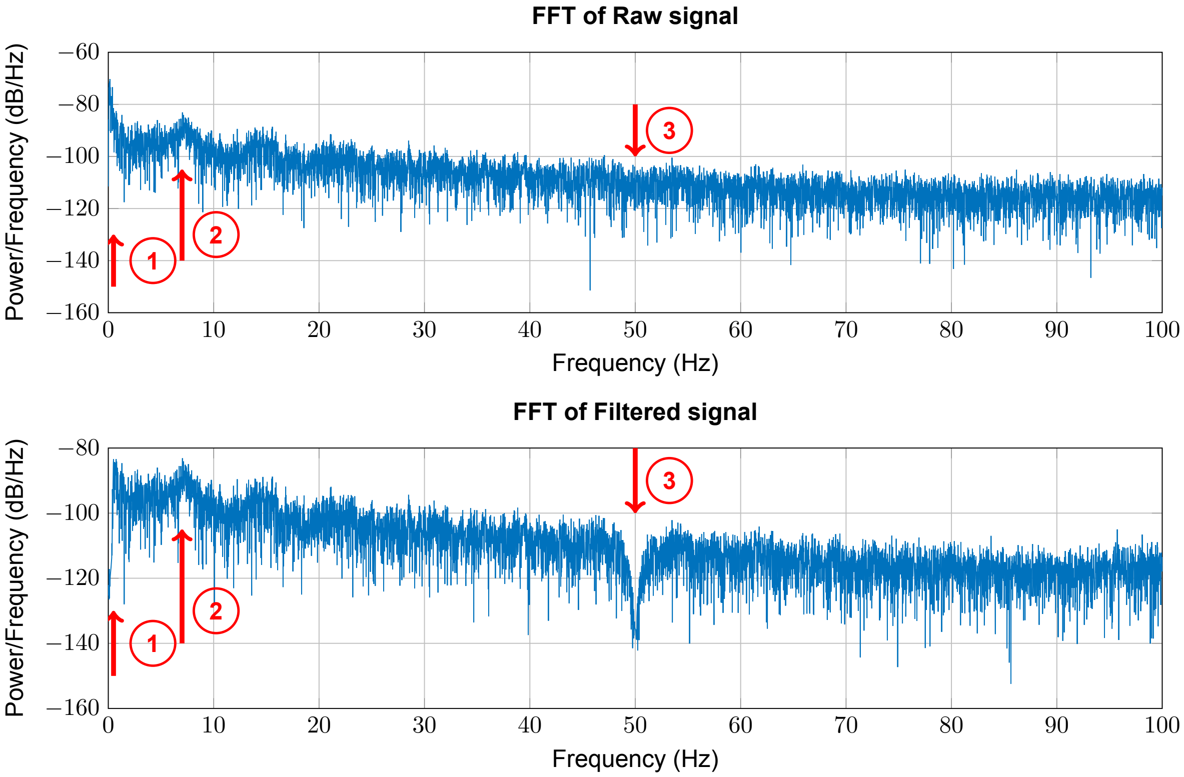

Figure 8.5: FFT of Figure 8.3.

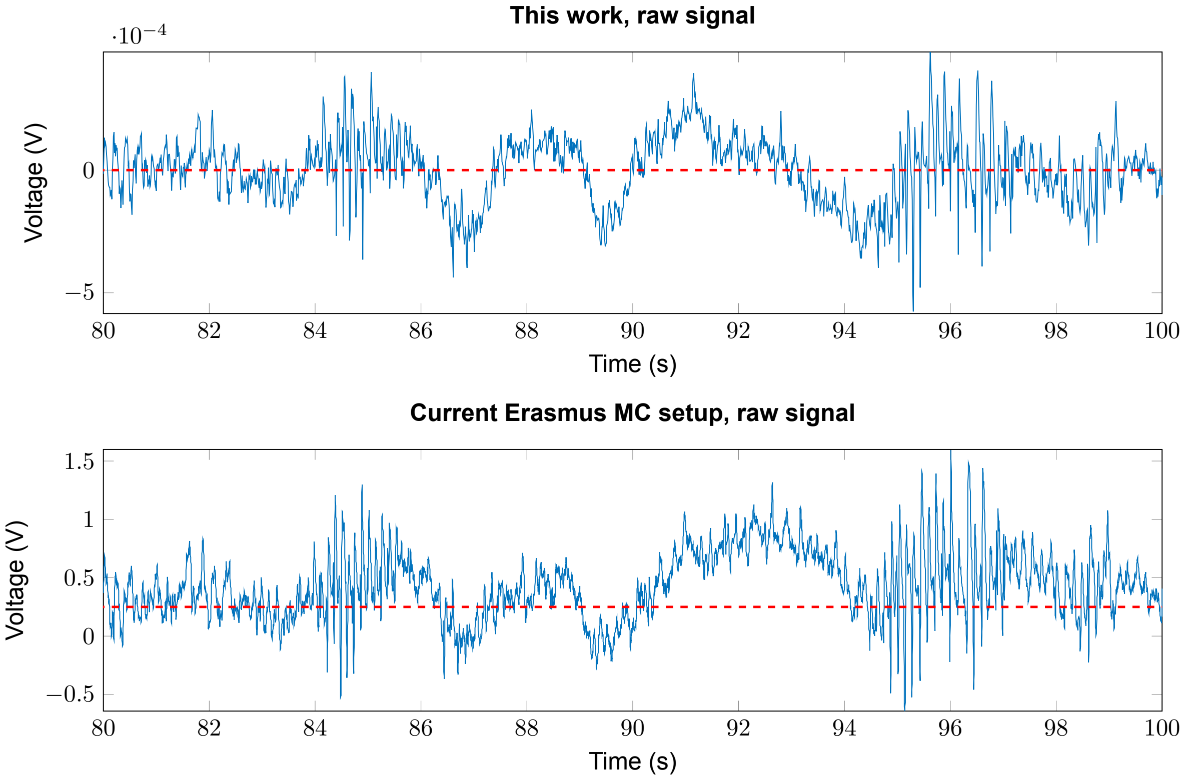

Figure 8.6: Recording made with AFE (top) versus the current set-up at Erasmus MC (bottom).

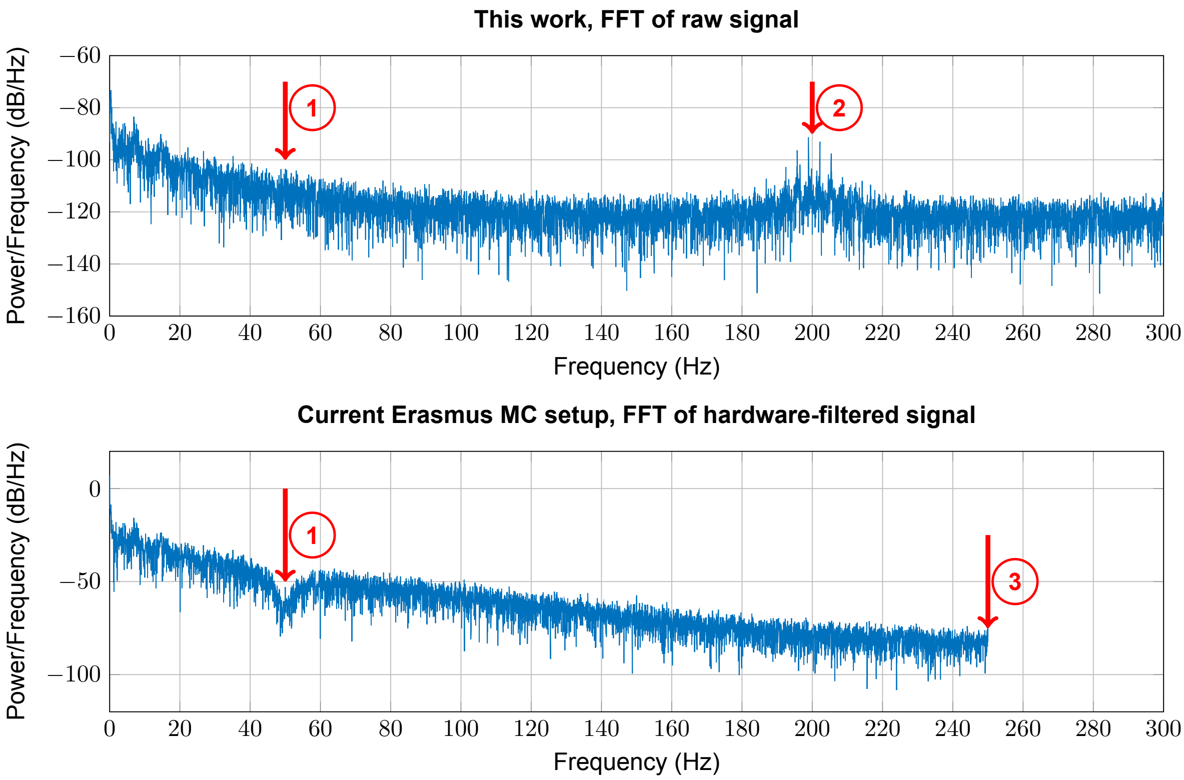

Figure 8.7: FFT of Figure 8.6.

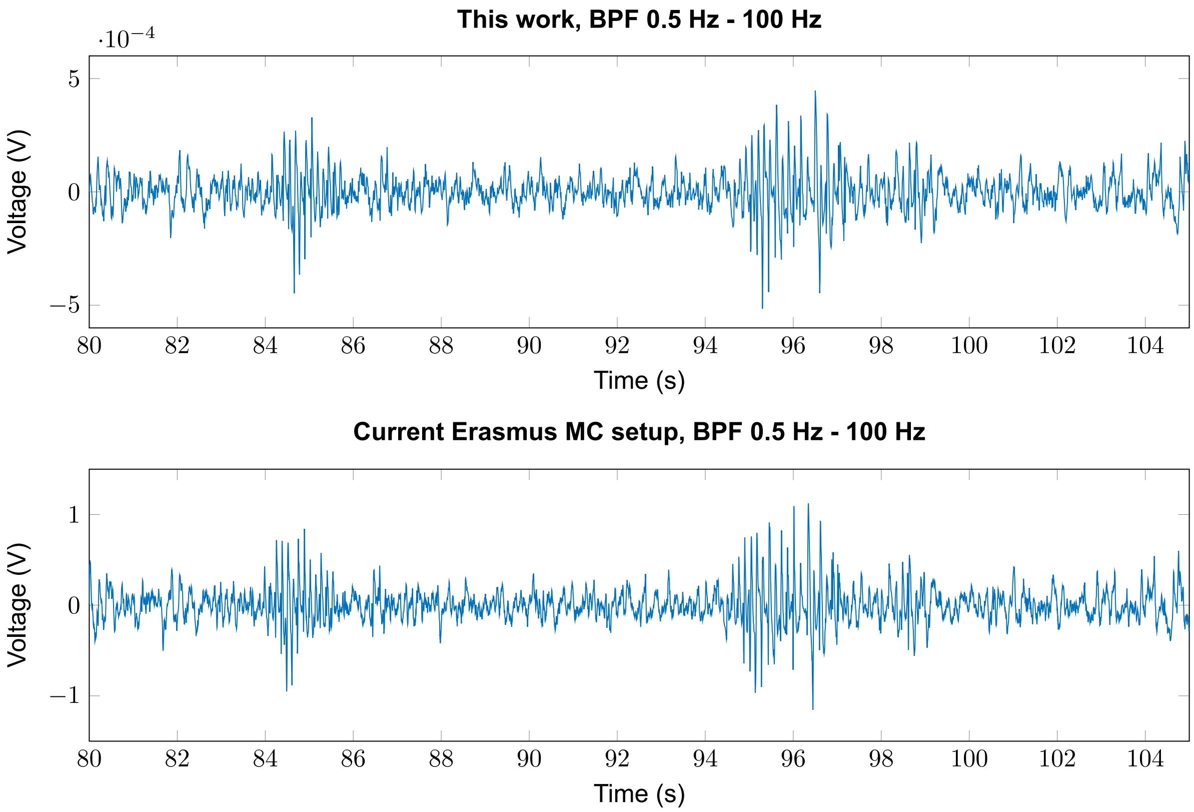

Figure 8.8: Filtered recording made by the AFE (top) versus the current set-up at Erasmus MC (bottom); band-pass filtered from 0.5 - 100 Hz.

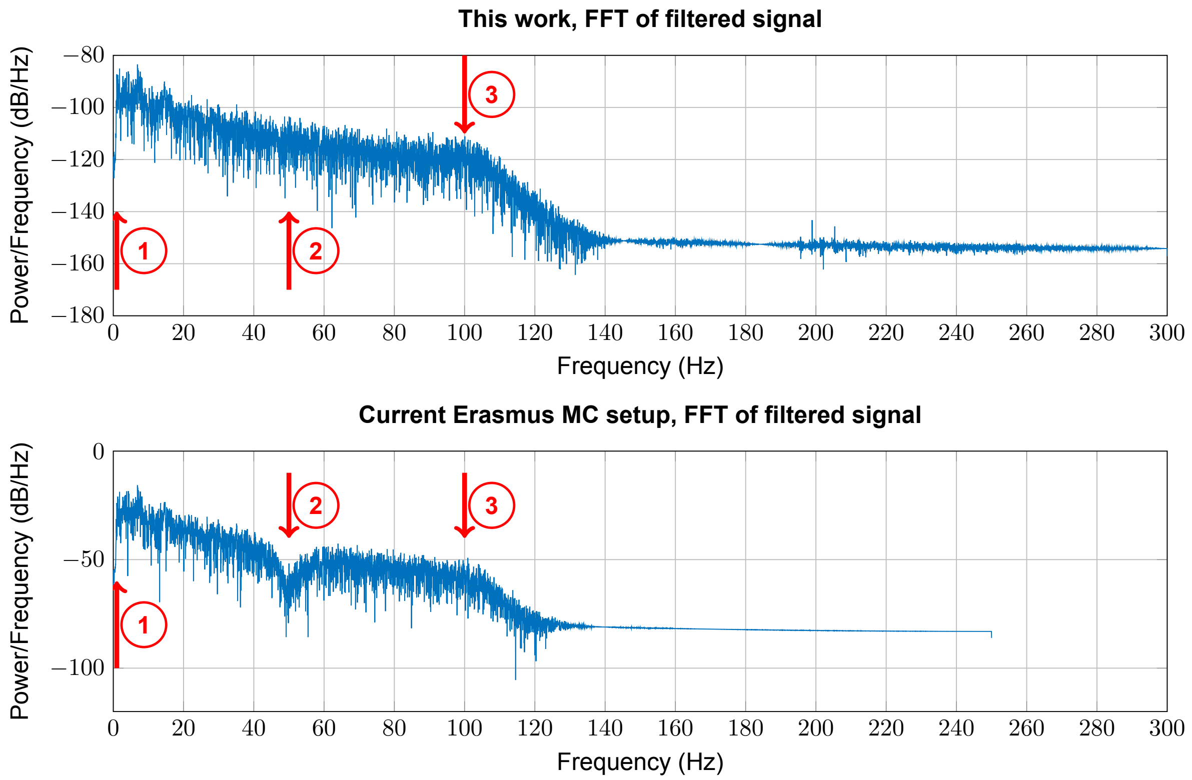

Figure 8.9: FFT of Figure 8.8.

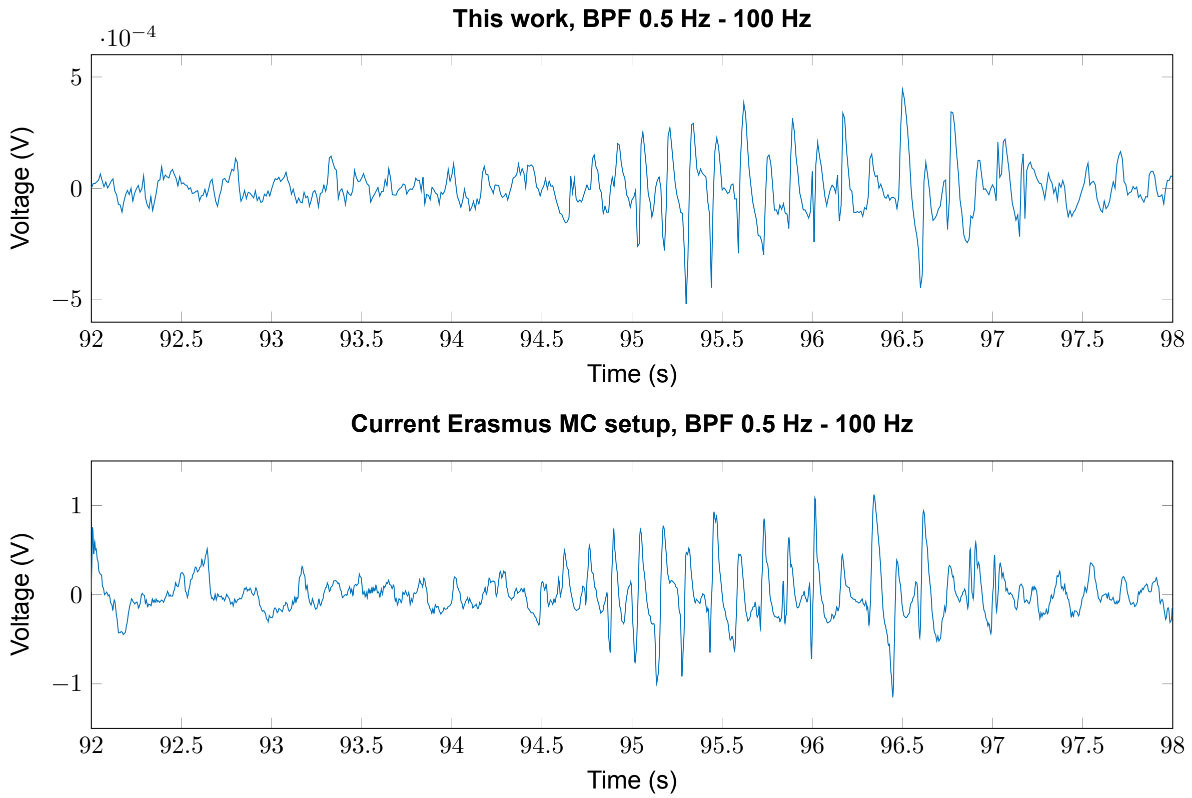

Figure 8.10: A zoomed in view of Figure 8.8.

8.2. Single cell recordings

In the same set-up as the ECoG-measurements (refer to Figures 8.1 and 8.2), a single cell recording was made. Single cell recordings are performed with a glass electrode. The connection to this electrode is of a nature that is completely different from the ECoG electrodes; it is connected via a silver wire in a borosilicate glass tube containing a 2M Sodium-Chloride solution. This tube connects the pre-amplifier with the glass electrode. The glass electrode is mounted on a frame of which the position can be controlled with μm precision. A specific pre-amplifier for glass-electrodes is used (different from the ones of the ECoG set-up, same manufacturer, unknown specifications).

During the measurements it was clear to the author that measurements with glass electrodes cannot yet be performed with the AFE. The reason can be found in the nature of glass electrodes. Glass electrodes have a high source impedance and are used with a current clamp amplifier which has an input impedance in the GΩ range. When the AFE is connected in parallel to the current clamp amplifier, the input impedance drops considerably, resulting in a signal drop at the amplifier input. Furthermore, the AFE can not be configured yet to function as a current clamp amplifier. The results are therefore not presented in this work.

8.3. Conclusions

Different in-vivo measurements that have been performed with the AFE developed in this work have been discussed. The performance has been compared to the current set-up of the EMC Neuroscience department. For the measurement of ECoG, the AFE performs well, and is affected less by 50 Hz interference. This is mainly due to adequate shielding and the use of shielded, twisted-pair wires to connect the AFE with the electrodes. A 50 Hz notch filter may be omitted, conserving ECoG information around 50 Hz.

Single cell recordings with a glass electrode can not be performed with the current AFE implementation. Firstly, the input impedance is too low compared to the high electrode impedance of the glass electrode. Secondly, a current clamp amplifier is not implemented in the current AFE.

9

Conclusions & Recommendations

The goal of this work was to design a system for wireless, multi-subject ECoG monitoring for small rodents for epileptic seizure detection and other neuroscience studies. The system performs the function of an Analog Front-End (AFE) and a wireless link. A discrete component realization was built that uses the backscattering technique and Frequency Division Multiple Access (FDMA) to allow multi-subject wireless communication. The main contribution of this work has been to show that backscattering high bitrate signals (> 300 kbit/s) at different subcarrier frequencies is possible with low complexity, commercially available, electronics. The most significant improvement over the state of the art is the fact that multiple subjects can be measured wirelessly and simultaneously. The subcarrier frequencies are generated by a Cortex M0+ MCU, which means the subcarriers are programmable. The Cortex M0+ has been developed for low-power operation, but it is too slow to achieve the desired bitrate of 0.96 Mbit/s in the current implementation. Three backscattering tags have been demonstrated in this work, transmitting at a bitrate of 80 kbit/s.

Next to this, it has been demonstrated that using two antennas per tag can increase reception of the backscattered signal with an order of magnitude. The AFE for this system has been developed in cooperation with Matthijs Weskin, based on the Intantech RHD2132 32 channel neural recording IC. In-vivo measurements have been conducted with the AFE subsystem at the Erasmus MC neuroscience department, showing improvements over the current setup in terms of interference reduction and size. It was found that this AFE is not suited to measure glass electrode single cell action potentials, mainly due to the low input impedance and the lack of current clamp amplifiers. The ADC used in this AFE has a 16 bit resolution, but it has been shown in this work that an 8 bit resolution might be enough for seizure detection. The total power consumption of the system at maximum speed (320 kbit/s) amounts to 20 mW.

The current implementation is a proof of concept version, which has not been integrated in a miniature PCB yet. When designing a future version, the size and weight requirements will limit the performance in terms of bitrate and battery lifetime. Furthermore, the current system is sensitive to a near-far effect in the receiver, which could cause loss of signal. The 915 MHz ISM band that has been used, potentially contains interference caused by GSM networks. This is a limiting factor for the bitrate and the number of subjects that can be measured simultaneously. A basic, non-realtime receiver has been built with discrete components, an oscilloscope and MATLAB processing. The current implementation uses a square wave subcarrier modulation, which creates odd harmonics. This reduces the number of potential subjects that can be supported by the system simultaneously.

With respect to the initial design requirements, specifications for size (< 1 cm^3), weight (< 2 g) and a high bitrate realtime signal (0.96 Mbit/s) have not been met. Lower bitrate (320 kbit/s), multiple animal support and flexibility have been achieved. Power consumption should be reduced if this system is to be integrated with a Wireless Power Transfer (WPT) link.

The most important recommendations for future work are as follows.

1. Instead of an MCU, a CPLD or small FPGA could be implemented as a control unit. Significantly higher modulation speeds can be achieved, while minimizing overhead and power consumption. One disadvantage of an FPGA is that it can be inconvenient for non-technical personnel. A VCO or similar frequency generating component could be considered for subcarrier generation to improve the subcarrier quality;
2. Usage of a higher carrier frequency than 915 MHz can increase the available bandwidth, allowing a higher bitrate and/or more simultaneous subcarriers. Care should be taken to assess potential interference from other band users;
3. The implementation of some form of pulse-shaping should be considered to reduce the higher harmonics generated with square wave modulation. This would allow implementation of more FDMA subcarriers.

Further recommendations on a more detailed level are listed below.

- When this work is integrated with the work of Farnaz Nassirinia (WPT link and optogenetic stimulator), a battery powered solution should be considered instead of a WPT link. It could reduce the complexity of the tag and allow for a more flexible cage environment;
- If a downlink has to be implemented in a future version of the system, TDMA should be considered as an alternative multiple access method to be used for the downlink as well as the uplink;
- Basestation antennas with a more narrow beamwidth will increase the isolation between the main carrier and the backscattered signals. An array of small patch antennas could be a potential implementation that offers a more narrow beamwidth;
- If a higher carrier frequency is employed, the development of a custom tag antenna should be considered to increase the performance and reduce the size;
- Per tag at least two orthogonally oriented antennas or even three antennas can be used to increase the reliability of the wireless link across the cage;
- To improve the receiver for an FDMA system, two options could be explored: a hardware-oriented approach with subcarrier clock recovery and downconversion or an SDR approach that makes use of a high sample rate ADC;
- The simplicity of ASK is attractive, but a BPSK system can have a 3 dB BER advantage. To further increase bitrate, other constellations could be considered;
- Based on the application of the measured ECoG signals, it should be considered to transmit 8-12 bits instead of 16 bits, to relax the requirement on the wireless link;
- For system integration, use of a 4 layer flexible or flex-rigid PCB is recommended. Care should be taken to separate the analog and digital signals on the PCB. The device should be enclosed and protected from the environment by, for example, non-conductive epoxy or a 3D-printed enclosure. Connection between the electrodes and AFE should be as short as possible.

Bibliography

[1] Cambridge Electronic Design, “CED amplifier and ADC,” http://ced.co.uk/products/pow3in, accessed: 01-08-2016.

[2] “Neurologger product page,” http://www.newbehavior.com/products/neurologger, accessed: 25-02-2016.

[3] S. J. Thomas, R. R. Harrison, A. Leonardo, and M. S. Reynolds, “A Battery-Free Multichannel Digital Neural/EMG Telemetry System for Flying Insects,” *Biomedical Circuits and Systems, IEEE Transactions on*, vol. 6, no. 5, pp. 424–436, 2012.

[4] G. Gagnon-Turcotte, Y. LeChasseur, C. Bories, Y. De Koninck, and B. Gosselin, “A wireless optogenetic headstage with multichannel neural signal compression,” pp. 1–4, 2015.

[5] W. Penfield and H. Jasper, *Epilepsy and the functional anatomy of the human brain*, 1954.

[6] L. Kros, O. H. J. E. Rooda, C. I. De Zeeuw, and F. E. Hoebeek, “Controlling Cerebellar Output to Treat Refractory Epilepsy,” *Trends in Neurosciences*, vol. 38, no. 12, pp. 787–799, Dec. 2015.

[7] J. Engel Jr., “ILAE classification of epilepsy syndromes,” *Epilepsy Research*, vol. 70, pp. 5–10, Aug. 2006.

[8] B. Litt, “Engineering devices to treat epilepsy: a clinical perspective,” in *2001 23rd Annual International Conference of the IEEE Engineering n Medicine and Biology Society*. IEEE, 2001, pp. 4124–4128.

[9] S. Shoham and S. Nagarajan, *Neuroprosthetics, theory and practice*. World Scientific Publishing Co., 2004, vol. 2, ch. 2.4.

[10] E. N. Marieb and K. Hoehn, *Human Anatomy and Physiology 9th Edition*. Pearson, 2013.

[11] E. C. Leuthardt, G. Schalk *et al.*, “A brain–computer interface using electrocorticographic signals in humans,” *Journal of Neural Engineering*, vol. 1, no. 2, pp. 63–71, Jun. 2004.

[12] J. M. Rabaey, “Brain-machine interfaces as the new frontier in extreme miniaturization,” in *ESSDERC 2011 - 41st European Solid State Device Research Conference*. IEEE, 2011, pp. 19–24.

[13] W. Wattanapanitch and R. Sarpeshkar, “A Low-Power 32-Channel Digitally Programmable Neural Recording Integrated Circuit,” *Biomedical Circuits and Systems, IEEE Transactions on*, vol. 5, no. 6, pp. 592–602, 2011.

[14] R. B. A. Adamson, M. Bance, and J. A. Brown, “A piezoelectric bone-conduction bending hearing actuator.” *The Journal of the Acoustical Society of America*, vol. 128, no. 4, pp. 2003–2008, Oct. 2010.

[15] B. I. Rapoport, J. T. Kedzierski, and R. Sarpeshkar, “A glucose fuel cell for implantable brain-machine interfaces.” *PloS one*, vol. 7, no. 6, p. e38436, 2012.

[16] T. Sun and X. Xie, *Wireless Power Transfer for Medical Microsystems*, 2013.

[17] L. Kros, O. H. J. Eelkman Rooda, and M. N. van Dongen, “Cerebellar output controls generalized spike-and-wave discharge occurrence.” *Annals of neurology*, vol. 77, no. 6, pp. 1027–1049, Jun. 2015.

[18] M. N. van Dongen, A. Karapatis, L. Kros *et al.*, “An implementation of a wavelet-based seizure detection filter suitable for realtime closed-loop epileptic seizure suppression,” in *Biomedical Circuits and Systems Conference (BioCAS)*. IEEE, 2014, pp. 504–507.

[19] S. J. Thomas, J. S. Besnoff, and M. S. Reynolds, “Modulated backscatter for ultra-low power uplinks from wearable and implantable devices,” in *the 2012 ACM workshop*. New York, USA: ACM Press, 2012, pp. 1–6.

[20] A. L. Mansano, Y. Li, S. Bagga, and W. A. Serdijn, “An Autonomous Wireless Sensor Node With Asynchronous ECG Monitoring in 0.18 um CMOS,” *IEEE T-BIOCAS*, June 2016.

[21] R. Sarpeshkar, *Ultra Low Power Bioelectronics*. Cambridge University Press, 2010, page 490.

[22] B. Rembold, “Optimum Modulation Efficiency and Sideband Backscatter Power Response of RFID-Tags,” *Frequenz*, vol. 63, no. 1-2, pp. 1–6, Jan. 2009.

[23] J. P. Curty, M. Declercq, C. Dehollain, and N. Joehl, “Design and optimization of passive UHF RFID systems,” 2006.

[24] D. Dobkin, *The RF in RFID, Passive UHF RFID in Practice*. Elsevier, 2008.

[25] A. Loeffler, I. Altmann, and F. Schuh, “CDMA-Based UHF-RFID System with Semi-Passive UHF Transponders,” pp. 1–16, Jan. 2016.

[26] H.-C. Liu, “The Approaches in Solving Passive RFID Tag Collision Problems, Radio Frequency Identification Fundamentals and Applications Bringing Research to Practice,” 2010, http://www.intechopen.com/books/radio-frequency-identificationfundamentals-and-applications-bringing-research-to-practice/the-approaches-in-solving-passive-rfid-tagcollision-problems.

[27] E. Kampianakis, J. Kimionis *et al.*, “Backscatter sensor network for extended ranges and low cost with frequency modulators: Application on wireless humidity sensing,” pp. 1–4, 2013.

[28] G. Vannucci, A. Bletsas, and D. Leigh, “A Software-Defined Radio System for Backscatter Sensor Networks,” *IEEE Transactions on Wireless Communications*, vol. 7, no. 6, pp. 2170–2179, Jun. 2008.

[29] S. Thomas and M. S. Reynolds, “QAM backscatter for passive UHF RFID tags,” *IEEE International Conference on RFID*, 2010.

[30] S. J. Thomas and M. S. Reynolds, *A 96 Mbit/sec, 15.5 pJ/bit 16-QAM modulator for UHF backscatter communication*. IEEE, 2012.

[31] I. Williams, S. Luan, and A. Jackson, *Live demonstration: A scalable 32-channel neural recording and real-time FPGA based spike sorting system*. BioCAS, 2015.

[32] E. G. Kilinc, C. Baj-Rossi *et al.*, “A System for Wireless Power Transfer and Data Communication of Long-Term Bio-Monitoring,” *IEEE Sensors Journal*, vol. 15, no. 11, pp. 6559–6569, 2015.

[33] S. Yang, J. Cho *et al.*, “Feedback controlled piezo-motor microdrive for accurate electrode positioning in chronic single unit recording in behaving mice.” *Journal of neuroscience methods*, vol. 195, no. 2, pp. 117–127, Feb. 2011.

[34] E. Greenwald, M. Mollazadeh *et al.*, “A VLSI Neural Monitoring System With Ultra-Wideband Telemetry for Awake Behaving Subjects.” *Biomedical Circuits and Systems, IEEE Transactions on*, vol. 5, no. 2, pp. 112–119, Apr. 2011.

[35] JAX, “C57BL/6J Phenotype information,” https://www.jax.org/strain/000664, [Online; accessed 07-10-2015].

[36] Y. Li, A. L. Mansano, Y. Yuan, D. Zhao, and W. A. Serdijn, “An ECG Recording Front-End With Continuous-Time Level-Crossing Sampling,” *Biomedical Circuits and Systems, IEEE Transactions on*, vol. 8, no. 5, pp. 626–635, 2014.

[37] Xilinx, “What is the difference between CPLDs and FPGAs?” http://www.xilinx.com/support/answers/7598.html, [Online; accessed 14-06-2016].

[38] J. D. Griffin and G. D. Durgin, “Complete Link Budgets for Backscatter-Radio and RFID Systems,” *IEEE Antennas and Propagation Magazine*, vol. 51, no. 2, pp. 11–25, Apr. 2009.

[39] ITU, “International telecommunication union page on ISM,” http://www.itu.int/net/ITU-R/terrestrial/faq/index.html#g013, accessed: 01-03-2016.

[40] FCC, “Federal communications commission page on MICS / MedRadio,” https://www.fcc.gov/general/medical-device-radiocommunications-service-medradio, accessed: 01-03-2016.

[41] FCC, “Federal communications commission page on wireless medical telemetry service,” https://www.fcc.gov/general/wireless-medical-telemetry-service-wmts, accessed: 01-03-2016.

[42] ECC, “European communications committee document on the frequency spectrum allocation,” http://www.erodocdb.dk/docs/doc98/official/pdf/ERCRep025.pdf, accessed: 01-03-2016.

[43] J. Griffin, G. Durgin, A. Haldi, and B. Kippelen, “RF Tag Antenna Performance on Various Materials Using Radio Link Budgets,” *Antennas and Wireless Propagation Letters*, vol. 5, no. 1, pp. 247–250, Jun. 2006.

[44] C. K. Poon and T. Suda, “Effect of guard band and guard time on mean message transmission delays in FDMA and TDMA [satellite communications],” pp. 360–364 vol.2, 1990.

[45] Stephen P. Boyd, Stanford University, “GGPLAB MATLAB toolbox,” https://stanford.edu/~boyd/ggplab/, [Online; accessed 02-08-2016].

[46] L. W. Couch, II, *Digital and Analog Communication Systems*, 6th ed. Upper Saddle River, NJ, USA: Prentice Hall PTR, 2000.

[47] M. Simon and D. Divsalar, “Some interesting observations for certain line codes with application to RFID,” *IEEE Transactions on Communications*, vol. 54, no. 4, pp. 583–586, 2006.

[48] C. A. Balanis, *Antenna Theory: Analysis and Design*. Wiley-Interscience, 2005.

[49] Taoglas, “Taoglas 915 mhz embedded ceramic patch antenna,” https://www.taoglas.com/wp-content/uploads/2015/06/ISPC.91A.09.0092E.pdf, accessed: 11-07-2016.

[50] J. D. Griffin, “High-frequency modulated-backscatter communication using multiple antennas,” 2009.

[51] Johanson Technology, “915 MHz ISM Antenna for small form factor applications,” http://www.johansontechnology.com/datasheets/antennas/0915AT43A0026.pdf, accessed: 13-07-2016.

[52] Analog Devices, “Wideband, 40 db isolation at 1 ghz, cmos 1.65 v to 2.75 v, spst switches adg901/adg902,” http://www.analog.com/media/en/technical-documentation/data-sheets/ADG901_902.pdf, accessed: 13-07-2016.

[53] TI, “LP38690 LDO,” http://www.farnell.com/datasheets/2030079.pdf?_ga=1.91314394.1935961425.1456491312, accessed: 12-07-2016.

[54] Y. Meyavuz, “Linear, circular and elliptical polarization animation in a single shot,” https://www.youtube.com/watch?v=Q0qrU4nprB0, accessed: 11-07-2016.

A

Additional theory

A.1. Polarization

Figure A.1 depicts the wave propagation for each polarization [54]. Circular polarization can be used very effectively to mitigate polarization mismatch and is used extensively in satellite communication, where polarization mismatch is an important factor [38]. Another way to look at it, is that linear polarization and circular polarization are extreme cases of elliptical polarization; when the ellipse becomes a straight line it is linear, and when it becomes a circle it is circular [48].

The rotation of polarization is defined as clockwise or counterclockwise. When an antenna receives an incoming wave that does not have the same polarization as the antenna, polarization mismatch occurs that reduces the amplitude of the signal at the antenna terminals. In the case of linear polarization, two orthogonally aligned antennas with the same linear polarization will barely be able to induce signals at each other's terminals. This could potentially mean loss of information for a communication link. When using a combination of a circular and a linear antenna, these peaks in polarization mismatch can be compensated at the cost of a decrease in average signal strength. However, when the linear antenna is oriented in such a way that its polarization is perpendicular to the circular polarized wave, high polarization mismatch can still occur.

A.2. Near field and far field

As can be seen in Figure A.2, the far field is defined to start at a distance of 2 wavelengths from an antenna. This boundary is not abrupt, and can differ slightly from system to system. There is a transition region between the near field and the far field, and the near field is split into two parts. The radiative near field might not exist in case the antenna has a small dimension compared to the wavelength. For the tag antenna, this will be true, as it is selected for minimum size. The main point of the distinction between near field and far field is that the field is better defined at large distances. In the reactive near

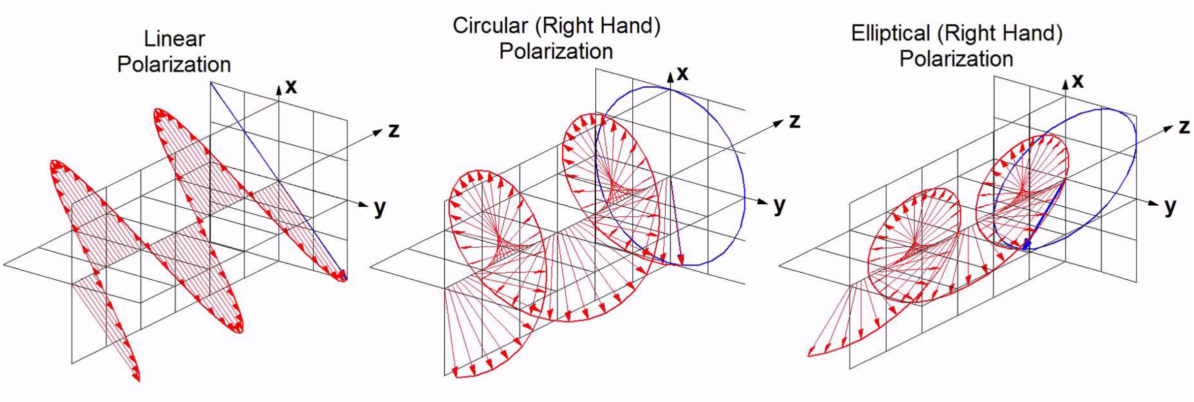

Figure A.1: Linear, circular and elliptical polarization [54].

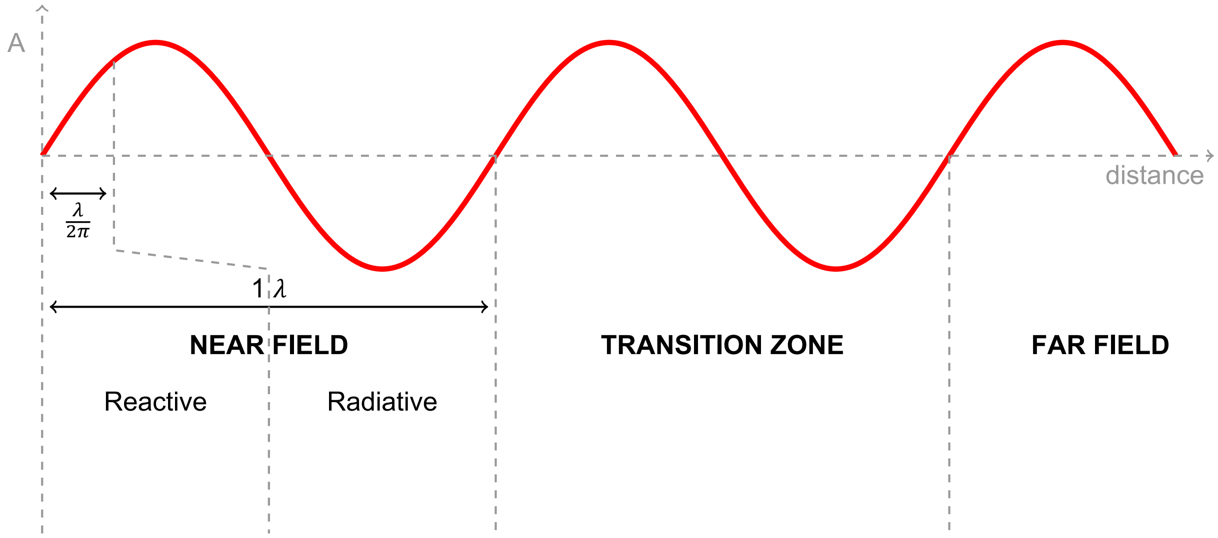

Figure A.2: Near field, transition zone and far field regions for antennas that are shorter than half of the wavelength.

field, the electric and magnetic fields are not necessarily in phase, and the angular field distribution depends strongly on distance. Between the near field and the far field (transition region), the electric and magnetic fields are in phase, but distance still has an impact on the angular field distribution. In other words, the shape of the antenna still has an impact on the field distribution. In the far field, the antenna can be approximated as a point source and the angular field is virtually independent of distance.

A.3. Diffraction

Diffraction is a phenomenon that can negatively impact the received signal strength in a wireless system. This effect is caused by the fact that objects of a certain size relative to the wavelength can cause multiple signal paths through and around it. When these signals arrive at the tag, they will have a phase difference. These signals with different paths can cancel out or add up at the tag. The phase difference relative to half of the wavelength is measured in the number of *Fresnel zones*, as stated in Equation A.1 below. With respect to Equation A.1, k represents the wavenumber (ω/c) and $L_{1,2}$ are the different path lengths.

$$\frac{\delta\phi}{\pi} = k(L_1 - L_2) \tag{A.1}$$

When this number is a small number of Fresnel zones, diffraction has a big impact. This results in a complex shadow region. When the number of Fresnel zones is large (greater than 3), the shadow of the object is well defined, and might hide the tag from the basestation.

B

Receiver MATLAB code

Listing B.1: ’MATLAB receiver code’

```
%% Variables
Fs = 100e6;                     % Sampling frequency of oscilloscope
nChannels = 3;                  % No. of subcarriers
Fsc = [1.2e6; 2.1e6; 3e6];      % Used subcarrier frequencies
BW  = 200e3;                    % Bandwidth around each subcarrier

% Filtering
Order = 10;
Stopband_att = 100;
Passband_ripple = 0.2;
lpf = repmat(BW,3,1);
% Digitizing
threshold = 2;
smoothing = 500e3;

f = csvread(’../../Graduation/Measurements/RTO/WIRELESS/3tags.Wfm.csv’);
N = length(f);
t = 1/Fs:1/Fs:N/Fs;

%% BPF
filtered = zeros(nChannels,N);
figure(2);

for i = 1:1:nChannels
    d = designfilt(’bandpassiir’, ’FilterOrder’, Order, ’PassbandFrequency1’, ...
                       Fsc(i)-BW, ’PassbandFrequency2’, Fsc(i)+BW, ...
                       ’StopbandAttenuation1’, Stopband_att, ’PassbandRipple’, ...
                       Passband_ripple, ’StopbandAttenuation2’, Stopband_att, ...
                       ’SampleRate’, Fs);
    filtered(i,:) = filter(d,f);
end

%% "Downconversion"
down = zeros(nChannels,N);
digital = zeros(nChannels,N);

for i = 1:1:nChannels
    down(i,:) = abs(hilbert(filtered(i,:)));

    d = designfilt(’lowpassiir’, ’FilterOrder’, 5, ’PassbandFrequency’, ...
                      lpf(i), ’StopbandAttenuation’, 50, ’PassbandRipple’, 0.5, ...
```

```
                      'SampleRate', Fs);
    down(i,:) = filter(d,down(i,:));

    down(i,:) = smooth(down(i,:),Fs/smoothing); % smooth out sharp peaks
    comp = ones(1,N)*mean(down(i,:))*threshold; % Make a comparison matrix
    digital(i,:) = down(i,:) >= comp; % compare
end

%% Combination plot showing filtered signal, envelope and bits detected
figure(3);

for i = 1:1:nChannels
    subplot(nChannels,1,i);
    plot(t*1e3,[filtered(i,:); down(i,:); digital(i,:)*max(filtered(i,:))]);
    str=sprintf('Mouse %d @ %0.2e MHz', i, Fsc(i));
    title(str);
    axis([t1 t2 min(filtered(i,:)) max(filtered(i,:))]);
    xlabel('Time (ms)');
    ylabel('Voltage (V)');
end

%% Rudimentary Manchester decoder
for i = 1:1:nChannels
    both = find(transitions(i,:) == 1 | transitions(i,:) == -1); % transitions
    interval = diff([both length(transitions)]);
    average  = mean(interval);
    half     = min(interval);
    true_average = mean(interval(interval < average));           % correct average

    bits = digital(i,(both+1));

    count = 1;
    skip  = 1;
    byte = 0;
    packets = 1;
    n = 1;
    while n < length(bits)
        if(interval(n) < 0.3*true_average)              % Skip too short bits

        elseif(interval(n) < true_average && skip == 0) % Clock transition
            skip = 1;
        elseif(interval(n) > true_average*5)            % New packet
            skip = 1;
            packets = packets+1;
            count = 1;
        else                                            % This is a data bit
            byte(packets,count) = bits(n);
            skip = 0;
            count = count + 1;
        end

        n = n + 1;
    end

    % Isolate sample and packet
    packet(i,:) = dec2hex(bi2de(byte(:,1:24)));
    data(i,:) = dec2hex(bi2de(byte(:,4:19)));
end
```

C

MCU generated frequencies

Table C.1: Distribution of possible subcarriers generated by the MCU, for different base clocks.

21 MHz	Div1							
Div2	2	4	8	16	32	64	128	256
1	1.05×10^7	5.25×10^6	2.63×10^6	1.31×10^6	6.56×10^5	3.28×10^5	1.64×10^5	8.20×10^4
2	5.25×10^6	2.63×10^6	1.31×10^6	6.56×10^5	3.28×10^5	1.64×10^5	8.20×10^4	4.10×10^4
3	3.50×10^6	1.75×10^6	8.75×10^5	4.38×10^5	2.19×10^5	1.09×10^5	5.47×10^4	2.73×10^4
4	2.63×10^6	1.31×10^6	6.56×10^5	3.28×10^5	1.64×10^5	8.20×10^4	4.10×10^4	2.05×10^4
5	2.10×10^6	1.05×10^6	5.25×10^5	2.63×10^5	1.31×10^5	6.56×10^4	3.28×10^4	1.64×10^4
6	1.75×10^6	8.75×10^5	4.38×10^5	2.19×10^5	1.09×10^5	5.47×10^4	2.73×10^4	1.37×10^4
7	1.50×10^6	7.50×10^5	3.75×10^5	1.88×10^5	9.38×10^4	4.69×10^4	2.34×10^4	1.17×10^4
24MHz	Div1							
Div2	2	4	8	16	32	64	128	256
1	1.20×10^7	6.00×10^6	3.00×10^6	1.50×10^6	7.50×10^5	3.75×10^5	1.88×10^5	9.38×10^4
2	6.00×10^6	3.00×10^6	1.50×10^6	7.50×10^5	3.75×10^5	1.88×10^5	9.38×10^4	4.69×10^4
3	4.00×10^6	2.00×10^6	1.00×10^6	5.00×10^5	2.50×10^5	1.25×10^5	6.25×10^4	3.13×10^4
4	3.00×10^6	1.50×10^6	7.50×10^5	3.75×10^5	1.88×10^5	9.38×10^4	4.69×10^4	2.34×10^4
5	2.40×10^6	1.20×10^6	6.00×10^5	3.00×10^5	1.50×10^5	7.50×10^4	3.75×10^4	1.88×10^4
6	2.00×10^6	1.00×10^6	5.00×10^5	2.50×10^5	1.25×10^5	6.25×10^4	3.13×10^4	1.56×10^4
7	1.71×10^6	8.57×10^5	4.29×10^5	2.14×10^5	1.07×10^5	5.36×10^4	2.68×10^4	1.34×10^4

D

PCB layouts

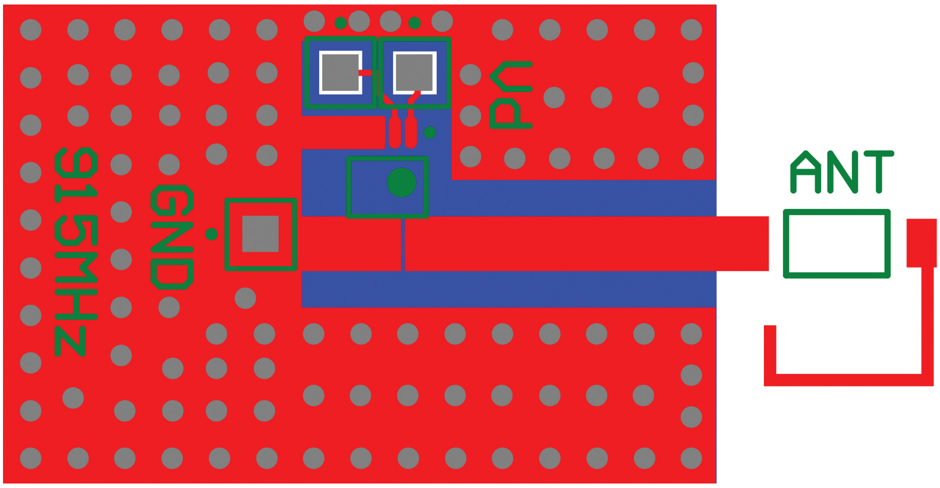

Figure D.1: PCB layout developed for the tag.

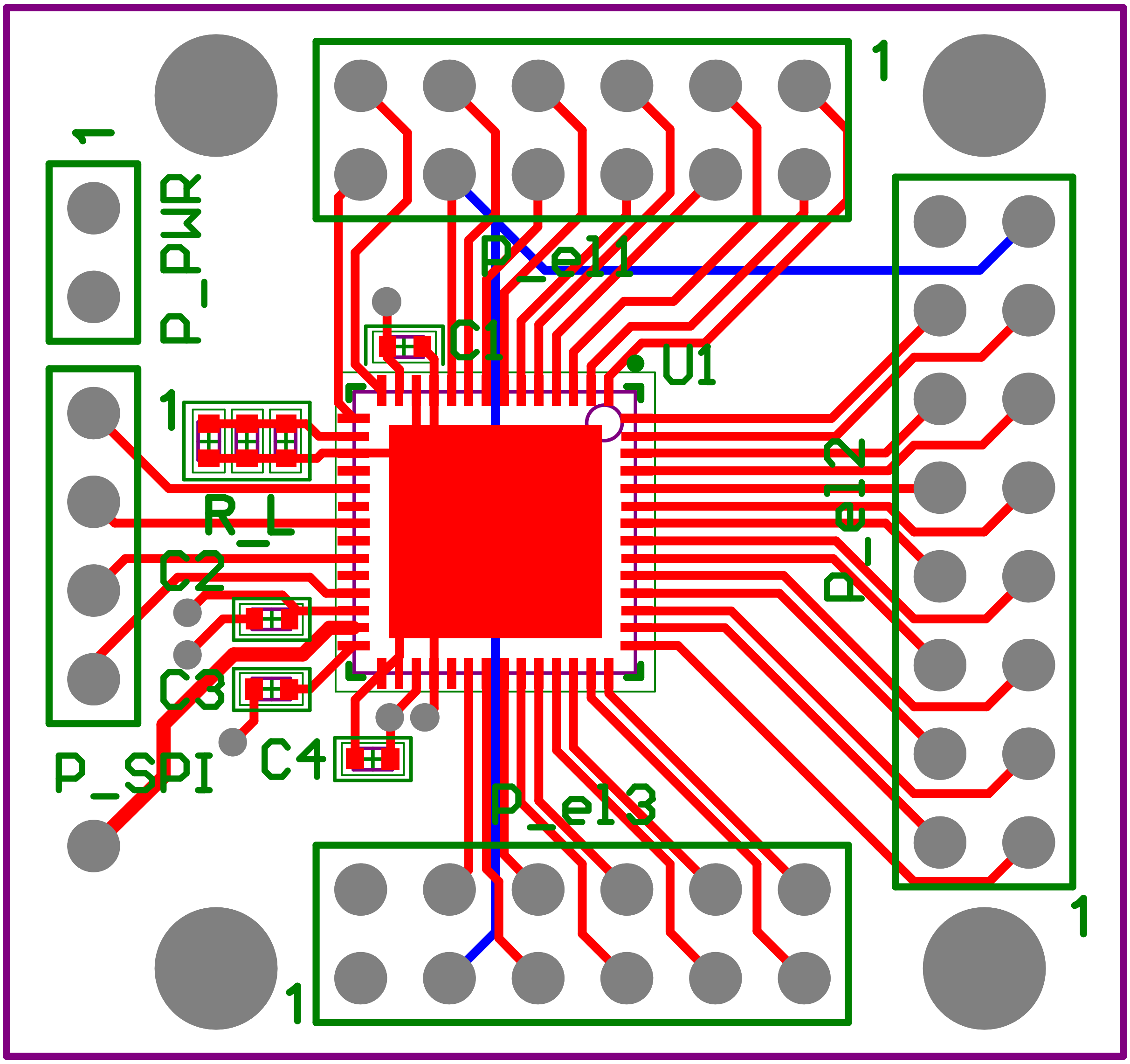

Figure D.2: PCB layout of the AFE.